

AFRL-ML-WP-TR-2001-4148



MATERIALS DEVELOPMENT RESEARCH

**Emmanuel E. Boakye, Ph.D.
Peter M. Hazzledine, Ph.D.
Kristin A. Keller, M.S.
Young-Won Kim, Ph.D.
Tai-II Mah, Ph.D.
Madan G. Mendiratta, Ph.D.
Sarah K. Menon, Ph.D.**

**Pavel Mogilevsky, Ph.D.
T.A. Parthasarathy, Ph.D.
M. Dennis Petry, M.S.
Satish I. Rao, Ph.D.
Oleg N. Senkov, Ph.D
Jonathan E. Spowart, Ph.D.
Christopher F. Woodward, Ph.D.**

**UES, INC.
4401 DAYTON-XENIA ROAD
DAYTON, OH 45432-1894**

SEPTEMBER 2001

FINAL REPORT FOR PERIOD OF 15 SEPTEMBER 1996 - 18 APRIL 2001

Approved for public release; distribution unlimited

**SENSORS DIRECTORATE
AIR FORCE RESEARCH LABORATORY
AIR FORCE MATERIEL COMMAND
WRIGHT-PATTERSON AIR FORCE BASE, OH 45433-7318**

20020613 018

NOTICE

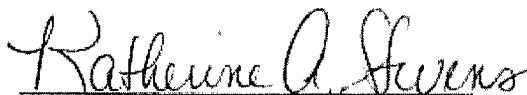
USING GOVERNMENT DRAWINGS, SPECIFICATIONS, OR OTHER DATA INCLUDED IN THIS DOCUMENT FOR ANY OTHER PURPOSE OTHER THAN GOVERNMENT PROCUREMENT DOES NOT IN ANY WAY OBLIGATE THE US GOVERNMENT. THE FACT THAT THE GOVERNMENT FORMULATED OR SUPPLIED THE DRAWINGS, SPECIFICATIONS, OR OTHER DATA DOES NOT LICENCE THE HOLDER OR ANY OTHER PERSON OR CORPORATION, OR CONVEY ANY RIGHTS OR PERMISSION TO MANUFACTURE, USE, OR SELL ANY PATENTED INVENTION THAT MAY IN ANY WAY RELATE TO THEM.

THIS REPORT IS RELEASABLE TO THE NATIONAL TECHNICAL INFORMATION SERVICE (NTIS). AT NTIS, IT WILL BE AVAILABLE TO THE GENERAL PUBLIC, INCLUDING FOREIGN NATIONS.

THIS TECHNICAL REPORT HAS BEEN REVIEWED AND IS APPROVED FOR PUBLICATION.



GERALD B. MILLER, Captain
Project Engineer
Metals Branch
Metals, Ceramics & NDE Division
Materials & Manufacturing Directorate



KATHERINE A. STEVENS, Chief
Metals Branch
Metals, Ceramics & NDE Division
Materials & Manufacturing Directorate



GERALD J. PETRAK, Assistant Chief
Metals, Ceramics & NDE Division
Materials & Manufacturing Directorate

IF YOUR ADDRESS HAS CHANGED, IF YOU WISH TO BE REMOVED FROM OUR MAILING LIST, OR IF THE ADDRESSEE IS NO LONGER EMPLOYED BY YOUR ORGANIZATION, PLEASE NOTIFY, AFRL/MLLM, WRIGHT-PATTERSON AFB OH 45433-7750 TO HELP US MAINTAIN A CURRENT MAILING LIST.

COPIES OF THIS REPORT SHOULD NOT BE RETURNED UNLESS RETURN IS REQUIRED BY SECURITY CONSIDERATIONS, CONTRACTUAL OBLIGATIONS, OR NOTICE ON A SPECIFIC DOCUMENT.

REPORT DOCUMENTATION PAGE			Form Approved OMB No. 074-0188
<p>Public reporting burden for this collection of information is estimated to average 1 hour per response, including the time for reviewing instructions, searching existing data sources, gathering and maintaining the data needed, and completing and reviewing this collection of information. Send comments regarding this burden estimate or any other aspect of this collection of information, including suggestions for reducing this burden to Washington Headquarters Services, Directorate for Information Operations and Reports, 1215 Jefferson Davis Highway, Suite 1204, Arlington, VA 22202-4302, and to the Office of Management and Budget, Paperwork Reduction Project (0704-0188), Washington, DC 20503</p>			
1. AGENCY USE ONLY (Leave blank)	2. REPORT DATE	3. REPORT TYPE AND DATES COVERED	
	SEPTEMBER 2001	Final Report, 09/15/1996 – 04/18/2001	
4. TITLE AND SUBTITLE MATERIALS DEVELOPMENT RESEARCH		5. FUNDING NUMBERS	
6. AUTHOR(S) Emmanuel E. Boakye, Ph.D., Pavel Mogilevsky, Ph.D., Peter M. Hazzledine, Ph.D., T.A. Parthasarathy, Ph.D., Kristin A. Keller, M.S., M. Dennis Petry, M.S., Young-Won Kim, Ph.D., Satish I. Rao, Ph.D., Tai-Il Mah, Ph.D., Oleg N. Senkov, Ph.D., Madan G. Mendiratta, Ph.D., Jonathan E. Spowart, Ph.D., Sarath K. Menon, Ph.D., and Christopher F. Woodward, Ph.D.		C: F33615-96-C-5258 PE: 62102F PR: 2306 TA: B0 WU: 02	
7. PERFORMING ORGANIZATION NAME(S) AND ADDRESS(ES) UES, INC. 4401 DAYTON-XENIA ROAD DAYTON, OH 45432-1894		8. PERFORMING ORGANIZATION REPORT NUMBER UES-P157-001	
9. SPONSORING / MONITORING AGENCY NAME(S) AND ADDRESS(ES) MATERIALS AND MANUFACTURING DIRECTORATE AIR FORCE RESEARCH LABORATORY AIR FORCE MATERIEL COMMAND WRIGHT-PATTERSON AIR FORCE BASE, OH 45433-7750 POC: CPT G. BRANDT MILLER, AFRL/MLLM, (937) 255-1310		10. SPONSORING / MONITORING AGENCY REPORT NUMBER AFRL-ML-WP-TR-2001-4148	
11. SUPPLEMENTARY NOTES			
12a. DISTRIBUTION / AVAILABILITY STATEMENT Approved for public release; distribution unlimited.		12b. DISTRIBUTION CODE	
13. ABSTRACT (Maximum 200 Words) <p>Research has been carried out in three materials systems: (1) <u>Advanced Metallics</u>: NbTi/silicides and gamma TiAl are being developed as high-temperature structural materials. The research included chemistry/processing/microstructure/property relations to provide a balance in mechanical properties and oxidation resistance. Fundamental studies on microstructures and mechanical behavior in these systems have been performed using a variety of analytical and computational tools to predict aspects of plasticity, creep and fracture on length scales connected to electronic, atomistic, and continuum levels. (2) <u>Advanced Metallic Composites</u>: Deformation, fracture, and creep studies have been performed on discontinuously reinforced Al and Ti composites. Projects have been initiated on 1) microstructural simulation in these composites, and 2) crystallization kinetics and topology-based models for amorphous Al alloys. (3) <u>Ceramic Composites</u>: Research has been conducted on a number of interrelated projects, including interface control, experimental mechanics and models, new composite systems, processing, and structure-property understanding.</p>			
14. SUBJECT TERMS: Nb & Mo/silicides, gamma TiAl, multiplayer and nanocrystalline metallic materials, computation materials science, discontinuously reinforced metallic composites, amorphous Al alloys, ceramic composites		15. NUMBER OF PAGES 138 16. PRICE CODE	
17. SECURITY CLASSIFICATION OF REPORT Unclassified	18. SECURITY CLASSIFICATION OF THIS PAGE Unclassified	19. SECURITY CLASSIFICATION OF ABSTRACT Unclassified	20. LIMITATION OF ABSTRACT SAR

NSN 7540-01-280-5500

Standard Form 298 (Rev. 2-89)
 Prescribed by ANSI Std. Z39-18
 298-102

TABLE OF CONTENTS

<u>SECTION</u>		<u>PAGE</u>
	List of Figures.....	ix
	List of Tables.....	xi
	FOREWORD	xii
1	INTRODUCTION	1
2.	TASK I. ADVANCED METALLICS	2
2.1	ADVANCED INTERMETALLICS.....	2
2.1.1	Final Evaluation of the Five-Component Nb-Ti-Cr-Al-Si Alloys	2
2.1.2	Microstructural Effects of Higher Order Alloying Additions in the Five Component Base Alloy in the Nb-Ti-Cr-Al-Si-X (X=Mo, Ta, W) Alloys Systems.....	3
2.1.3	The Effect of Varying Hf, Cr, Al, and Si Concentrations on Microstructural Modifications in a Nb-Ti-Hf-Cr-Al-Si Alloy Developed at GE-CRD.....	3
2.1.4	Continued Screening Studies Within the Nb-Ti-Hf-Cr-Al-Si Family of Alloys to Optimize the Compositions for Turbine Blades	3
2.1.5	Evaluations of Nb-Ti-Hf-Cr-Al-Si-X Alloys for Improved Oxidation Resistance	4
2.1.6	Environmental Resistance of Nb-Ti-Hf-Cr-Al-Si-X Alloys	4
2.1.7	Mechanical Property Evaluation of a Baseline Nb-Ti-Hf-Cr-Al-Si Alloy.....	4
2.1.8	Selection and Characterization of Second-Generation Nb-Ti-Hf-Cr-Al-Si-X Alloys.....	5
2.1.9	Study of Oxidation Mechanisms in Nb-Ti-Hf-Cr-Al-Si-X Alloys	5
2.1.10	High Temperature Oxidation Mechanisms in Nb - Silicide Bearing Multicomponent Alloys.....	6
2.1.11	Oxidation Behavior of α Mo-Mo ₃ Si-Mo ₅ SiB ₂ (T2) Three-Phase System	8
2.1.12	Basic Oxidation Mechanisms in Mo-Si-B Ternary Alloys.....	8
2.1.13	Effect of Alloying Additions on the Phase Equilibria and Oxidation in the Mo-Si-B System.....	9
2.1.14	MoSi ₂ Barrier Coating on Mo-Si-B Alloys	11
2.1.15	Mechanical Properties of the Mo-Si-B Alloys	11
2.2	TiAl ALLOYS: DEVELOPMENT, PROCESSING, AND EVALUATION	12
2.2.1	Introduction of Research Programs	12
2.2.2	K5 Alloys: Design and Evaluation.....	13
2.2.2.1	Alloy Chemistry Modification.....	13
2.2.2.2	Microstructure Control and Process Development.....	14
2.2.2.2.1	Control by TMT Methods	14
2.2.2.2.2	Control by TMP Methods	14
2.2.2.2.3	Stabilization Treatments	15
2.2.2.2.4	Multistep Forming Experience.....	15
2.2.2.3	Mechanical Properties	16

TABLE OF CONTENTS (CONTINUED)

<u>SECTION</u>	<u>PAGE</u>
2.2.2.3.1 Tensile Properties	16
2.2.2.3.2 Fracture Toughness	17
2.2.2.3.3 Fatigue Resistance.....	17
2.2.2.3.4 Fatigue Cracking Threshold	17
2.2.2.3.5 Creep Resistance.....	18
2.2.2.3.6 Creep Crack Growth (CCG).....	18
2.2.3 Microalloying and GS Effect of Creep Behavior	18
2.2.4 Effect of Boron on Grain Refinement and Lamellar Formation.....	19
2.2.5 Production and Evaluation of K5 Alloy Sheet.....	20
2.2.6 Evaluation of IHPTE Rotor/Disk Alloys	20
2.2.6.1 Characterization of Alloy 395-M.....	20
2.2.6.1.1 Evaluation of Alloy 395-M.....	20
2.2.6.2 Evaluation of Alloy 395MM.....	21
2.2.7 High-Temperature Gamma Alloy Development.....	21
2.2.8 Summary of Other Efforts.....	22
2.2.8.1 Automotive Valve Program.....	22
2.2.8.2 Control of Casting Microstructures.....	22
2.2.8.3 Collaborations	23
2.3 TiAl: FUNDAMENTAL STUDIES	23
2.3.1 Phase Field Model for the Formation of the Lamellar Structure in Ti-Al	23
2.3.2 The Properties of the Unit <110>/2 Dislocation in Ti-Al	23
2.3.3 The Yield Stress of Lamellar TiAl.....	24
2.3.4 Creep FL TiAl Alloys - Review and Identification of Critical Variables	24
2.3.5 Lamellar Spacing Effect in Creep of Polycrystal FL TiAl Alloys	25
2.3.6 Creep Anisotropy of PST and Its Relation to Creep of Polycrystal FL.....	25
2.3.7 Microstrain Stress-Strain Behavior of PST and FL TiAl Alloys	26
2.4 MULTILAYERS AND NANOCRYSTALLINE MATERIALS	26
2.4.1 The Strongest Size for Nanocrystalline Copper.....	26
2.4.2 Dislocation Nucleation as an Alternative to Multiplication.....	27
2.4.3 Yield Strength of a Semicoherent Metallic Multilayer	27
2.4.4 Zener Pinning by Equiaxed and Shaped Particles	28
2.5 THEORECTICAL STUDIES AND COMPUTATIONAL MATERIALS SCIENCE.....	29
2.5.1 Methods.....	29
2.5.1.1 Green's Function Boundary Conditions in Atomistic Simulations	29
2.5.1.2 Predicting Trends in Ternary and Higher Order Phase Diagrams	29
2.5.1.3 First Principles Green's Function Boundary Condition Method	30
2.5.1.4 Scalable Parallel Electronic Structure Methods	30
2.5.1.5 Scalable Parallel Atomistic Methods.....	30

TABLE OF CONTENTS (CONTINUED)

<u>SECTION</u>	<u>PAGE</u>
2.5.2 Infrastructure	31
2.5.3 Applications	32
2.5.3.1 Atomistic Simulations of Dislocation-Interface Interactions in Cu-Ni Nanolayers.....	32
2.5.3.2 Atomistic Simulations of Dislocation-Interface Interactions in Cu-Cu Twinned Nanolayers	33
2.5.3.3 Dislocation-Interface Interactions in α Ti- β Ti.....	33
2.5.3.4 Frank-Read Source Simulation.....	33
2.5.3.5 Self-Energy of Small Loops	34
2.5.3.6 Core Structure and Mobility of a/2[111] Screw Dislocation in BCC Mo.....	34
2.5.3.7 Cross-Slip of a/2[110] Screw Dislocation in Model FCC Structures.....	35
2.5.3.8 Cross-Slip Obstacles on a/2[110] Screw Dislocation in L10 TiAl	35
2.5.3.9 The Influence of Solid Solutions on Flow Behavior in γ -TiAl	36
2.5.3.10 First Principles Simulation of Deformation Modes in Refractory Metals	37
2.5.3.11 First Principles Simulation of Deformation Modes in Intermetallics.....	37
2.5.3.12 First Principles Simulation of Metal/Oxide Interfaces.....	38
2.5.3.13 Predicting Solubility and Trends in Ternary and Higher Order Phase Diagrams Using the Dilute Solute Model.....	39
2.5.3.14 The Hierarchy of Planar Fault Energies in γ TiAl	39
2.6 PUBLICATIONS.....	40
2.7 PRESENTATIONS.....	46
2.8 INVENTION DISCLOSURE/PATENTS	52
2.9 BOOKS CHAPTER.....	52
2.10 CONFERENCE PROCEEDING EDITED.....	52
2.11 AWARDS	53
2.12 REFERENCES	54
3. TASK II. ADVANCED METALLIC COMPOSITES.....	57
3.1 MAJOR FINDINGS	57
3.1.1 Discontinuously Reinforced Aluminum Composites (DRA).....	57
3.1.1.1 Fracture Toughness Testing of DRA Materials.....	57
3.1.1.2 Enhanced-Toughness DRA.....	57
3.1.1.3 Analytical Modeling of Deformation and Fracture in DRA.....	58
3.1.1.4 Characterization of Spatial Heterogeneity in DRA.....	58
3.1.2 Fiber-Reinforced Titanium Matrix Composites (TMC).....	58
3.1.2.1 Longitudinal Tension Testing of TMCs	58
3.1.2.2 Transverse Tension Testing of TMCs Using Cruciform Specimen Geometry.....	59
3.1.2.3 Creep Behavior of TMCs.....	60

TABLE OF CONTENTS (CONTINUED)

<u>SECTION</u>	<u>PAGE</u>
3.1.2.4 Fatigue and Interfacial Effects in TMCs.....	60
3.1.2.5 Development of New Fiber Coatings for Optimized Mechanical Properties in TMCs.....	60
3.1.3 Fiber-Reinforced Orthorhombic Titanium Matrix Composites (OTMCs).....	61
3.2 CURRENT WORK.....	62
3.2.1 Discontinuously Reinforced Aluminum (DRA) Composites.....	62
3.2.1.1 Effect of Degassing on Mechanical Properties of a DRA Composite	62
3.2.1.2 Microstructural Characterization and Simulation.....	62
3.2.2.3 Effect of Particle Morphology on Mechanical Properties of DRA.....	62
3.2.2 Discontinuously Reinforced Copper (DRCu) Composites	63
3.2.3 Amorphous Aluminum	63
3.2.3.1 Crystallization Kinetics of an Amorphous Al-based Alloy	63
3.2.3.2 Compaction of an Amorphous Powder	63
3.2.3.3 Topology-Based Structural Models for Amorphous Metals	63
3.3 PUBLICATIONS.....	64
3.4 INVENTION DISCLOSURE/PATENTS	67
3.5 BOOKS	67
3.6 AWARDS	67
3.7 REFERENCES	68
4.0 TASK III. CERAMIC COMPOSITES.....	69
4.1 SUMMARY OF MAJOR FINDINGS	69
4.1.1 Interface Control	70
4.1.1.1 Easy Cleaving Oxides: Hexaluminates.....	70
4.1.1.2 Weakly Bonded Interface: Monazite	70
4.1.1.2.1 Coating on Sapphire Monofilaments.....	71
4.1.1.2.2 Coatings on Nextel TM 720 and 610 Fiber Tows	71
4.1.1.2.3 Effect of Process Variables on Coated-Fiber Tensile Strength.....	71
4.1.1.2.4 Monazite Coating without Fiber Strength Degradation	72
4.1.1.3 Fugitive Coatings	72
4.1.1.4 Porous Coatings	73
4.1.1.4.1 Porous ZrO ₂ -SiO ₂	73
4.1.1.4.2 Porous Rare-Earth Aluminate Fiber Coatings	74
4.1.1.5 Others.....	74
4.1.2 Experimental Mechanics and Models	74
4.1.2.1 Evaluation Protocol: Micro and Mini-CMCs	74
4.1.2.1.1 Fiber Strength.....	75
4.1.2.1.2 Micro-CMCs.....	75
4.1.2.1.3 Mini-CMCs	76
4.1.2.1.4 CMC Panels	76

TABLE OF CONTENTS (CONTINUED)

<u>SECTION</u>	<u>PAGE</u>
4.1.2.2 Test and Models to Understand/Evaluate Interface Behavior.....	77
4.1.2.2.1 Crack Deflection.....	77
4.1.2.2.2 Progressive Debonding with Roughness.....	78
4.1.2.2.3 Fiber Coating Thermoelastic Effects	78
4.1.2.2.4 Interface Debond Crack and UTS of CMC	78
4.1.3 Identify and Evaluate New System.....	79
4.1.3.1 Single-Crystal Yttrium Aluminum Garnet (YAG).....	79
4.1.3.2 Alumina-YAG Eutectic Polycrystal.....	79
4.1.4 Ceramic Composite Processing.....	79
4.1.4.1 CMCs with Fugitive Coatings	80
4.1.4.2 CMCs with Oxide Coatings	80
4.1.5 Structure-Property Understanding.....	81
4.1.5.1 Characterization and Experimental Techniques.....	81
4.1.5.2 Long-Term Effects and Environmental Stability.....	82
4.1.5.3 Design Issues.....	84
4.1.6 Miscellaneous.....	85
4.1.6.1 Review of Structural Ceramic Composites.....	85
4.1.6.2 In Situ Reinforced Mullite.....	85
4.1.6.3 Processing of YAG.....	85
4.1.6.4 SiC/MoS ₂ Nanocomposite.....	86
4.2 SUMMARY OF CURRENT WORK NOT REPORTED.....	86
4.2.1 Oxide CMC	86
4.2.1.1 Microstructural Evolution of Monozite Coatings for Oxide-Oxide Ceramic Composites: From Processing Sols to Minicomposites.....	86
4.2.1.2 Microstructural Characterization of COI Nextel TM 720/Monazite/AS Composites	89
4.2.1.3 Effect of Long-Term, High-Temperature Exposures on Nextel TM 610/Monazite/Alumina Composites	94
4.2.1.4 Tow Weavability	95
4.2.1.5 Commercial CMC Characterization for Thermal Gradient Exposure.....	95
4.2.1.6 Porous Matrix Composite Processing.....	96
4.2.1.7 Nextel TM 610/Alumina-YAG Composites	97
4.2.1.8 Nextel TM 650 Fiber Characterization.....	97
4.2.1.9 Dense Matrix Processing through Reaction Bonding	97
4.2.2 Nonoxide CMCs.....	98
4.2.2.1 Monazite Coatings of Tyranno TM -SA Tows	98
4.2.2.1.1 Effects of Sol Concentration on Coating Uniformity	98
4.2.2.1.2 Oxidation Protection.....	99
4.2.2.1.3 Filament Tensile Strength.....	100

TABLE OF CONTENTS (CONTINUED)

<u>SECTION</u>		<u>PAGE</u>
4.2.2.2	Monazite Coatings of Sylramic TM , Tyranno TM -SA, Hi-Nicalon TM , and Hi-Nicalon TM -S: Coating Retention.....	101
4.2.2.3	Application of Monazite Coatings in SiC/SiC Composites.....	103
4.2.2.4	Ube SiC/SiC – Stress-Rupture Tests	107
4.2.3	Miscellaneous	107
4.2.3.1	Failure and Deformation Mechanisms in Scheelite.....	107
4.2.3.2	Analyses of Hysteresis Loop to Extract Interface Roughness Parameters.....	108
4.2.3.3	Fracture Toughness Measurement of Fiber.....	109
4.2.3.4	Fugitive Liquid Phase Sintering of Alumina.....	109
4.2.3.5	CVD Processing of Alumina Matrix	110
4.2.3.6	Microstructure of Pure and Doped YAG Fibers Produced by Containerless Method.....	111
4.2.3.7	Doped Alumina-YAG Eutectic Polycrystals.....	111
4.2.3.8	Melt Growth of Piezoelectric Ceramic Fibers	113
4.2.3.9	Lanthanum Aluminate Single-Crystal Continuous Fiber Growth for Superconductor Substrate.....	114
4.3	PUBLICATIONS.....	114
4.4	PATENTS	119
4.5	BOOK CHAPTERS	119
	List of Acronyms.....	121

LIST OF FIGURES

<u>FIGURE</u>	<u>PAGE</u>	
1	Computational Scaling of the Parallel Atomistics Algorithm Developed at LLL in Collaboration with the CMS Group at AFRL.....	31
2	Isosurface Charge Density Plot of the Charge Density Near an $a/2<110]$ Screw Dislocation in L_{10}TiAl	38
3	TEM Micrograph and Schematics Showing the Arrangement of Rhabdophane Nanocrystals in the Coating Sol.....	87
4	TEM Micrograph and Schematics of the Microstructure of As-deposited Monazite Coating on Nextel TM 610 Fiber.....	87
5	COI Nextel TM 720/Monazite/AS Composite As-fabricated at 2100 °F	88
6	[100] Pole Figure Collected from Individual Grains in Monazite Coating in Nextel TM 610/Monazite/ Al_2O_3 Minicomposite after Heat Treatment at 1200 °C for 100 hrs.....	88
7	Schematic of Microstructural Development of Monazite Fiber Coatings in Oxide-Oxide Ceramic Composites	89
8a	TEM Micrograph Showing Preferred Orientation of the Coating in the As-Fabricated COI Nextel TM 720/Monazite/AS Material.....	90
8b	Grain Growth and Apparent Loss of Crystallographic Orientation in the Same Material after Heat Treatment at 2200 °F	90
9	TEM Micrograph Showing Partial Infiltration of Silica and an Al_2O_3 Particle Dragged into the Monazite in the As-Fabricated COI Nextel TM 720/Monazite/AS Material.....	91
10a	TEM Micrographs Showing Spheroidization and Formation of Isolated Discontinuous Grains of Monazite in Thin Coatings	92
10b	Formation of Thicker Dense Uniform Coatings in COI Nextel TM 720/Monazite/AS Material After Heat Treatment at 1200 °C for 100 Hours.....	92
11	CBED Pattern from Monazite and HRTEM Image of the Monazite/Fiber Interface Confirming the Thermodynamic Stability of Monazite in COI Nextel 720/Monazite/AS Material After Heat Treatment at 1200 °C for 100 Hours.....	93
12	Tensile Test Results for Oxide-Oxide CMCs.....	94
13	PVA Sizing of Coated Nextel TM 720 Showing: (a) Filaments Bundled Together and (b) PVA Crust.....	95
14	SEM Micrographs of Monazite Coating on Tyranno-SA Fiber with (a) No Crusting and (b) Crusting	99
15	SEM Micrographs of Tyranno-SA Heat Treated in Air at 1200 °C/10 Hours: (a) Without and (b) With Coatings	100
16	Tensile Filament Strength of Heat-Treated Monazite Coated Tyranno TM -SA Fiber Versus Silica Film Thickness	101

LIST OF FIGURES (CONTINUED)

FIGURE		PAGE
17	Monazite Coating on (a) Sylramic TM , (b) Tyranno TM -SA, .(c) Hi-Nicalon TM and (d) Hi-Nicalon TM -S.....	102
18	Surface Roughness of Sylramic TM , Tyranno TM -SA, Hi-Nicalon TM and Hi-Nicalon TM -S.....	102
19	TEM Micrographs Showing Fiber/Coating/Matrix Interfaces in the Sylramic TM /Monazite/CVD-SiC (Hypotherm) Material.....	104
20	EDX Maps and Spectra Showing the Extent of Chemical Reaction at Fiber/Coating/Matrix Interfaces in the Sylramic/Monazite/CVD-SiC (Hypotherm) Material.....	105
21	A TEM Image of the Fiber/Matrix Interface in the BF Goodrich Sylramic TM /Monazite/CVD SiC Material (a), and EDX Spectra from the Matrix (b).....	105
22	TEM Micrograph of a Hi-Nicalon TM /Monazite/CVI SiC Mini-CMC Showing the Presence of Monazite Grains at the Fiber-Matrix Interface.....	106
23	TEM Images of the Fiber/Matrix Interface in ORNL Tyranno TM SA/Monazite/CVD-SiC Material.....	106
24	Results of Intermediate Temperature Gradient Test on UBE Minicomposites.....	107
25a	(001) Cleavage Accompanied by Slip Along (114) Plane Resulting in the Offset of the Cleavage Plain by Nine Lattice Unit Cells in the [001] Direction.....	108
25b	(001) Cleavage Combined with Periodic Kinks in the (011) Plane, Resulting in the Average Cleavage Plane Deviating from (001) by About 4 to 5°.....	108
26	The Hysteresis Data Obtained on Various Micro-CMC and Mini-CMCs.....	109
27	The Minicomposites Fabricated Using Monazite as Interlayers In Nextel TM 610-Reinforced CVI Alumina Matrix Mini-CMCs	111
28	Flexural (4-pt) Strength of AYE Polycrystal with, and without Dopant	112
29	SENB Fracture Toughness of AYE Polycrystal with, and without Dopant	113

LIST OF TABLES

<u>TABLE</u>		<u>PAGE</u>
1	Composition of Quaternary Mo-Si-B-X and Quinary Mo-Si-B-X-Y Alloys	10
2	K5-Series Alloy Compositions (at.%).....	13
3	Tensile Filament Strength of TyrannoTM-SA Coated Fiber	100

FOREWORD

This report was prepared by the Materials and Process Division of UES, Inc., Dayton, Ohio under Air Force Contract F33615-96-C-5258. Captain Wayne Meyer and Captain G. Brandt Miller of the Air Force Research Laboratory (AFRL), Materials and Manufacturing Directorate (ML), Metals, Ceramics and Nondestructive Evaluation Division, Materials Development Branch, were the Government Project Engineers. The research reported herein covered the period 15 September 1996 to 18 April 2001.

1. INTRODUCTION

The structural integrity of many Air Force systems depend critically on the optimal performance of traditional materials and continued exploration/development of new material technologies. Two major requirements have driven new material technologies: (1) reduced weight of engineering components of aircraft, and (2) increased operating temperature of engines. Success in meeting these requirements will lead to improved performance efficiency and fuel cost savings. Material systems based on intermetallics, advanced metallic composites, and ceramic composites have great promise in fulfilling these requirements. While engineering developments based upon educated empirical approaches and accumulated experience must continue, the fundamental scientific understanding of material behavior at interlinked electronic, atomistic, and continuum levels is needed to provide a solid foundation for further advancements.

For the past 4 and a half years UES has carried out experimental and theoretical research on three different classes of materials. These include advanced metallics, advanced metallic composites, and ceramic composites. This is the final report on progress made on various topics within the three broad categories of material types. The report contains a summary of major findings, a description of current work not reported earlier, and a list of publications/presentation/patents/book chapters.

2. TASK I. ADVANCED METALLICS

2.1 ADVANCED INTERMETALLICS

During this reporting period, UES performed research on two refractory metal/intermetallic systems: Nb-Ti-Hf-Cr-Al-Si-X and Mo-Si-B-X. The first system consists of Nb Ti Hf Cr Al metal phase in equilibrium with the complex 5:3 silicides and Laves (Cr_2Nb) phases. The second system consists of refractory Mo metal phase in equilibrium with the silicide Mo_3Si and borosilicide Mo_5SiB_2 phases. Depending upon relative volume fractions and spatial distribution of the phases, these systems fall within the alloy classes termed as ductile/brittle or brittle/ductile. The first class consists of a ductile metal matrix plus dispersed brittle intermetallics phases, while the second consists of brittle intermetallic matrix and dispersed metal phase. These multiphase systems have a potential to provide a balance in properties for high-temperature structural applications. The intermetallic phases can result in good high-temperature properties including oxidation, strength, and creep while the metal phases can provide low-temperature toughness and damage tolerance.

The two systems described above are candidates for hot-section jet engine components, e.g., turbine blades and combustors under the (DoD) Integrated High Performance Turbine Engine Technology (IHPTET) program. The IHPTET goals include a temperature capability to exceed that for the best single-crystal Ni base super alloys by ~ 150 °C for the turbine blade.

The research reported here includes composition effects on microstructure and oxidation, basic oxidation mechanisms, microstructural dependence of toughness, tensile strength, creep, and creep improvement based upon microstructural perspective. It should be pointed out that these research projects are ongoing with a long-range goal of using these two classes of materials in microlaminated airfoil design.

Following is a summary of major findings of various research projects on advanced intermetallics.

2.1.1 Final Evaluation of the Five-Component Nb-Ti-Cr-Al-Si Alloys

The objective of this ongoing effort was to investigate alloys containing a nominally oxidation-resistant (or oxidation tolerant), ductile, refractory phase in equilibrium with one or more refractory silicide intermetallic phases in order to evaluate their potential for a useful balance of structural properties. Work leading up to the present final characterization of the five component Nb-based alloys has been reported in our previous final technical report [1]. Extensive screening studies were conducted on alloys with 1:1 Nb/Ti ratio, 8 to 10 atomic (at.)% Cr, 10 at.% Al and 13 to 19 at.% Si. Typical microstructures in these alloys consisted of the beta phase as the continuous matrix, with one or more silicides as dispersed phases, whereas for high-temperature strength, a more desirable microstructure is one or more refractory silicides that are reinforced via a co-continuous mixture of a ductile refractory metal phase. Results on additional alloy compositions indicated that lowering the Cr and Al contents in the alloys may be beneficial toward obtaining a more co-continuous microstructure containing the beta and silicide phases. Bend strength versus temperature studies on selected alloys showed that, at

temperatures above 1000 °C, the beta + silicide alloys have superior strengths compared to baseline beta alloys as well as nickel-based superalloys, although the strengths are lower than the model Nb₅Si₃/Nb alloys.

2.1.2 Microstructural Effects of Higher Order Alloying Additions in the Five Component Base Alloy in the Nb-Ti-Cr-Al-Si-X (X=Mo, Ta, W) Alloy Systems

Higher order alloying modifications of Nb-Ti-Cr-Al-Si base alloy with Mo, Ta, W were pursued to obtain information about phase equilibria and elemental partitioning between the different phases. Phase equilibria studies at 1000 and 1400 °C showed the decomposition of the beta phase with resultant formation of (Nb,Ti)₃Al in the Mo-containing alloys, whereas no such decomposition was observed in the Ta- and W-containing alloys. Mechanical property data on these alloys showed noticeable strengthening at 1000 °C compared to the baseline alloys, although the absolute strength levels were still substantially below the strengths obtained for the model Nb₅Si₃/Nb alloys. The strength decrement again may be attributed to the beta phase being the continuous phase in all of these alloys.

2.1.3 The Effect of Varying Hf, Cr, Al, and Si Concentrations on Microstructural Modifications in a Nb-Ti-Hf-Cr-Al-Si Alloy Developed at GE-CRD

Work from General Electric Corporate Research and Development (GE-CRD) on a Directionally Solidified (DS) 47Nb-25Ti-8Hf-2Cr-2Al-16Si alloy had shown attractive properties in toughness, strength, and creep rupture. However, issues such as microstructural control and phase stability were still not addressed. Hence, a systematic study was conducted to delineate the effect of the various alloying additions on the GE alloy, particularly with respect to elemental partitioning, and morphology and distribution of the beta and the silicide phases. The results showed that Hf partitions predominantly to the silicide phases, while Cr and Al partition almost completely to the beta phase. Further, it was evident from the microstructural information that the phase distribution and solidification paths are very sensitive to the Cr, Hf, and Al concentrations. It was determined that the optimum compositions should have higher Nb, lower Ti, lower Cr, and lower Al than the alloys currently under investigation. The results from these studies were used to select three baseline alloys with compositions in the range (49 to 51)Nb, (24 to 26)Ti, (2 to 4)Cr, (2 to 4)Al, (0 to 4)Hf, and (15 to 16)Si for further evaluation (composition range given in at. %).

2.1.4 Continued Screening Studies Within the Nb-Ti-Hf-Cr-Al-Si Family of Alloys to Optimize the Compositions for Turbine Blades

The objective of this research was to evaluate Nb-Ti-Hf-Cr-Al-Si base alloys as viable candidates for long-term engineering service at temperatures beyond the current limit of superalloys. Alloys within this class represent one of the major development approaches being pursued for turbine blades within the IHPTET Phase III goals, and beyond. Systematic chemistry modifications were conducted within the multicomponent Nb-Ti-Cr(Hf)-Al-Si systems in an effort toward obtaining a co-continuous microstructure containing a ductile refractory beta phase and one or more refractory intermetallic silicides. The results indicated that lowering the Cr and Al contents in the alloys may produce such a

microstructure. Further evaluation was conducted on alloys with low Cr+Al concentration, specifically, alloys having compositions in the range (49 to 51)Nb, (24 to 26)Ti, (2 to 4)Cr, (2 to 4)Al, (0 to 4)Hf, and (15 to 16)Si. In the cast + 1500 °C heat treated condition, these alloys showed the formation of a metastable M₃Si-type phase. Upon hot forging at 1400 °C followed by subsequent heat-treatment at 1500°C, the metastable M₃Si phase undergoes a cellular or eutectoid decomposition to the equilibrium phases of beta and M₅Si₃ silicide. The results indicated that the microstructure in these alloys can be suitably tailored by choosing appropriate chemistries and/or processing techniques. Chemistries within this family were selected as the starting point for external development work at GE. Having this knowledge of phase equilibria, the researchers decided that further alloy development efforts would be based on increased Cr additions to introduce a Cr-rich Laves phase, within the same general microstructure. Such additions were viewed as necessary to further enhance the oxidation resistance.

2.1.5 Evaluations of Nb-Ti-Hf-Cr-Al-Si-X Alloys for Improved Oxidation Resistance

While alloys with the composition range (49 to 51)Nb, (24 to 26)Ti, (2 to 4)Cr, (2 to 4)Al, (0 to 4)Hf, and (15 to 16)Si represented major progress toward an Nb-base turbine blade alloy, still further improvements in oxidation resistance were required for the anticipated service environment. Higher order alloying modifications of Nb-Ti-Hf-Cr-Al-Si with Mo, Mo+B, Zr, Y, Re additions were centered on providing substantial further enhancement in the oxidation resistance. The initial results indicated that Mo, Zr and Y additions do not provide further improvements. Mo + B additions resulted in the formation of a Nb-Ti-Mo borosilicide phase which was similar in composition to the T2 phase observed in the Mo-Si-B system that was being investigated in separate studies. To evaluate the effect of boron on the Nb-silicide phase, compositions corresponding to the borosilicide phase in the Nb-Si-B, as well as Nb-Mo-Si-B systems, were evaluated for oxidation resistance. It was evident from the results that the Nb-base borosilicide phase did not provide improved oxidation resistance in the composite; however, the Nb-Mo base borosilicide appeared to show some promise.

2.1.6 Environmental Resistance of Nb-Ti-Hf-Cr-Al-Si-X Alloys

Alloys with Cr additions of ~15 at.% showed favorable oxidation behavior with metal recession rates of 0.8 to 1.1 µm/h (~0.03 to 0.05 mil/h) at 1200 °C. The microstructure of these alloys after heat-treatment of 1400 °C/100 h consisted of co-continuous beta with Nb₅Si₃ and Ti₅Si₃ silicides, together with the Cr₂Nb-based Laves phase. Based on these results, a second-generation Nb-base alloy with the composition Nb-10Ta-24Ti-4Hf-15Cr-3Al-14Si-5Ge was downselected for ingot processing.

2.1.7 Mechanical Property Evaluation of a Baseline Nb-Ti-Hf-Cr-Al-Si Alloy

A first-generation Nb alloy with the composition 42Nb-29Ti-4Hf-6Cr-2Al-17Si, an alloy procured from the Los Alamos National Laboratory (LANL), was extruded at 1400 °C. Specimens of the extruded LANL alloy was tested for mechanical properties. Room-temperature fracture toughness of this alloy ranged from 22 to 26 MPa√m. Tensile tests in air showed yield/fracture strengths that were comparable to the model binary alloy Nb-10Si over the temperature range from 25 to 1100 °C.

2.1.8 Selection and Characterization of Second-Generation Nb-Ti-Hf-Cr-Al-Si-X Alloys

Alloying studies were continued on Nb-Ti-Hf-Cr-Al-Si-X (X=Ta, Ge or Zr) alloys with a higher Cr content of ~15 at.%. The most promising additions appeared to be Ge and Zr for oxide scale stability. Additionally, the effect of chemistry modifications on oxidation was evaluated by varying the Cr concentration in the alloys. Alloys with Cr additions of ~15 at.% showed favorable oxidation behavior with metal recession rates of 0.8 to 1.1 $\mu\text{m}/\text{h}$ (~0.03 to 0.05 mil/h) under static conditions at 1200 °C. Cyclic oxidation that was conducted on two alloys at 1200 °C showed metal recession rates of 0.06 to 0.07 mil/h, with a total weight losses of ~120 mg/cm² after exposure for 200 h. Ta additions of ~10 at.% appeared to be desirable from the point of view of obtaining a co-continuous microstructure of beta + silicides. The microstructure of these alloys after heat treatment of 1400 °C/100 h consisted of co-continuous beta with Nb₅Si₃ and Ti₅Si₃ silicides, together with the Cr₂Nb-base Laves phase. Based on these data, a third-generation Nb-base alloy with the composition Nb-10Ta-24Ti-4Hf-15Cr-3Al-14Si-5Ge was procured from Pittsburgh Materials Technology, Inc., and extruded at 1400 °C, using a 6:1 extrusion ratio. The extrusion was full of cracks; therefore, tensile specimens could not be machined from the extrusion. A few tensile creep specimens were obtained and tested at 1100 and 1200 °C. The initial data showed creep rates that were an order of magnitude higher than those for binary Nb-10Si. However, the data may be unreliable, as defect-free specimens could not be obtained.

Based on an earlier alloy (26Nb-22Ti-8Ta-4Hf-15Cr-2Al-18Si-5Zr; Alloy 1942) which showed the best cyclic oxidation life (140 h of weight gain at 1200 °C), an alloy with the composition 31Nb-26Ti-8Ta-4Hf-12Cr-2Al-12Si-5Zr (Alloy 1329) was obtained as an ingot. In this alloy, the Cr was lowered from 15 to 12 percent for obtaining crack-free cast ingots, and the Si was lowered to 12 percent (based on Austin Chang's phase equilibria predictions for primary beta phase dendrite formation and to avoid formation of large Nb₅Si₃ faceted dendrites which were seen in Alloy 1942). The plan was to extrude this alloy for mechanical property evaluation.

2.1.9 Study of Oxidation Mechanisms in Nb-Ti-Hf-Cr-Al-Si-X Alloys

To date, empirical alloying schemes have been successful in identifying pathways toward obtaining reasonable oxidation resistance in the Nb-base alloys. However, there is still a lack of fundamental understanding as to the operative mechanisms for oxidation protection. Research was initiated toward identifying some of these oxidation mechanisms through a systematic study of oxidation kinetics followed by a detailed characterization of oxide scale composition and structure. Gravimetric oxidation studies were initiated on selected alloys (Alloy 1870: Nb-10Ta-24Ti-4Hf-14Cr-2Al-13Si-5Ge and LANL: Nb-28Ti-4Hf-6Cr-2Al-17Si) in an effort to understand scale growth kinetics. In the initial oxidation exposures of alloy 1870, continuous weight gain/loss of alloys was monitored during exposures at 1200 °C for various times ranging from a few hours to ~80 hours. Cross-sectional Scanning Electron Microscopy (SEM) was conducted on the oxidized specimens in an effort to understand the oxide scale characteristics. SEM (dot map) and x-ray diffraction (XRD) were conducted on the oxidized specimen surfaces to characterize the oxide scale type/composition. The weight change data showed two distinct regimes: (1) a steady weight gain at temperature, which may be indicative of parabolic oxidation kinetics, and (2) a rapid weight gain (~50 to 60 percent of total weight gain) during cooling through

1200 to 900 °C for specimens exposed from 5 to 40 hours. SEM (dot map) of the oxide scale surface indicated the following: (a) No Ge in the scale, (b) presence of (Nb, Ta, Cr)-rich regions [Cr(Nb,Ta)_xO₄ niobates] and Ti-Cr rich regions (CrTiO₄).

A preliminary study initiated on a Nb-21 at.%Ti-15 at.%Si-13 at.%Cr-4 at.%Cr-4 at.%Ge-2 at.% Al-3 at.%B showed that oxidation at 800 °C and 1200 °C led to vastly different microstructures. Though nonadherent oxide mixtures containing TiO₂ and Nb₂O₅ form as an outer oxide at both these temperatures, adherent oxide mixtures containing TiO₂ and lower Nb oxides form below the oxide scale. All of the solid solution regions in the microstructure are apparently oxidized to mixtures of oxides while only the outer layers of the silicide phase are oxidized at 1200 °C. Oxygen diffusion at 1200 °C is substantial, and internal oxidation produces HfO₂ precipitates well inside the alloy. The subsurface layer formed at 800 °C was found to be constituted of Nb₂O₅ precipitates in the solid solution regions, with the silicides being virtually unattacked. The formation of Nb₂O₅ precipitates in the subsurface region leads to catastrophic cracks parallel to the surface of the alloy. Further studies to understand the mechanisms of these reactions will be explored in detail.

2.1.10 High Temperature Oxidation Mechanisms in Nb - Silicide Bearing Multicomponent Alloys

A fundamental understanding of the influence of chemistry and microstructure on the nature, sequences, and mechanisms of oxidation of multicomponent Nb alloys at various temperatures is crucial in any effort on Nb alloy development. This study was undertaken with this objective and oxidation of a variety of multicomponent Nb-based alloys was studied and the role of alloying additions critically examined. In particular, the kinetics of oxidation of a number of alloys was determined by following the weight changes during cyclic oxidation. A Nb-25Ti-18Si-6Cr-2Al-2Hf-0.5Sn alloy was chosen as the base alloy for comparison, and the effect of substitution of a part of Si with Ge and a part of Cr with Fe was examined. The role of small amounts of Ce (0.1 at.%) and B (2 at.%) were also examined. The influence of Si was examined by adding up to 5% Si to the base alloy. The results of these alloying effects on oxidation can be summarized as:

- (1) All alloys show a two-stage oxidation reaction with an initial weight gain region, followed by a rapid weight loss region. The second stage can be described as a breakaway oxidation reaction where rapid oxidation and oxide spallation occur. The onset of the breakaway oxidation is strongly temperature dependent and occurs earlier in time as the temperature is raised.
- (2) Replacement of Si with 5 at.% Ge appears to have a very remarkable influence with the onset of breakaway oxidation, which is delayed by at least an order of magnitude in time.
- (3) Replacement of Cr with Fe, or adding B may have a detrimental effect in oxidation resistance. The oxide scales in the latter two alloys tend to break up into fine powder rather than stay as a compact sheet. The positive effect of Ge appears to be somewhat lost when part of Cr is replaced with Fe.

The results of the microstructural studies can be summarized as:

- (1) In general, the equilibrium compositions of the phases varied only slightly between different heat-treatment temperatures, suggesting that the phase boundaries are quite steep in this region of the multicomponent phase diagram.
- (2) The solubility of Si as well as Ge in the solid solution is very low, while a substantial amount of Cr and most of the Sn remains in the solid solution.
- (3) The two silicides may be easily distinguished from their compositions as the Nb_5Si_3 -and the Ti_5Si_3 -type phases are associated with Nb/Ti atomic ratios of approximately 1.8 to 2.0 and 0.8 to 0.9, respectively.
- (4) Both of the silicides are enriched in Ge presumably substituting for Si in their crystal structures while Hf clearly shows preferential partitioning into the Ti_5Si_3 -type phase. These experimental observations are in conformity with expected alloying behavior based on their binary phase diagrams.
- (5) There is a substantial difference in the oxidation behavior of the β phase and the silicide phase. Oxygen diffuses through the β phase very rapidly and forms oxides, while it leaves the silicide phase virtually unattacked. It appears that oxygen permeability in Nb alloys has not been affected to the extent of obtaining an oxidation-resistant Nb solid solution. Grain boundaries and interfaces appear to assist the oxygen diffusion in the alloy.
- (6) The general mechanism of oxidation in these alloys seem to be controlled by oxygen dissolution in the β phase and precipitation of the oxide at the grain boundaries within the β phase and the β /silicide interfaces. Consequently, an adherent oxide scale forms on the alloy surface and oxidation continues.
- (7) During oxidation at temperatures below approximately 1000 °C, the surface of the alloy, just below the adherent oxide scale, contained numerous cracks (mostly in the silicide phase) parallel to and following the contour of the sample surface.

From all of the experimental results, it appears that the mechanism of oxidation of multicomponent alloys containing silicide is not changed to any extent by alloy chemistry, though the kinetics appear to be quite influenced. Clearly, oxygen diffusion into the β phase occurs rapidly, and due to the substantial solubility for oxygen even in the multicomponent alloys, alloy oxidation is quite rapid. Selective internal oxidation of alloying elements like Hf appear to occur due to their high thermodynamic stability. Oxygen solubility in the silicide phase appears to be quite limited, and so does oxygen diffusion. Oxygen diffusion is substantially aided by the internal defects in the alloy with the grain boundaries and phase boundaries acting as short-circuit diffusion paths. During these stages of oxidation, the kinetics of oxidation can be roughly described by a modified Wagner mechanism in which diffusion of oxygen through the oxide, as well as substantial dissolution of oxygen in the β phase, is considered and a cubic law can describe the weight change kinetics. As the reaction proceeds, rapid diffusion of oxygen through the oxide scale leads to a linear (or breakaway) stage of oxidation kinetics, aided by oxide scale spallation.

2.1.11 Oxidation Behavior of α -Mo-Mo₃Si-Mo₅SiB₂ (T2) Three-Phase System

The oxidation resistance of Mo can be significantly enhanced by additions of Si and B to produce the intermetallic phases Mo₃Si and Mo₅SiB₂ in equilibrium with the Mo phase. Initial cyclic-oxidation tests at 1200 °C revealed that a minimum of 11 at.%Si and 9 at.%B in Mo are required to make a significant improvement. The cyclic oxidation kinetics and microstructure of the oxide scales were investigated for the Mo-11 at %Si-11 at %B alloy from 600 to 1400 °C. This composition was cast and heat treated (1600 °C/24 h and 1700 °C/48 h) to produce a coarse three-phase microstructure containing ~37 vol% Mo phase in a two-phase intermetallic (Mo₃Si + Mo₅SiB₂) matrix. The overall oxidation behavior for the entire temperature regime was governed by a competition between volatilization of Mo as MoO₃ gas and the passivation provided by the formation of borosilicate glass (B-SiO₂) scale. At low temperatures (\leq 800 °C), even though the formation of the B-SiO₂ is thermodynamically favored, the MoO₃ phase grew very rapidly and its volatilization provided no protection. From 800 to 900 °C, the kinetics showed a rapid transient weight loss due to MoO₃ volatilization and, a steady-state weight loss associated with the formation of a porous outer B-SiO₂ scale and continuous escape of MoO₃ gas, thereby providing a limited oxidation protection. At and above 1000 °C, the oxide scale consisted of relatively solid and well-adherent outer B-SiO₂ scale and an inner reaction zone consisting of α -Mo and SiO₂ phases. In the temperature regime of 1000 to 1300 °C, there was a high degree of oxidation protection characterized by low transient- and steady-state weight losses. Preoxidation at 1300 °C beyond the transient stage (i.e., an exposure of 4 h) provided a significant oxidation protection at 800 °C.

2.1.12 Basic Oxidation Mechanisms in Mo-Si-B Ternary Alloys

To understand the mechanisms of oxidation of Mo-Si-B alloys, a systematic investigation was conducted. The oxidation kinetics of a pure silica-coated molybdenum were studied and compared with the kinetics of a Mo-reinforced B-Mo₃Si alloy under identical conditions in the temperature range of 500 to 800 °C. The results were analyzed to understand the rate-limiting processes in the different temperature range. The relative kinetics of silica-scale formation, oxidation of B, volatilization of B₂O₃, volatilization of MoO₃ and the viscosity of the B-SiO₂ were identified as key parameters that determine the kinetics of the oxidation of the alloy in the temperature range of 500 to 1300 °C. Based on initial results, the following was proposed and experiments conducted to answer key questions. During the transient stage there is evaporative loss of Mo as MoO₃ (gas). This is impeded and slowed significantly by the formation of silica. Full coverage of the surface is ensured by the fluxing of the silica by B₂O₃ that forms by oxidation of B. The lowered viscosity due to the presence of B₂O₃ must play a significant role in the coverage, since no protection is obtained in Mo-Si alloys of similar compositions with no B. Soon after the B-containing silica forms, the kinetics is slowed down to a parabolic weight change, presumably limited by oxygen diffusion through the silica scale. The further oxidation of Mo requires the permeation of gaseous MoO₃ through the scale. It is also known from ceramics literature that B₂O₃ is volatile above \sim 1100 °C. It is proposed that at 1300 °C, B₂O₃ is lost from the scale early, resulting in a low B-containing silica that has a sufficiently high viscosity to minimize MoO₃ permeation. At 800 °C, the B-rich silica scale is much less viscous, allowing MoO₃ to permeate by bubbling through the scale. B also is known to enhance oxygen diffusion in silica; thus the scale thickness is higher at 800 °C. From

the experimental results (weight change data), it was clear that there is a transition from parabolic weight loss to parabolic weight gain as the temperature is decreased from 800 °C to 500 °C, with a narrow temperature window around 700 °C where the weight loss is linear. At 650 °C, there is a linear weight loss, beyond a transient increase in weight. The higher temperature weight changes show a transient rapid weight loss. However, the low temperature regime does not show any transient. X-ray diffraction of the scales showed that the oxidation scale formed was solid MoO₃ at lower temperatures. There was no significant scale formation at 700 °C in the case of pure Mo. Comparing results on Mo and Mo-Si-B, it was seen that even when the scale is entirely MoO₃, the presence of Si and B in the alloy helps slow the kinetics of oxidation. A comparison of the data showed that the Mo-Si-B, is slightly superior even in the regime where no scale forms. The kinetics are parabolic weight gain below 700 °C and linear weight loss at and above 700 °C, consistent with the results obtained on the Mo-Si-B alloy. The critical temperature range where practically no protection exists, was identified as 700 to 750 °C. Attempts to improve the oxidation resistance of this system must focus on this temperature range [2].

2.1.13 Effect of Alloying Additions on the Phase Equilibria and Oxidation in the Mo-Si-B System

As described in the previous section, the oxidation resistance of the ternary Mo-Si-B compositions within the α Mo - Mo₃Si - Mo₅SiB₂ phase field is not adequate for the entire temperature range (600 to 1400 °C) for high-pressure turbine blade applications under the IHPTET program. Therefore, it was decided to explore whether selected alloying additions can significantly improve the oxidation behavior, particularly at low temperatures. The alloying elements investigated were W, Nb, V, Cr, Re, Ge, Al, Hf and Ti+Cr and a range of compositions were melted and heat treated to obtain information on phase equilibria at selected temperatures prior to oxidation exposures. The additions are listed in Table 1.

Table 1. Compositions of Quaternary Mo-Si-B-X and Quinary Mo-Si-B-X-Y Alloys

Element	Composition/Composition Range (Atomic Percent)
W	Mo-7.5 to 30W - 15 to 19.5Si - 5 to 10B
Nb	Mo-30Nb-30Si-10B
V	Mo-20 to 30V - 12 to 30Si - 6 to 10B
Cr	Mo-20Cr-12Si-10B
Re	Mo-7.5 to 23Re - 7.5 to 20 Si-10B
Ge	Mo-5Ge-11Si-8B
Al	Mo-5Al-11Si-11B
Hf	Mo-0.3 to 10Hf - 9 to 12Si - 9 to 12B
Ti+Cr	Mo-18Ti-11Cr-9Si-9B

The important findings of the effects of alloying additions to the base composition on phase relations and oxidation behavior are summarized below.

- (1) For W and Nb additions, it is possible to obtain a phase equilibrium consisting of the metal phase + 5:3 silicide + T2; however, this requires high levels of W (~ 30 at.%) and Nb (~ 25 at.%). The oxidation resistance for these high W- and Nb-containing compositions is significantly inferior to the base Mo-11Si-11B, most probably due to selective oxidation of W and Nb, thus, interfering with the formation of a continuous and protective B-SiO₂ glass. For lower W contents, i.e., in the metal + 3:1 silicide + T2 phase field, the oxidation resistance is also inferior to the base ternary alloy (Mo-11 at.% Si-11 at.%B) at both 800 and 1300 °C. Lower Nb contents have not been investigated.
- (2) For Cr and V additions, the phase relations showed the existence of two three-phase fields: metal + 3:1 silicide + T2 and 3:1 silicide + T2 + 5:3 silicide. For no composition, it is possible to obtain metal + T2 + 5:3 silicide equilibrium. At 800 °C, all Cr- and V-containing alloys exhibited worse oxidation resistance than that for the base ternary. At 1300 °C the quaternary alloys exhibited oxidation resistance somewhat similar to that of the ternary alloys.
- (3) Re additions produced complex phase relations and stabilized the intermetallic σ (MoRe) phase. Phase equilibria indicate the existence of a three-phase field: metal + 3:1 silicide + T2, and, two four-phase fields: metal + 3:1 silicide + T2 + σ and 3:1 silicide + T2 + σ + 5:1 silicide. Limited oxidation experiments showed that Re additions were not beneficial for oxidation resistance.
- (4) Small amounts of Ge and Al additions studied did not alter the basic ternary Mo-Si-B phase equilibria. Oxidation resistance was found to be inferior in these compositions as compared to that in the ternary Mo-Si-B composition.

(5) A number of Hf additions were explored at two different Si + B levels. At all levels, Hf additions did not improve the oxidation protections.

Thus, the most significant finding is that all alloying additions explored did not produce a better oxidation-resistant-composition than the base ternary Mo-Si-B alloy. In fact, almost all alloying additions made the oxidation behavior significantly worse, leaving the ternary base alloy system with the best overall behavior achieved to date. It is possible that other alloying elements (e.g., rare-earth additions) might be worth exploring, however, it is not clear whether there is any scientific rationale for selection.

2.1.14 MoSi₂ Barrier Coating on Mo-Si-B Alloys

Since there is, at present, no obviously reasonable alloying approach for enhanced oxidation resistance beyond the behavior of the ternary base alloy, it was decided to explore application of an oxidation-resistant coating. A simple chemical vapor deposition (CVD) process was used to enrich the surface of a Mo-11Si-9B sample with Si. The base alloy was heat treated for homogenization at 1550 °C for 100 h, followed by 1400 °C for 100 h in argon. A coupon, ~ 5-mm cube, machined from the heat-treated alloy, was encapsulated in an evacuated quartz tube together with 1 g Si powder and 20 mg ammonium chloride and annealed at 850 °C for 10 h. This process produced a fairly uniform coating, ~ 25 µm thick. Energy dispersive analysis (EDX) and x-ray diffraction revealed this coating to be MoSi₂. The coated coupon and an uncoated coupon were subjected to cyclic oxidation at 800 °C for 200 h, followed by cyclic oxidation at 1300 °C for additional 200 h. The coated sample survived all of the cycles with virtually no loss of weight. In comparison, the uncoated sample exhibited considerable weight loss. Thus, a simple coating process (which has not been optimized yet) provides a high degree of protection.

As mentioned earlier, it is possible that the ongoing development efforts will not succeed in achieving adequate oxidation resistance in the Mo-Si-B-X alloys. Therefore, if the surface coating has to provide the only significant protection in service, then such coating has to be the prime reliant coating. This means that the coating should be highly reliable and durable, i.e., it should not fail under complex thermomechanical loading and environmental cycles present in a turbine engine. This necessitates further work on coating optimization and testing for reliability and durability. Such effort is presently underway.

2.1.15 Mechanical Properties of the Mo-Si-B Alloys

Limited work was done to measure the bend strength and fracture toughness, K_Q of nonconsumable arc-melted and heat-treated Mo-12Si-12B and consumable arc-melted and extruded (1800 °C, 4:1 ratio) and heat-treated Mo-7.4Si-8.5B alloys (compositions are in at.%). The heat treatment for both compositions consisted of exposing the test samples at 1600 °C/24 h and 1700 °C/48 h in inert atmosphere. Compressive creep was also carried out for the Mo-12Si-12B alloy. This alloy contained ~32% volume of Mo phase and the remainder a mixture of Mo₃Si and Mo₅SiB₂ phases. The bending fracture strength for the Mo-12Si-12B was found to be ~600 MPa at RT, ~670 MPa at 1000 °C and ~700 MPa from 1200 to 1400 °C. The material was brittle (zero ductility) up to 1200 °C; at and

above this temperature the load-deflection curves exhibited some nonlinearity with very small deflections beyond the elastic limit. SEM observations of the fracture surfaces showed mixed cleavage and intergranular fracture at room temperature, with Mo phase exhibiting mostly a cleavage mode. At 1400 °C, the fracture modes consisted of brittle cleavage/intergranular propagation through the intermetallic Mo_3Si and Mo_5SiB_2 phases and significant plastic stretching of the Mo phase. The single-edge notch bending toughness (K_Q) for the Mo-12Si-12B was determined to be $\sim 15 \text{ MPa}\sqrt{\text{m}}$ at room temperature and between 10.5 to 14 $\text{MPa}\sqrt{\text{m}}$ from 800 to 1400 °C. For the Mo-7.4Si-8.5B composition (containing ~ 55 vol% Mo phase), the room temperature bending fracture strength was $\sim 450 \text{ MPa}$, which gradually increased to $\sim 700 \text{ MPa}$ at 1200 °C. Below 1200 °C, there was no ductility (absence of nonlinearity in the load-deflection curves), at 1200, and at 1400 °C some, ductility was observed with elastic-limit stress values of 405 MPa and 240 MPa, respectively. For this composition, the K_Q values were determined to be $\sim 10 \text{ MPa}\sqrt{\text{m}}$ at room temperature and 16 $\text{MPa}\sqrt{\text{m}}$ at 1200 °C.

Instrumented compressive creep was carried out on Mo-12Si-12B at 1200 and 1300 °C in inert atmosphere. At 1200 °C, the minimum creep rates were determined to range from 10^{-9} to $4 \times 10^{-9} \text{ s}^{-1}$ at stress values ranging from 100 to 180 MPa. At 1300 °C, for the same stress range, the minimum rates ranged from 8×10^{-9} to $7 \times 10^{-8} \text{ s}^{-1}$. This creep performance was compared with other prospective high-temperature structural materials, including Nb_5Si_3 , Nb + Nb_5Si_3 , $\text{Mo}_5(\text{Si}, \text{B})_3$, MoSi_2 + SiC (whiskers), TZM, Rene N6 and MoSi_2 . The creep resistance of the Mo-12Si-12B was significantly superior to that for all of these materials except Nb_5Si_3 .

2.2 TiAl ALLOYS: DEVELOPMENT, PROCESSING, AND EVALUATION

2.2.1 Introduction of Research Programs

The gamma research activities that have been performed during the last 5 years are divided into three major areas, that is, optimization of K5 alloys, evaluation of IHPTET gamma rotor/disk alloys, and development of very high-temperature gamma alloys. The optimization effort on K5 series alloys has been made through chemistry modification, controlling refined microstructures for improved balance in tensile and fatigue behavior, and by introducing strengthening particles (carbides and silicides) for greater creep resistance. Effort was made to evaluate rollability and rolled sheet of K5 alloys. Progress was made in the development of a new class of gamma alloys for very high-temperature applications: Alloy compositions were formulated to contain increased amounts of Nb and other elements. While some success was achieved in enhancing the oxidation resistance, further improvements in both oxidation and creep resistance is required in this ongoing program. For the last 2 years, an accelerated effort was undertaken toward evaluating IHPTET rotor/disk alloy 395M extrusions and forgings. Improved understanding of ingot metallurgy resulted from this work, and this led us to identify a better alloy chemistry and improved melting conditions and parameters. Investigations were made to evaluate the oxidation resistances of all gamma alloys, including existing gamma alloys. Collaboration work in some specific areas has been pursued with academia and industry, and some of them are summarized also in this report.

2.2.2 K5 Alloys: Design and Evaluation

This program was to design K5 alloys in wrought-processed forms with improved creep resistance and balance in other properties. The ultimate goal is to define K5 alloy compositions and processing routes that can yield optimized combinations of grain size/morphology, lamellar spacing and grain boundary morphology. A series of K5 alloys was formulated on the basis of by basic understanding in the areas of microstructure evolution through exploration of controlled processes and/or heat treatments; composition-structure-property relationships; and the individual and synergistic effects of alloying/microalloying additions on grain refining, mechanical behavior, and environmental resistance. This alloy system in wrought-processed microstructural forms has demonstrated significantly improved resistance to deformation/fracture at all temperatures, as well as high-temperature oxidation over the current alloys. Introducing and distributing small amounts of fine, stable precipitates (carbides and silicides) was found to result in improved high-temperature capabilities, such as in creep resistance fatigue-damage, and sustained-load-crack-propagation.

2.2.2.1 Alloy Chemistry Modification

On the basis of the fundamental/practical understanding made in the individual and synergistic effects of alloying additions, the alloy K5 (Ti-46.5Al-2Cr-3Nb-0.2W) was first formulated as the base composition; it exhibited good microstructural controllability, reasonable strength levels in standard wrought microstructural forms, and excellent oxidation resistance. A number of alloys were empirically formulated according to preliminary property evaluation and accumulated knowledge of alloying effects. Selected alloys have been extensively characterized for microstructure control and process development, and they are listed in Table 2. Collectively, this effort is leading us to the introduction of a new-generation (wrought) K5-series alloy system, K5-(46.0-46.5)Al-2Cr-3Nb-(0-0.2)B-(0.03-0.25)C-(0-0.2)Si.

Table 2. K5-Series Alloy Compositions (at.%)

Alloy	Ti	Al	Cr	Nb	W	B	C	Si	O	Others
K5	Bal	46.5	2.0	3.0	0.2		0.03		0.17	
K5R	Bal	46.5	2.0	3.0	0.2		0.03		0.17	
K5-Hf	Bal	46.0	2.0	2.5	0.2		0.15		0.19	1 Hf
K5S	Bal	46.5	2.0	3.0	0.2		0.03	0.2	0.18	
K5CS	Bal	46.5	2.0	3.0	0.2		0.1	0.2	0.18	
K5BC1	Bal	46.4	2.0	3.0	0.2	0.16	0.12		0.17	
K5BC2	Bal	45.8	2.0	2.8	0.2	0.2	0.16		0.19	
K5BCS	Bal	46.4	2.0	2.6	0.2	0.1	0.22	0.15	0.18	
KDBCS	Bal	46.5	2.0	2.8	0.24	0.1	0.22	0.15	0.17	

Table 2 Note: All alloy ingots weighing 25 kg were produced using the ISM technique, except for the KD 350 kg, which was produced by the (Plasma Arc Melting) PAM process. For ISM ingots, tungsten was added in the melt as elemental particle forms with two different sizes. Approximately 1- μ m particles were used for all alloys other than for K5-R where coarser (~10 μ m) tungsten particles were applied.

2.2.2.2 Microstructure Control and Process Development

Two distinct methods to control desired microstructures (especially fully lamellar (FL)) were developed and designed for wrought-processed K5 alloys. These include thermomechanical treatments (TMT) for refined lamellar material, and thermomechanical processing (TMP) for producing in situ lamellar material.

2.2.2.2.1 Control by TMT Methods

FL grain sizes (GS) produced in wrought material of the base alloy K5 (Table 2) were generally greater than 400 μ m and as large as over 1000 μ m, depending on annealing temperature and time. Two approaches were developed to refine FL grains, that is, annealing in a two-phase field and introduction of boron in the boride forms. The two-phase annealing consisted of forging or extrusion of alloy ingots and annealing of the material at a near-alpha temperature in either an alpha + gamma field or a alpha + beta field. This annealing resulted in refined alpha grains. Addition of coarse (instead of fine) W particles (alloy K5R) or a Hf addition (alloy K5-Hf) resulted in widening the alpha + beta field, allowing the lamellar GS to be controlled in the range of 500 to 100 μ m, depending on the alpha/beta volume ratio present. Adding small amounts of boron in the alloys was found to be more effective and convenient in refining lamellar grains, and accordingly most of K5 alloys (Table 1) were formulated to contain boron. Standard conditions to produce these wrought TMT lamellar materials were established from the experiments, as follows:

- Annealing of wrought material for 10 min to 4 h at T in the alpha or alpha + beta field
- Furnace cooling (>5 °C/min) or air cooling (AC) to a quench temperature
- Quench temperatures are set in the range of 1250 °C to 900 °C
- AC to Room Temperature (RT) from the quench temperature.

All heat treatments involved in the TMT process were conducted on bare material in air, and under all heat-treatment conditions, the oxygen-affected surface layer (including oxide scale) was shallow and did not exceed 300 μ m after 4 h annealing.

2.2.2.2.2 Control by TMP Methods

Thermomechanically processed lamellar (TMPL) microstructures were produced when a canned workpiece is hot worked, while it is in the alpha phase, in warm or cold dies. Three different TMPL methods identified are alpha extrusion, alpha forging, and alpha rolling. When controlled properly, the

lamellar microstructures unique to each method are formed during cooling in the deformed alpha matrix after hot deformation is ceased. The microstructural features, such as colony size, lamellar spacing, and texture, were found to be controlled by the deformation and stress-state, recrystallization and grain-growth kinetics, grain size, and cooling rate in the deforming and/or deformed alpha phase. Some of these factors appeared to be processing-specific, and thus are fixed. Alpha extrusion of either as cast-ingot or hot-worked material resulted in *situ* lamellar microstructures with various colony sizes (50 to 400 μm) having nonconventional morphology appearances which depended on pre-extrusion soaking temperature and extrusion ratio. The formation process and growth kinetics of the alpha-extruded lamellar structure and its texturing has not been investigated in detail. Boron additions tended to reduce the anisotropy. The alpha forging (AF) process consists of forging a canned work piece during cooling but while in the alpha state. Alpha forging textures the alpha grains radially or in the material's flow directions. Forging operation should end before the lamellar formation begins, and uniquely defined lamellar structures form in the unstressed matrix during the subsequent cooling period. Regardless of their morphologies and sizes, the alpha-forged microstructure was found to exhibit a [110] fiber texture with respect to the forging plane. Remarkable tensile strength and widely ranging tensile ductility were obtained through this process. Conditions and parameters for producing these FL microstructures were quantified by combining microstructural observations, and modeling the process relating transfer time, die temperature, ram speed, and cooling rates in specific locations in the billets. Alpha rolling to produce another *situ* lamellar material was experimented in collaboration with Plansee by pack-rolling canned work pieces successively after presoaking at a temperature near the alpha transus. The first trial was not entirely successful in producing FL material; however, it demonstrated the possibility to produce fine FL microstructures (much smaller than the alloy sheet thickness) by properly selecting the soaking temperatures and rolling conditions/parameters.

2.2.2.2.3 Stabilization Treatments

To achieve thermally stable sound material conditions at usage temperatures, aging treatments at low temperatures were given on all samples treated or processed at the high temperatures described. For anticipated use at 760 °C, the aging temperature was empirically determined to be 900 °C, and holding for 50 h resulted in the best creep resistance. This aging broke up the alpha plates into elliptical-shaped particles, while generating carbides and silicides in between, as described later. Prolonged aging at this temperature coarsened these particles reducing the creep resistance. Depending on use temperature and property requirements, it may be important to establish the optimum aging conditions, and thus detailed experiments in this are required.

2.2.2.2.4 Multistep Forming Experience

An industrial size ingot of alloy KD, weighing 336 kg, was produced using the single-melting PAM technique at Pratt & Whitney (P&W). The ingot was machined to a 76-cm long billet with 33-cm diameter, which was then wrapped with ceramic felt and canned in a 45-cm-diameter stainless steel can. The canned billet was homogenized at 1320 °C for 6 h, and then extruded to a cylindrical rod form at a 6:1 extrusion ratio. The extrusion rod was machined to 20-cm-long billets that were isothermally forged to 7-cm-thick plates (65 percent reduction). Some of the billets were isothermally

forged at 1159 °C to 2.5-cm-thick plates (88 percent total reduction) by the two-step process. These forgings were given alpha treatments to produce standard TMT lamellar microstructures. The grain sizes in these lamellar materials (LM) were measured to range widely between 300 and over 700 μm . The low boron content (0.1 at.%, Table 1) and nonuniform distribution of borides were responsible for this. For the same boron content, the grain sizes were qualitatively estimated to be coarser than those generated in ISM ingots that were wrought processed. Two 7-cm-thick plates were canned, annealed at 1310 °C, the maximum temperature of the furnace at the Wyman-Gordon Houston forging facility, and forged to 2-cm-thick plates in dies to 700 °C, followed by off-press cooling to RT. The alpha transus of alloy KD is 1321 °C, so the resulting microstructure was not entirely FL. The originally planned alpha forging (AF) was not accomplished; nevertheless, the experiment demonstrated that the AF process could be scaled up.

2.2.2.3 Mechanical Properties

2.2.2.3.1 *Tensile Properties*

TMTL materials with a GS range of 100 to 400 μm show RT Yield Strength (YS) levels between 450 to 550 MPa and tensile elongation (high as 2.0 percent). Impressive improvements were observed in TMPL materials; for example, alpha-extruded LM showed YS levels reaching as high as 1000 MPa at RT and tensile elongation up to about 3 percent. Further increases in strength are expected to be possible by modifying the extrusion parameters and conditions through controlled postextrusion cooling rates, however, these responses have not been demonstrated for large-scale products. Significant property improvements in strength were achieved in AF LM produced in laboratory-scale disk forms; their tensile ductility reach as high as 3.5 percent and RT YS ranged from 620 to 950 MPa, depending upon the GS and composition, in both longitudinal as well as transverse directions. Overall, the fine-grained duplex material is more sensitive to strain rate than FL material in both strength and elongation variations. Their high-temperature strength retention in TMPL materials was remarkably high, with the YS ranging from 500 to 670 MPa at 870 °C and 320 to 600 MPa at 1000 °C. On the basis of the deformation anisotropy and tensile properties of LM measured for GS in the range of 200 to 3000 μm , and lamellar spacing (LS), λ , varying from 2 and 0.2 μm , the Hall-Petch (HP) relationship for FL material was proposed to be $\alpha_y = \alpha_0 + k \lambda d^{-1/2} + kd^{-1/2}$. In this relationship, the HP constant is expressed as $k = \alpha k_d$ with $\alpha = f(\lambda, \alpha_2/\gamma)$ where k_d is the usual GS-dependent HP constant, and α is the anisotropy factor, which is a function of LS and alpha-2 volume fraction. For large LS, k approaches that of the duplex material, and the maximum k value will be set by the maximum anisotropy, which is expected to occur at the finest LS for a given alpha-2 volume fraction.

2.2.2.3.2 Fracture Toughness

The fracture toughness at RT was tested on compact tension specimens for various K5 alloys in both duplex and FL forms. The typical initiation toughness (K_{Ic}) and saturation toughness (K_{max}) for these materials were 16 to 18 MPa and from 21 to 25 MPa for medium-to-coarse FL material, 10.2 MPa and 10.2 MPa for duplex material, and 14.0 MPa and 14.5 MPa for fine (<40 μm) FL material. These trends are consistent with the dependence of toughness on GS established in our previous contractual work.

2.2.2.3.3 Fatigue Resistance

Hourglass-type specimens of K5 specimens having TMTL microstructures were tested with $R=0.1$ at 760 °C and 870 °C in air to generate S-N curves and to determine the fatigue strength (FS) at 10^7 cycles. The results were analyzed in comparison with those tested earlier at 600 °C and 800 °C to draw the following conclusions:

- (1) Fatigue damage in gamma alloys takes place through the typical processes: (1) a remarkable long plastic deformation process; (2) crack initiation to a critical size which is equal or greater than GS, depending on temperature; and (3) rapid crack propagation to failure.
- (2) At temperatures below Brittle Ductile Transition Temperature (BDTT), S-N curves are fairly flat. FS is largely controlled by tensile properties, meaning that fine-grained material is more fatigue resistant. At higher temperatures, fatigue life depends on tensile strength under high stresses, and under low stresses (<YS), creep sets in to reduce the fatigue life. In this case, fully lamellar material is more fatigue and creep resistant.
- (3) A tensile-creep-temperature deformation map was constructed in the S-N field. Cleavage fracturing takes places below BDTT, and boundary fracturing is predominant at higher temperatures.
- (4) Fully lamellar microstructures with intermediate-size grains and an appropriate distribution of incoherent carbides yield improved balance in fatigue and HT creep resistance.

2.2.2.3.4 Fatigue Cracking Threshold

The fatigue crack propagation tests conducted on K5 alloys in collaboration with the AFRL/MLLM mechanical behavior group showed that the threshold values (ΔK_{th}) range from about 5 MPa $\sqrt{\text{m}}$ for duplex material to 7.5 to 9 MPa $\sqrt{\text{m}}$ for FL materials. Statistical analysis showed that ΔK_{th} values appear to be proportionally related to the initiation toughness (K_{Ic}) values for a given material, which can be described as $\Delta K_{th} = \alpha(K_{Ic})$, where the constant α appears to be material-specific and is ~ 0.5 for TiAl alloys. For FL material, this relation can be generalized as $\Delta K_{th} = \alpha/(d, \lambda)$ by reasonably assuming that the threshold in FL material is a function of GS (d) and lamellar spacing (λ). The characteristic, rapid increases in fatigue-crack-growth (FCG) rate were also observed, with increasing stress intensity or crack length. Nevertheless, the FCG rates in FL materials are considerably lower than those of duplex materials at RT and high temperatures.

2.2.2.3.5 Creep Resistance

Tensile creep testing was conducted under constant loading conditions on both duplex and FL materials of most of alloys (listed in Table 1) in air over the temperature range of 760 °C to 870 °C. Both constant loading and stress-increase tests were applied.

Both materials produced under various cooling rates were given aging treatments at temperatures 800 °C and mostly 900 °C for varying times up to 100 h. Under all testing conditions, both primary creep and secondary creep occurred faster for FL than for DP materials at all temperatures and the difference became greater as temperature was raised.

Primary-creep strains in K5 alloys, as observed in conventional gamma alloys, were measured to be large, ranging from 0.2 to over 1 percent depending on microstructure and creep condition. Alloy modification for solid solution hardening (e.g., by W or Nb) has not demonstrated any significant improvement in primary creep resistance. When aged properly, FL K5 alloys containing Si and/or C showed remarkable improvements in creep resistance. The improvements were greater for primary creep than secondary creep and under higher stresses. The enhancement was found to be due to carbides and/or silicides that precipitated out in stringer forms at the expense of alpha-2 plates. The greatest improvement was observed in K5SC FL material having large grains (~450 µm) aged at 900 °C for 50 h and tested at 760 °C under high stresses (276 MPa). K5 alloys containing B and C had were slightly less creep resistant than FL K5SC. Relatively finer grains (~200 µm) and coarser LS due to the presence of borides appear to be responsible for this. The effect of carbides and silicides is reduced as the testing temperature increases, and preliminary analyses showed that more stable dispersoids are needed for long-term exposures at or above 850 °C.

2.2.2.3.6 Creep Crack Growth (CCG)

The crack growth behavior of K5S under constant loading conditions was investigated at 650 and 800 °C in a nearly fully lamellar microstructural form. Cracking ensued at stress intensities (K) higher than respective fracture initiation toughness. At 650 °C, creep crack extension occurs mainly through transgranular fracture; however, this growth process was exhausted eventually. At 800 °C, crack extension involved extensive plastic deformation, and consisted of an initial rapid transition period and a subsequent steady state. The resistance to crack propagation at 650 °C is explained in terms of work-hardening and the increased crack propagation at 800 °C in terms of boundary weakening and creep damage in the plastic zone. The cracking modes at 800 °C were boundary fractures consisting of interlamellar separation and intergranular fracture, the latter of which took place through the formation and coalescence of voids.

2.2.3 Microalloying and GS Effect of Creep Behavior

Creep resistance of FL K5 alloys containing C and/or C+S in both primary and secondary creep was found to be a strong function of aging at 900 °C. Upon aging, both incoherent Ti₂AlC carbides and hexagonal silicides were found to form from the dissolving alpha-2 plates, resulting arrays of carbides,

silicides, alpha-2 and beta particles. The strategic distribution of the particles effectively pinning mobile dislocations along the easy slip directions effectively slows down creep deformation. The best resistance was measured on the material aged for 50 h, and remarkable improvements in both the secondary creep and primary creep resistances were observed at 760 °C and 800 °C. The minimum creep rate at 800 °C was reduced by five to seven-fold, and the primary creep strain at 760 °C/276 MPa was 0.2 percent which is compared with that (1 percent) for the base K5 alloy. The improvement of primary creep resistance became more significant under higher applied stresses, but this apparent significance has not been quantified.

However, instantaneous strain, or initial loading strain, was not clearly affected by the presence of precipitates. On the basis of balanced property consideration, the allowable upper limit for temperature may depend on Al content, but was suggested to be 0.2 at% C for Ti-47Al base alloys and higher levels (up to 0.3 °C) for lower Al-containing alloys. A creep study was made on a fixed alloy (similar to the base K5) with carefully controlled FL GSs (105 to 600 μ m), and the study indicates that within the range investigated, the GS effect is insignificant at 760 °C, but that large FL GS yields higher creep resistance at temperatures higher than 870 °C. The combined effects of GS and LS have not been clarified yet. These results indicate that the creep behavior measured below 870 °C depends on largely microstructural features other than GS, including dispersion and LS.

2.2.4 Effect of Boron on Grain Refinement and Lamellar Formation

As was described earlier, lamellar grain refinement in wrought-processed K5 alloys was achieved through the two-phase annealing, alpha processing, or TMP, and boron addition followed by TMT. The most efficient way was found to be adding small amounts of boron. The boron method was further investigated to confirm if the method could be applicable for any compositions, and then to quantify and understand the process in detail. Studies were also made to see if borides influence the lamellar formation process, including the kinetics. For this, experiments were conducted on both binary alloys and K5 alloys having the compositions of Ti-(43-48)Al-(0-0.5)B (at.%) and K5-(0.1-0.3)B. Alloy ingots were forged to about 88 percent reductions and then given annealing in the alpha phase field followed by cooling at various cooling rates and schemes. It was found that boron additions greater than 0.03at% produced Ti-borides interdendritic regions (often in ribbon forms and mixed with beta phases). Forging broke up these borides to form stringer arrangements parallel to the materials flow direction, which effectively retard the high-temperature alpha grain growth. The greater the boron content, the finer the boride stringer spacing became, resulting in finer alpha grains. For the given forging reduction, the resulting lamellar GSs for each alloy set are quantitatively related to the boron content, which in turn controls the boride array spacing. Cooling experiments, including Differential Thermal Analysis (DTA) showed that borides on grain boundaries help the gamma phase nucleate to raise the lamellar formation temperatures. This led to the formation of lath structures that were coarser and more inhomogeneous than in alloys containing no boron, which in turn lowers the strength (both tensile and creep) levels. This deficiency was alleviated by employing a faster cooling rate and/or modifying chemistry, such as reducing Al content and microalloying with carbon or oxygen. Using the cooling data and metallographic observations, a CCT/Time Temperature Transformation (TTT) diagram was constructed to describe microstructure evolution in Ti-44Al and Ti-44Al-0.2B.

2.2.5 Production and Evaluation of K5 Alloy Sheet

This program was aimed at producing and characterizing rolled sheets of K5BC1 and K5BC2 alloys (Table 1). Two billets for each alloy were isothermally forged to form 1.2-cm-thick plates, and they were pack-rolled at Plansee by duplex rolling and alpha-rolling processes to sheets having the dimensions of 180 x 450 x 1.0 mm³. They were stress relieved by annealing at 1000 °C for 2 h. The K5 alloy plates were rolled as easily as those of simpler alloys (Ti-48Al-2Cr, for example) and the resulting microstructures were compared and found to be finer and more uniform than the ternary alloy sheets. The process produced duplex microstructures as well as an alpha-rolled lamellar (ARL) microstructure which were fairly uniform and fine grained, with average GSs of 10 µm and 30 µm, respectively. Remarkable tensile property levels, as compared with other gamma alloys, were measured especially for alloy K5BC2: YS=864 MPa, UTS=980 MPa and fracture-strain=1.4% at RT; YS=533MPa and UTS= 662 MPa at 870°C. Similar properties were measured at Plansee and Boeing. Fatigue tests on smooth, uniform gage sheet specimens showed typical SN curves reflecting uniform microstructures and the fatigue strength FS of 510 MPa at 10⁷ cycles. Tensile-creep testing conducted on the duplex material over the temperature range from 700 to 840 °C showed that the creep resistance is greater than that of the duplex material of the base K5 alloy in Table 1.

2.2.6 Evaluation of IHPTET Rotor/Disk Alloys

This task was to evaluate 395 M alloys developed for IHPTET compressor disk applications. P&W produced two PAM alloy ingots having a 17-inch diameter (called TR14) and a 26-inch diameter (TR15) at Allvac; these ingots were subsequently extruded and forged. Fogged plates were heat treated for fully lamellar microstructures. The chemical analysis showed that the composition is Ti-46.2Al-2Cr-2Nb-0.5M-0.12B-0.3C-0.3O (at%). The carbon and oxygen contents were greater than the nominal.

2.2.6.1 Characterization of Alloy 395 M

2.2.6.1.1 Evaluation of Alloy 395 M

The objective of this added task was to conduct an accelerated characterization of multistep formed 395 M forgings with reductions comparable to those of PRDA V rotor. A billet from TR14 extrusion was forged into two plates with different forging reductions, 78 percent and 88 percent. FL microstructures were produced by appropriate annealing treatments, followed by relatively slow cooling (10 to 50 °C/min). From the property characterization, the following conclusions were drawn: 1) Lamellar GS in 395M ranges from 100 to over 400 µm. The nonuniformity increases with decreasing forging reduction; 2) the lamellar material exhibits reasonably high tensile strength, creep resistance and FCG resistance; 3) the lamaller material also shows unacceptably low tensile ductility (0.3 to 0.9 percent), and poor fatigue resistance, especially when forged to a low reduction; and 4) the oxidation resistance is poorer than that of 4822. It appears that the poor ductility stems from the coarse and nonuniform grain sizes and also high levels of interstitial contents (C and O). It will be important to

isolate each effect in order to find out ways of improving ductility. A separate investigation conducted in collaboration with Yokohama Univ. showed that the oxidation resistance is lower than that of Ti-48Al-2Cr-2Nb. Defect analyses were conducted on some selected forging in fully lamellar conditions using X-ray radiography, probe analysis and metallography. Two typical defects were low-density areas (LDA) consisting of fine gamma grains and high-density areas (HDA) consisting of fine, Ti-rich lamellar grains with GB beta phases. Porosity was present only along the central areas that correspond to the ingot central line. These defects are apparently related to chemistry variations with location, which do not appear to be related to the solidification pathway, especially for HDAs. Homogenization experiments indicate that removal of such defects is extremely difficult, requiring extreme conditions ($T > 1350$ °C; $t > 5$ days), which are not only impractical but also alter the desirable matrix microstructures.

2.2.6.2 Evaluation of Alloy 395MM

According to the characterization results described in the previous section, and also results from TR15 ingots and forgings, two recommendations were made and successfully adopted by AF as well as P&W. A modified alloy, named 395MM, was introduced, with the following composition: Ti-46.2Al-1.2Cr-2.2Nb-0.3Mo-0.20B (all in at%) - 800 C (wtppm)-900 Ox (wtppm)

A PAM ingot (26 inches in diameter and 3000 pounds) was produced in October 2000 using finer master alloy particles at a slower feed rate (300 lb./h versus 600lb/h). Tighter control of interstitial was measured. Three, 3-inch thick, 26-inch-diameter disks were cut from the ingot, one from the top and two from the bottom. We received one 2/5 pie from each disk for characterization. Extensive radiography and metallographic examination was conducted for 3 months to find no defects in the portions of the ingot. Careful extensive microprobe composition analyses were also performed to find relatively uniform distribution of composition with no noticeable segregations. Homogenization treatments were carried out at 1370 °C for 8 h and both metallographic and Back Scattered Electron Imaging (BSEI) observations and microprobe analysis indicate that homogenizing this alloy ingot is possible. Small billets were prepared for the pies and extruded for characterization of hot-worked material. Characterization efforts are being made on this material as part of an ongoing program.

2.2.7 High-Temperature Gamma Alloy Development

This task was to design/develop gamma alloys for high-temperature applications (long-term exposure at 900 °C) by first enhancing oxidation resistance and then the creep resistance. Preliminary studies on 95G (Ti-45Al-10Nb), 97G (Ti-45Al-8Nb-0.04B) and 98G (Ti-45Al-8Nb-0.2B-0.15C), indicated that the first two alloys do not have a single alpha phase field up to 1400 °C. The yield strength varies between 500 and 1250 MPa depending on the HT temperature and cooling rate. The treatment at 1300 °C (in alpha + beta) followed by two-step cooling resulted in a nearly lamellar structure having 25- μ m lamellar grains decorated with GB beta phase plates. The yield strength was 1200 MPa. Two alloys, Ti-45Al-10Nb-(0, 2)Cr, were selected for this program. Detailed HT experiments showed that the Nb contents should be 8 percent or lower in order for FL material to be generated with confidence.

Extensive cyclic oxidation tests (at 760 °C and 870 °C for up to 1000 h) were carried out on these alloys, in collaboration with the Yokohama group, along with all existing gamma alloys including K5 alloys. The results showed that these two compositions are superior to all other gamma alloys at 760 °C up to 1000 h. At 870 °C, however, while these alloys maintain the same superiority over K5 alloys up to 300 to 400 h exposure, further exposure increases weight gains to the level of K5 alloys or higher, indicating that high-Nb additions may promote spalling. This means that development of high- Nb-containing alloys may not be justified for long-term application unless the rapid spalling tendency could be suppressed by certain means, such as microalloying. From these results, an alloy, called 98D, was designed as follows: 98D: Ti-45Al-2Cr-6Nb-x(W, Hf, Mo)-x(B, C).

Cyclic exposure tests showed that this alloy shows oxidation resistance far greater than any alloys existent to date. Apparently, the synergistic effects between Nb and refractory elements effectively reduce spalling as observed visually and microscopically. Two ongoing tasks include finding the best compositions for oxidation resistance and then identifying dispersoids that are thermally and thermomechanically stable at 900 °C or higher.

2.2.8 Summary of Other Efforts

2.2.8.1 Automotive Valve Program

The objective was to experiment to find whether preforms of gamma alloys can be forged into automobile exhaust valve forms in the production press. Using the TRW forging press, forging experiments were conducted to establish the relation between the can/insulation thickness and the sound-stem length, and to identify the influences of thermal-barrier/lubrication glass coating. It was found that thicker can/insulation resulted in more sound valve extrusion, and that the maximum sound-stem length was about 7 cm. The glass coating played an important role as lubricant rather than as thermal barrier. It would be extremely difficult to produce sound full-length stem valves using the current TRW production facility. This means that producing valves from uncanned preforms is impossible. This experience could have led this program in another direction, that is, exploration of possibilities to produce short-stem valves from uncanned extruded rods or cast rods under more forgiving conditions. However, the effort ended due to the decreased interest from the industry at that time.

2.2.8.2 Control of Casting Microstructures

This project was aimed at exploring the methods to refine coarser/nonuniform cast microstructures through heat treatment. The ultimate goal was to develop economical methods to produce the desired microstructures. Some experiments conducted on alloy castings with thin sections showed that converting cast structures into refined lamellar-base microstructures was possible by heat treatments; however, it was practically impossible to remove the nonuniformity of the starting microstructures.

2.2.8.3 Collaborations

Collaboration with other institutes/groups has been actively pursued in various areas: (1) Anger Electron Microscopy (AEM) analysis of the interactions between dislocations and carbide particles was performed through the collaboration with Prof. M. Mills, The Ohio State University (OSU). This work positively identified the carbides and silicides pin dislocations moving in the easy directions; (2) oxidation resistance of K5 alloys and high-temperature gamma alloys have been investigated, along with other existing gamma alloys, in collaboration with Dr. Y. Yoshihara of Yokohama University who conducted exposure experiments for number of gamma alloys. Through this work, gamma alloys could be classified in terms of cyclic oxidation resistance; (3) castability of K5-1.0at% B alloy has been investigated in collaboration with IHI, Japan where. The results by IHI indicate that molds for casting thin section plates (<3 mm) are difficult to be completely filled; (4) impact/fatigue evaluation of FL K5 was investigated in cooperation with NASA-GRC; (5) the phase relationships in Ti-45Al-(8-10)Nb alloys were investigated with Prof. G. Chen of UST Beijing.

2.3 TiAl: FUNDAMENTAL STUDIES

2.3.1 Phase Field Model for the Formation of the Lamellar Structure in Ti-Al [3]

A three-dimensional phase field model of the $\alpha \rightarrow \alpha_2 + \gamma$ transformation has been developed to simulate the formation of coherent multidomain lamellar structures in γ Ti-Al intermetallic alloys. The model takes into account the effect of coherency strain associated with the lattice rearrangements accompanying the phase transformation and the anisotropy in interfacial energy. Simulation studies based on the model have successfully reproduced the essential features associated with the multidomain lamellar structures observed experimentally. It is shown that the coherency strain accommodation is the dominating factor responsible for the lamellar structure. The neighboring lamellae of γ phase are found to have either a twin or a pseudo-twin relationship, with the former being most common. It is found that strain-induced, correlated nucleation plays an important role in the formation of the twinned lamellae. The lamellar thickness is determined by the interplay among the elastic strain energy, interfacial energy and bulk chemical free energy. Domains within individual lamellae are isotropic, and domain boundaries are smoothly curved. No special self-accommodating morphological patterns are observed on the (0001) plane.

2.3.2 The Properties of the Unit <110>/2 Dislocation in Ti-Al [4-5]

By a careful analysis of electron micrographs of deformed specimens of single-phase γ Ti-Al, we have proved that the pins that were observed to obstruct screw dislocations are in fact jogs, probably caused by double-cross slip events. The jogs vary in height from a single plane spacing up to about 50 nm. The very small jogs can move with the dislocation, producing or absorbing vacancies, but the higher jogs are sessile. The low jogs contribute to the friction stress (since their effect is reversible), but the higher jogs exert a spectrum of point forces on the moving dislocation, acting against the direction of motion.

Calculations of the forces, in conjunction with experimentally observed separations of the pins, demonstrate that the observed yield stress can be accounted for by the sum of the friction stress and the pinning stress. In principle, the yield stress anomaly can be caused by the temperature dependence of the frequency and height of jogs. Creep in Ti-Al may also be rate limited by the emission or absorption of vacancies at jogs in gliding screw dislocations.

The picture which emerges is not compatible with the Viguier-Louchet theory which considers single-cross slip events and which takes no account of the strength of the pins.

2.3.3 The Yield Stress of Lamellar Ti-Al [5-8]

The theory for the yield strength of fully lamellar Ti-Al alloys has identified the fact that out of all the possible microstructural parameters, the most critical one is the thickness of the lamellae within a grain. The strengthening mechanism is then a Hall-Petch mechanism for dislocations crossing the lamellar boundaries. In this case, it is necessary to reconcile the experimental measurements of Hall-Petch slopes in gamma Ti-Al, which may be summarized as follows:

Grain strengthening in monolithic gamma (McQuay)	1.0 MPa \sqrt{m}
Grain strengthening in FL Ti-Al (Kim)	2.0 MPa \sqrt{m}
Hard and soft modes in PST in shear (Kishida)	0.1 MPa \sqrt{m}
Lamellar strengthening in high strength FL Ti-Al (Dimiduk)	0.1 MPa \sqrt{m}

Assuming that monolithic gamma grain boundaries act similarly to FL grain boundaries, the grain strengthening in FL Ti-Al must have two equal components, one (1.0 MPa \sqrt{m}) from ordinary grain boundary obstacle hardening and the second an apparent effect caused by the fact that grain size and lamellar thickness are correlated.

The lamellar hardening in PST gives a Hall-Petch slope of 0.1 MPa \sqrt{m} in shear, which would be expected to give about 0.3 MPa \sqrt{m} for FL Ti-Al in compression. There are three reasons why the measured values are lower (0.1 MPa \sqrt{m}). First, the Parthasarathy Effect, that pinports that in a distribution of lamellar thicknesses, the effective thickness is about twice the average thickness. Second, the Hall-Petch slope drops when lamellar thickness decreases as the Hall-Petch strengthening saturates. Third, the predominantly gamma/gamma boundaries in Poly Synthetically Twinned (PST) are stronger than the predominantly alpha/gamma boundaries in FL Ti-Al. The three reasons are each of similar importance.

2.3.4 Creep of FL TiAl Alloys - Review and Identification of Critical Variables

There is a need to improve the creep resistance of fully lamellar TiAl alloys; however, there is also a lack of understanding of what specific chemical and microstructural factors influence the creep deformation of these materials. Processing complexities have precluded any systematic studies. However, a review of literature data was conducted to identify critical effects from existing data through sorting and critical analysis. The creep data on FL alloys were analyzed along with data on the

constituent phases, Ti-rich γ and Al-rich α_2 with a view to determining the relative effects of chemistry and microstructural parameters (grain size, lamellar spacing (γ thickness), volume fraction α_2) in FL gamma alloys. The minimum creep rates measured at temperatures below ~ 850 °C (above which the microstructure is unstable under creep conditions). For the single-phase (NG) alloys were collected. This was limited to only the Ti-rich end of the alloys, viz., the Ti-50Al composition, since this is very close to the γ phase in the two phase alloys. The Al-rich composition of α_2 for which data is available is the 34mol%Al. Despite the lack of systematic studies on FL polycrystalline alloys, existing data could be analyzed for identifying critical effects on the creep of these alloys. The grain size, α_2 volume fraction, and contents of Al, Cr, Nb, and Mn appear to have insignificant effects on creep and B additions are detrimental. Of the various factors that might enhance the creep resistance of these alloys, ternary additions of Si, W and C, and the refinement of lamellar spacing appear to be the most significant. Dispersion strengthening as a strengthening mechanism appears to be at least as effective as refinement of lamellar spacing. Si and C additions are more promising than are W additions in the range studied. Significant refinements in lamellar spacing and optimization of dispersion/precipitation hardening systems, especially C and Si containing alloys are likely to yield the most creep-resistant alloys. Finally, the effects of interstitial elements needs to be studied [9].

2.3.5 Lamellar Spacing Effect in Creep of Polycrystal FL TiAl Alloys

The fully lamellar (FL) microstructure is known to have the best creep resistance, but the effects of microstructural variables remain poorly understood. A recent review [9] considered the available data on FL alloys in an attempt to determine trends of the effect of the microstructural variables. The lamellar spacing was suggested to have a significant effect; however the effects were found to be confounded by more than one variable being changed at a time. Due to the complex interactions between the various processing variables, controlling the microstructure and thus conducting a systematic study has been difficult. There is no reported study in which just one of the variables has been independently varied in order to study the effect of a chosen variable. In the present work, we report on a set of processing schedules that yielded two FL alloys (Ti-47at%Al) which had essentially the same microstructure except for the lamellar spacing. The effect of LS on the secondary creep rate and on the primary creep strain were measured at 760 °C and 207 MPa. Both primary creep strain and steady-state creep rate are markedly reduced by reducing the LS. The dependence of primary creep strain can be rationalized through a classic dislocation pile-up model. The square-root dependence of the secondary creep rate on LS suggests that conventional power law creep models and substructure-invariant creep models are inapplicable to FL alloys [10].

2.3.6 Creep Anisotropy of PST and Its Relation to Creep of Polycrystal FL

The anisotropy in creep behavior of a PST crystal was examined using crystals of the composition Ti-48Al in three different orientations, $\phi=0^\circ$, 45° and 90° , in the temperature range of 700 ° to 815 °C. In addition, a fully lamellar Ti-48Al polycrystal of similar lamellar spacing was also tested under identical conditions for comparison. Significant anisotropy was observed at all the three temperatures of test. In both primary and secondary stage, the 0° PST material was consistently the strongest and the 45° the weakest, with the polycrystal behaving much like the 45° PST crystals. The anisotropy could not be

rationalized based on either Schmid factor differences or α_2 anisotropy. The beneficial effects of orientation are observed to be similar to those of alloying additions of C or Si. It is anticipated that fully-lamellar textured polycrystals will be significantly superior to polycrystalline materials having a random grain orientation in both primary and secondary stage creep behavior [11].

2.3.7 Microstrain Stress-Strain Behavior of PST and FL TiAl Alloys

The flow behavior of PST crystals of a Ti-48Al alloy was studied as a function of orientation in the microstrain regime (10^{-5} to 2×10^{-2}) at room temperature, to understand the evolution of the anisotropy of flow stress with strain. After resolving the stresses on to the slip systems, the variation of flow stress with orientation was observed to be only 10-15 MPa at near zero (10^{-5}) strain, but it increases rapidly to ~ 70 MPa at 0.2 percent plastic strain. The stress-strain response had discrete steps, indicating the possible effects of the progressive deformation of lamellae of varying thicknesses within the distribution. The flow behavior of a polycrystalline fully-lamellar (FL) alloy of the same composition was also studied in the same strain regime for comparison. The saturation engineering flow stress (0.2 percent) and the strain-rate sensitivity of the polycrystal were found to be close to those of the 0° orientation of the PST crystals. Combining the data of the hard orientations of the PST material and those of the polycrystal, an apparent Taylor factor for FL polycrystalline Ti-48Al was determined to be in the range of 3.2 to 3.8. The results on PST crystals were analyzed and rationalized using a mechanistic model that takes into account the distribution of the lamellar sizes (γ/γ and γ/α_2). The work-hardening rate, the saturation flow stress of the hard orientations, and the Hall-Petch slopes are all predicted to be sensitive to both the mean and the standard deviation of the lamellar thickness distribution, with dislocation sources from only a fraction of the distribution contributing to the deformation process, even at 0.2 percent plastic strain. Narrower distributions of LS are predicted to be beneficial in increasing 0.2 percent yield strength [12].

2.4 MULTILAYERS AND NANOCRYSTALLINE MATERIALS

2.4.1 The Strongest Size for Nanocrystalline Copper [13]

Nanocrystalline materials generally show a peak in their yield strength at a grain size of approximately 20 nm. At larger grain sizes, the drop in strength may be attributed to the Hall-Petch effect, whereby dislocation pileups of ever increasing length generate larger and larger stress concentrations at their heads. These stress concentrations enable the leading dislocations to cross grain boundaries at lower and lower applied stresses as the grain size increases. On the small grain size side of the peak, it is plausible that diffusive creep mechanisms operate more and more efficiently as the grain size shrinks. This hypothesis has been tested in a model containing Hall-Petch strengthening of large grains, Coble creep in small grains and a log-normal distribution of grain sizes. The model agrees well with experimental measurements in Cu and other materials.

2.4.2 Dislocation Nucleation as an Alternative to Multiplication [14]

When a metal or an intermetallic is gradually loaded, plasticity may start either by preexisting dislocations multiplying or by the nucleation and expansion of new dislocation loops. Nucleation had been discounted because the stress required to create a loop is too large, but a new model by Khantha, in which loops are created collectively at lower stresses, has reopened the possibility that nucleation might compete with multiplication in some materials, e.g., nanocrystalline materials in which Frank-Read sources are short. It is also possible to have a hybrid model in which nucleation of loops close to existing dislocations effect mobilize those dislocations. An analytical model which is simpler than Khantha's has been formulated and supplemented with a computer simulation of self-catalytic dislocation nucleation.

The computer model is a two-dimensional Monte Carlo simulation in which a plane is divided into N squares, each of which is a potential nucleation site. Sites are visited randomly, the stress at the evisited site from the applied stress and from all other existing dislocation loops is calculated, and a new loop is nucleated with a probability $\exp(-U/kT)$, where U is the formation energy of a loop in the presence of the local stress. It has been confirmed that the computer model, like the previous analytical model, does give critical values of applied stress and temperature at which nucleation becomes self-sustaining. The values of the critical parameters are lower in the computer model because the interactions between close loops are much larger (and more realistic) than the mean field interactions used in the analytical model. The reduced critical parameters make nucleation a more plausible process than had been thought previously.

2.4.3 Yield Strength of a Semicoherent Metallic Multilayer [4,15]

Multilayers derive their strength from the presence of many interfaces which block the progress of glissile dislocations. In order to calculate the macroscopic strength of such materials, the most accurate possible calculations must be made of the barrier strengths of interfaces in systems of interest, e.g., multilayered Cu-Ni. Previous estimates, based on the Koehler effect, the van der Merwe effect, the chemical effect and the crystallographic effects, are adequate when the layers are thick but they fall short when the layers are thin enough to show coherency and to have dimensions which are comparable to the dislocation core widths. Atomistic simulations can be used to calculate the strengths of interfaces between very thin layers. In Cu-Ni, the results of atomistic simulations of the barrier strength of interfaces can be summarized as follows:

- (1) The Koehler stress τ_K^* is confirmed to be 0.01μ to 0.015μ , positive at the Cu->Ni interface and negative at the Ni->Cu interface. In coherent Cu-Ni multilayers, the coherency stress enhances the modulus difference between Cu and Ni, and, hence, enhances τ_K^* . In addition, an opposite effect occurs in any multilayer; τ_K^* drops rapidly when the width of a dislocation is comparable with the layer width.
- (2) The lattice parameter mismatch stress is provided by the blocking action of van der Merwe dislocations in incoherent (long wavelength) multilayers and is of order 0.01μ , positive at all interfaces. In thinner multilayers, the stress falls (to zero at the coherence limit), but its effect remains strong at all

wavelengths because as the density of van der Merwe dislocations falls, the coherency stress rises. Coherency stresses exert glide forces on mobile dislocations, modify their cores, and change the elastic constants.

(3) The chemical stress itself τ_c^* is comparatively small in Cu-Ni, 0.003μ (positive at Cu->Ni, negative at Ni->Cu), but it is strongly affected by coherency Escaig stresses. At {001} interfaces, coherency reduces τ_c^* by 0.005μ by constricting Cu dislocations and expanding Ni dislocations. At {111} interfaces, exactly the opposite occurs, and τ_c^* is increased by 0.005μ .

(4) Interfaces at which the slip plane is discontinuous are powerful obstacles. 60° dislocations can penetrate twin interfaces only at stresses of 0.03μ to 0.04μ . Even screw dislocations are strongly blocked because they cross slip into the interface where the stacking fault energy is low.

(5) The total barrier strength of both {111} and {001} interfaces is $\sim 0.02 \mu$ at long wavelengths. As the wavelength is decreased, τ^* falls, gradually at {001} interfaces, but precipitously at {111} interfaces.

The barrier strengths, τ^* , calculated either atomistically or by normal methods (e.g., for the blocking effect of van der Merwe dislocations) may be added appropriate for a given interface and inserted into the discrete Hall-Petch equation to obtain a value of the strength of the multilayer. The result, for Cu-Ni, reaches a peak of about 2 GPa at a layer thickness of 10 nm, falls to almost zero at layer thicknesses of 0.2 nm, and falls gradually (as $\lambda^{-1/2}$) on the long wavelength (λ) side.

2.4.4 Zener Pinning by Equiaxed and Shaped Particles [16-17]

The driving force for grain growth is the reduction in grain boundary energy as the average grain grows. The most common method used to slow or to stop grain growth is Zener pinning by second phase particles, which works because grains may lower their boundary areas by contacting pins. Energy arguments may be used to estimate the kinetics of grain growth and stagnation. Alternatively, the kinetics may be worked out from curvature arguments in which grain boundaries migrate toward their centers of curvature, and Zener pins work by eliminating curvature. Potts models and physical simulations can be used to differentiate between these two approaches and, consequently, to make better estimates of the kinetics of grain growth in two-phase systems.

The theory of grain growth and stagnation in two dimensions, as calculated in a Potts model, has been compared with experiments on the growth of soap film cells, also in two dimensions. The computed and observed results agree in almost every detail. The kinetics of initial grain growth contain a time exponent of 0.5, and stagnation may be adequately represented by a constant Zener stress opposing growth. The resulting pinned grain structures have a grain area equal to 0.6 times the area occupied by one pin. The grains remain equiaxed even when the pins are aligned and have aspect ratios as high as 10. Only if the product of the pin aspect ratio and area fraction exceeds 1 are the grains elongated. A comparison between two Potts simulations, one of an isolated grain shrinking and the other of a polycrystal coarsening, has given a value for the constant, a , in the grain growth equation $dD/dt = a M$

γ/D , where D is the grain size, γ the grain boundary energy, and M the mobility. The constant $a = 1.0$, which implies that the effective radius of curvature of a growing grain is 4.0 times the actual radius of a grain.

2.5 THEORECTICAL STUDIES AND COMPUTATIONAL MATERIALS SCIENCE

The theory effort in the high-temperature structural materials has concentrated on three areas: infrastructure development, methods development, and applications. We have attempted to engage a broader community than just the AFRL, and to secure resources which support the AFRL research program. In response to AFRL research requirements, a variety of methods were developed to model plastic deformation and the effects of chemistry on phase stability and strength. The research includes work on a variety of materials: Mo, Ta, Ni, Ni₃Al, L1₀ TiAl, Al-Al₃Sc, MgO-Cu, and carbides in TiAl. The details of these material science investigations are summarized briefly in the following section; references to papers published on this work and papers currently in press are included.

2.5.1 Methods

2.5.1.1 Green's Function Boundary Conditions in Atomistic Simulations

In order to determine activation parameters and mobilities for processes like kink pair formation, cross slip, and climb of extended dislocations, a need for three-dimensional atomistic calculations of dislocation activation processes exists. The use of fixed boundary conditions in such simulations may preclude the calculation of accurate formation energies and mobilities of the defect complexities involved in such processes. To relieve the incompatibilities that arise at the boundary of these three-dimensional dislocation simulations, flexible boundary conditions using the Green's function technique were implemented in this research. This technique in combination with a conjugate gradient technique (empirical Embedded Atom Method (EAM) potentials) has been tested successfully for both two and three dimensional dislocation problems in simple metals as well as alloys. In three dimensions, the Green's function technique has been developed and tested for simulations involving both fixed and periodic boundary conditions along the dislocation line. The results of this technique have been written as a journal article in *Philosophical Magazine A* [18]. The Green's function boundary conditions have been implemented with MGPT potentials for Mo as well as first principles calculations in Body Centered Cubic (BCC) Mo, Ta in an effort to study the core structure and mobilities of rigid $a/2[111]$ screw dislocations as well as kinks on such dislocations.

2.5.1.2 Predicting Trends in Ternary and Higher Order Phase Diagrams

We have developed a simple thermodynamic model (the Dilute Solution Model or DSM) for calculating the free energy of a multicomponent alloy using point defect energies derived from first principles calculations [19]. While the model can be generalized to multicomponent systems, it is limited to dilute solute concentrations. In collaboration with Prof. M. Asta (Northwestern University) we have developed an extension to the DSM using the Low Temperature Expansion (LTE) model. In the LTE model thermodynamic quantities are written as an expansion in the defect energies, which are in turn

represented as many one, two, and higher order excitations [20]. This formalism reduces to the DSM in the limit of single particle excitations (noninteracting defects) and can be generalized to double and higher order excitations (interacting defects). Thus, the LTE can be used to model higher concentrations of multicomponent alloys by explicitly calculating defect-defect interaction energies. We have shown in model systems that this increases the concentration range over which the thermodynamic models give reliable results. Also we have made progress in predicting other thermodynamic quantities, such as vibrational entropy in intermetallic alloys. Our experience in the Al/Al₃Sc system has shown that vibrational entropy plays a critical role in determining solubility as a function of temperature.

2.5.1.3 First Principles Green's Function Boundary Condition Method

We have extended the Lattice Green's Function (LGF) Boundary Condition method to work with first principles calculations using a supercell geometry. Two approaches were examined, one in which the dynamical matrix was derived using a direct force method, and another which the LGF was derived using small test forces. The latter method is how the LGF has been derived previously in atomistic simulations. We have demonstrated that supercells can be used to derive the LGF using these methods. Also, we have developed a way of generating supercells which minimize the electrostatic iterations between the dislocations and the boundary of the cells. We have demonstrated the method by simulating screw dislocations in the BCC metals (Mo and Ta) and in L₁₀ TiAl. This research is part of a high profile Grand Challenge Project awarded by the HPCMO in FY98 through FY00.

2.5.1.4 Scalable Parallel Electronic Structure Methods

Electronic structure methods have proven to be useful tools in determining fundamental properties for a wide variety of materials. Traditionally the use of these methods on structural materials is limited by: 1) the size of the calculation needed to simulate the underlying critical phenomena, and 2) our fundamental understanding of the relevant structure-property relationships. In order to address the first of these two issues we engaged in a code development project (~2.0 FTE/year) to produce a robust scalable electronic structure method from FY97 through FY00. The electronic structure code incorporated the following options: dynamic memory allocation, quasi-Newton lattice optimization, a user friendly-interface, and a graphics package for displaying the results. As part of the development cycle, groups of researchers were trained to use the algorithm at special workshops arranged by the High Performance Computing Modernization Office (July, 1998, 1999, and 2000 at the Aberdeen Proving Grounds, Maryland). This work is sponsored by DARPA (160K/year) and is being done in collaboration with Dr. David Singh at the Complex Systems Theory Division at the Naval Research Laboratory.

2.5.1.5 Scalable Parallel Atomistic Methods

Drs. S. I. Rao and C. Woodward have collaborated with members of the Physics H division at Lawrence Livermore Laboratory to develop a scalable parallel atomistic code for metals. The current algorithm uses embedded atom potentials and modified generalized pseudo-potential. We have incorporated the LGF boundary condition method into this code, and the general algorithm is

compatible with a parallel version of the first principles electronic structure codes. The Lawrence Livermore National Laboratory supported this effort with \$30,000, \$10,000, and \$50,000 contracts for FY98, FY99, and FY00, respectively. The code has been completed and can be accessed on the Air Force Systems Command - Material Science Research Center (ASC-MSRC). The code has almost perfect scaling, as shown in Figure 1.

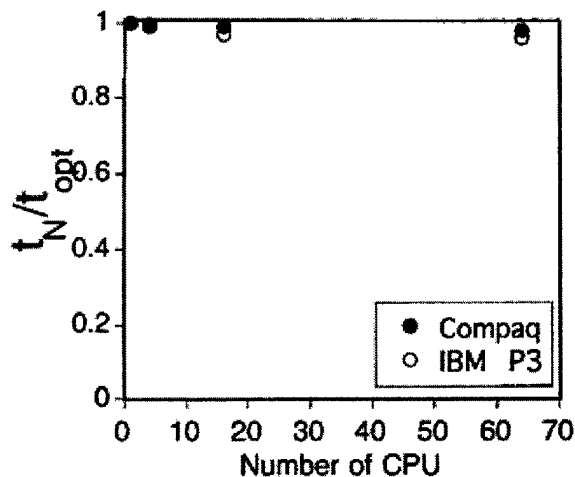


Figure 1. Computational Scaling of the Parallel Atomistics Algorithm Developed at Lawrence Livermore Laboratory in Collaboration with the CMS Group at AFRL

2.5.2 Infrastructure

We have been active in trying to build the infrastructure needed to support computational materials science both here at AFRL and at our partner institutions. In FY98 working with Dr. H. Fraser, Ohio State University (OSU), we submitted a large National Science Foundation (NSF) proposal to form a multidisciplinary research center at OSU. The proposal was well received by the NSF, and we were granted a site visit in June 1999. Unfortunately, the proposal for a Scientific and Technology Center at OSU was not funded. However, in FY00 a smaller project based on the ideas developed in this proposal was funded by NSF. This work is now underway at OSU and involves scientists from across the country. The focus is to accelerate the maturation process of new materials systems by using state-of-the-art computational and experimental methods. The outcome of this research will be a science-based alloy design process which tightly couples scientific inquiry to the metallurgical development of structural materials. This effort also led to our work in the Accelerated Insertion of Materials (DARPA) initiative. This research program has just come on-line at the end of this contract.

To support our Computational Material Science (CMS) effort, we sought large resource allocations from the High Performance Computing Modernization Office. These resources have been used by the group at the AFRL and our university and Department of Energy (DOE) collaborators to study material

systems germane to Air Force requirements. We held a DoD Grand Challenge Project from FY97 to FY00, and garnered significantly more computational resources for our research effort in FY01.

One of the major critical areas that emerged from the 1993 Work Unit Directive (WUD) 55 in house review was the use of parallel processing to perform computational research. The latest generation of parallel processors have enormous potential for applications to material science problems. To take advantage these resources, Dr. C. Woodward obtained DARPA funding (~\$420 k) over 3 years to port serial programs to these parallel platforms (see previous research topic). This work focused exclusively on electronic structure methods.

2.5.3 Applications

2.5.3.1 Atomistic Simulations of Dislocation-Interface Interactions in Cu-Ni Nanolayers

Experimental results show that a nanolayered composite structure made of two kinds of metals strengthens dramatically as the layer thickness is reduced. In epitaxial systems, this strengthening has been attributed to the modulus, lattice parameter, gamma surface and slip-plane mismatches between adjacent layers. The modulus mismatch (Koehler barrier) introduces a force between a dislocation and its image in the interface. The lattice parameter mismatch generates oscillating coherency stresses and Van der Merwe misfit dislocations at or near the interfaces which interact with mobile dislocations. The gamma surface (chemical) mismatch introduces a localized force on gliding dislocations due to core energy changes at or near the interfaces. Slip-plane misorientations across the interfaces require mobile screw dislocations to cross-slip for slip transmission and other dislocations to leave a difference dislocation at the interface. Atomistic simulations using the embedded atom method (EAM) are used to study the four components of dislocation-interface interactions in epitaxial Cu-Ni multilayers in a systematic fashion. The interaction of misfit dislocations with mobile dislocations is modeled using continuum theory. In thick Cu-Ni bilayers, the Koehler barrier is almost independent of interface orientation and dislocation character and is equal to 0.01 to 0.015 μ . But, when the layer thickness is comparable with the core width of a dislocation, the Koehler barrier falls rapidly (from 0.01 μ at a wavelength of 10 nm to 0.004 μ at 1.75 nm). This behavior is in accordance with available experimental observations in the literature on the yield of epitaxial Cu-Ni multilayered systems. The gamma surface mismatch or the chemical strengthening component of the blocking strength of Cu-Ni interfaces to $a/2<110>$ screw dislocations is 0.003 μ , a factor of 3 lower than the Koehler stress. Coherency stresses, apart from exerting direct forces on dislocations, alter the barrier strengths by three mechanisms: (a) they reduce the density of Van der Merwe misfit dislocations, (b) they enhance the Koehler barrier by altering the elastic constants of both Cu and Ni, and (c) nonglide stress components change the core structure of gliding dislocations, thereby altering the Koehler barrier. Overall, the barrier strength of {111} interfaces is independent of the wavelength of the multilayer and ~ 0.02 μ up to a wavelength of λ_c , the coherence wavelength limit. At {001} Cu-Ni interfaces the total barrier strength decreases from a value of 0.02 μ at large wavelengths ($\lambda \sim \infty$) to ~ 0.01 μ at $\lambda = \lambda_c$, as considered by Rao, Hazzledine and Dimiduk, 1995 in their yield stress model for Cu-Ni multilayered structures.

Slip-plane misorientations provide powerful barriers to slip transmission. Even at a {111} twinned interface in a coherent Cu-Ni multilayer, screw dislocations cross-slip onto the interface rather than into Ni because the stacking fault energy at the interface is lower than in Ni. The blocking strength of the same interface to 60° dislocations (which must leave a step and a residual dislocation in the boundary) is very large, 0.03 to 0.04 μ . These results have been written as a journal article in *Philosophical Magazine A* [15] as well as *MRS Proceedings* [21].

2.5.3.2 Atomistic Simulations of Dislocation-Interface Interactions in Cu-Cu Twinned Nanolayers

The strengthening associated with the Cu-Cu twinned nanolayer system can be solely attributed to the slip-plane mismatch between adjacent layers. In this investigation, atomistic simulations are used to study the interaction of a 60° $a/2[110]$ dislocation with a Cu-Cu twinned nanolayer. It is found that a shear stress of 0.04 μ is required for the $a/2[110]$ dislocation to cross the first interface. A higher stress of 0.08 μ is required for the subsequent unhindered motion of the $a/2[110]$ dislocation since it has to drag a high energy fault behind it. These results indicate that the strengthening achievable in the Cu-Cu twinned nanolayer system can be substantial. These results are being written as a journal article.

2.5.3.3 Dislocation-Interface Interactions in α Ti- β Ti

Experimental results in the α Ti- β Ti system by Prof. M. Mills and his group at Ohio State University suggest that the yield, work hardening, and creep behavior of the α Ti- β Ti system is strongly dependent on the slip system that is operative, i.e., whether a_1 or a_2 dislocations are operative. Here, atomistic simulations are used to study the interaction of a_1 and a_2 dislocations in the α layer with the appropriate α Ti- β Ti interface. It is found that the interaction is anisotropic, i.e., that the α - β interface interacts strongly with the a_2 dislocation as compared to the a_1 dislocation. This is attributed to the different slip plane mismatches between adjacent layers for the moving dislocations. These results are being written as a journal article.

2.5.3.4 Frank-Read Source Simulation

The newly developed two- and three-dimensional Green's function technique for atomistic simulations has been applied to study the operation of a Frank-Read source in metallic alloys. The objective of the research is to understand dislocation multiplication at an atomistic level. Also, the development of such an atomistic procedure is expected to be useful in understanding work hardening phenomenon in metals and alloys. Initially, two angular dislocations were introduced in a perfect Ni crystal, using the displacement field solution from the work of Yoffe et al. The structure of the dislocation configuration thus introduced was checked using differential displacement plots. The dislocation configuration was relaxed, using the EAM potential for FCC Ni, to obtain its atomistic core structure. Differential displacement field plots were used to characterize the relaxed core structure. It was found that along the short segment of the dislocation configuration (8 nm in length), the dislocation dissociates into Shockley partials with the separation distance being a maximum in the middle and a minimum at the ends. The amount of constriction at the ends is approximately a factor of 2. The dissociation distance

in the middle is identically equal to the value obtained for an infinite $a/2[110]$ edge dislocation. Using fixed boundary conditions in the atomistic simulations, the bowing of the short segment was obtained at two glide stresses, $.01 \mu$ and $.025 \mu$. It was found that the short arm of the dislocation bows in its glide plane as expected. However, the two semi-infinite long arms of the dislocation bends its glide plane, also. To clarify whether the application of pure glide stresses or pure glide strains influenced this behavior, both types of stress states were studied. Some quantitative differences in the response of the dislocation configuration was detected. However, qualitatively, the responses were very similar between the two stress states.

Similarly, an identical simulation with Green's Function (GF) boundary conditions applied on three of the four faces of the simulation cell was used to obtain the relaxed dislocation configuration. Molecular static simulations combined with the newly developed Green's function boundary conditions for atomistic simulations in 3-D have been used to determine the bowing of the 8-nm- long dislocation segment under various applied stresses. Stresses ranging from 0.0025μ to 0.01μ were considered in the calculations. Results of these simulations were compared with similar calculations performed using fixed boundary conditions. It is found that at a stress of 0.01μ , with GF boundary conditions, the dislocation segment bows in its glide plane approximately a factor of 2 larger than in the fixed boundary simulations. The atomistic results of bowing have been compared with continuum calculations. Results of these simulations are published in *Scripta Materialia* [22].

2.5.3.5 Self-Energy of Small Loops

Atomistic techniques have been used to obtain the self-energy of small glide shear dislocation loops. The purpose is to obtain the trends in the shear loop energies as a function of their radii. These calculations are expected to give useful inputs/insights into the Khantha/Pope/Vitek/Sun model of ductile-brittle transition in metals/intermetallics/semiconductor materials. Atomistic simulations of the self-energy of small loops with radii ranging from $1.5 b$ to $10 b$ have been completed, using an EAM potential for FCC Ni. Small radii loops, with radii ranging from 1.5 to $10 b$, were introduced into the simulation cell. Stresses required for the unstable equilibrium of loops of various sizes were determined. The equilibrium stresses obtained atomistically converge to continuum values at relatively large radii ($5 b$ to $10 b$). However, at smaller radii ($1.5 b$ to $3 b$), the atomistic results deviate strongly from the continuum values, with the atomistic values being higher. Introduction of a core energy correction term to the continuum expressions results in an excellent fit to the atomistic values at smaller radii; however, this correction term introduces a significant departure from the atomistic values at larger radii. The results of these simulations have been written as a journal article in *Scripta Materialia* [23].

2.5.3.6 Core Structure and Mobility of $a/2[111]$ Screw Dislocations in BCC Mo

Atomistic simulations using a MGPT potential and Green's function boundary conditions were employed to determine the Peierls stress of rigid straight $a/2<111>$ screw dislocations for the application of shear stresses on {110}-and {112}-type planes in BCC Mo. It is found that the Peierls stress of $a/2<111>$ screw dislocations for the application of shear stress on the {110} planes is 0.0175 to 0.020μ . Large twinning-antitwining asymmetry is found for the application of pure shear stress on

the $\{112\}$ planes with the Peierls stress along the twinning direction being 0.0125 to 0.020 μ and along the antitwinning direction to be 0.050 to 0.05625 μ . The Peierls stress of screw dislocations for the application of tensile and compressive stresses along $\{001\}$, $\{110\}$, $\{111\}$, and $\{201\}$ directions were also determined. A large tension-compression asymmetry is observed for the $\{001\}$, $\{110\}$ and $\{111\}$ directions. This is a manifestation of the twinning-antitwinning asymmetry observed in the pure shear stress calculations. A tension-compression asymmetry is also observed for the $\{201\}$ direction, indicating that nonglide stress effects are also important in determining the Peierls stress. To facilitate an understanding of $a/2<111>$ screw dislocation motion by the kink pair mechanism, the core structure and energetics of six possible kinks and two Anti-Phase Boundary (APD) defects on $a/2<111>$ screw dislocations were also determined. It is found that the kink pair formation energy at infinite separation distance varies between 1.46 and 2.10 eV which is in reasonable accord with the experimental value of 1.27 eV. These results have been written as a journal article in *Philosophical Magazine A* [24].

2.5.3.7 Cross-Slip of $a/2[110]$ Screw Dislocations in Model FCC Structures

Three-dimensional, cross-slipped core structures of $a/2[110]$ screw dislocations in model FCC structures are simulated using lattice static within the Embedded Atom Method (EAM) formalism. Two parametric EAM potentials fitted to the elastic and structural properties of FCC Ni were used for the simulations. The newly developed two-and three-dimensional GF are used to relax the boundary forces in the simulations. Core structures and energetics of the constrictions occurring in the cross-slip process are studied. The core structure of the constrictions are diffuse, as opposed to a point constriction as envisaged by Stroh. The two constrictions formed by cross-slip onto a cross $\{111\}$ plane have significantly different energy profiles, at variance with classical continuum theory. This suggests that self-stress forces and atomistics dominate the energetics of the cross-slip process; the far-field elastic-energy contribution to cross-slip appears to be minimal. However, the Shockley partial separation distances near the constrictions, as well as the variation in cross-slip energy with stacking-fault energy, are in reasonable agreement with continuum predictions. Cross-slip energies estimated for Cu and Ni from these calculations show reasonable agreement with experimental data. The cross-slip energy shows a significantly weaker dependence on Escaig stress as compared to elasticity calculations. The activation volume for the cross-slip process is estimated to be of the order of $20 b^3$ at an applied Escaig stress of $10^{-3} \mu$ in Cu, an order of magnitude lower than experimental estimates and continuum predictions. These results have been written as a journal article in *Philosophical Magazine A* (P8) as well as *MRS Proceedings* [25].

2.5.3.8 Cross-Slip Obstacles on $a/2[110]$ Screw Dislocations in $L1_0$ TiAl

The yield anomaly identified in γ -TiAl has been related to the formation of cross-slip obstacles on $a/2[110]$ screw dislocations. TEM observations of $a/2<110>$ screw dislocations in the yield anomaly regime show a large density of jogs on the screw dislocation segments, and has been shown to be formed as a result of double cross-slip. Previous 2-D simulations of the core structure of $a/2<110>$ screw dislocations show that their core is compact and has a significant Peierls barrier. Here, some results of 3-D simulations of the elementary cross-slip processes occurring in $L1_0$ TiAl are given.

The energy of cross-slip in $L1_0$ TiAl was determined parametrically, as a function of complex stacking-fault energy, using EAM potentials fit to properties of γ -TiAl. The cross-slip energy determined at a fault energy of 300 mJ/m² is in agreement with experimental observations of average spacing between cross-slip obstacles in the yield anomaly regime. Core structure and energetics of a Viguier lock or $a\langle 110 \rangle$ jog were also determined using 3-D simulations. The jog is diffuse in structure with a width of 6 b and has a formation energy of 0.69 eV. At the center of the jog, the core of the $a/2\langle 110 \rangle$ dislocation is completely contained in the cross-slip plane. The interaction energy between the two elementary kinks forming the jogs is found to be significantly smaller than continuum estimates. These results have been written as a journal article in *TMS Proceedings* [26].

2.5.3.9 The Influence of Solid Solutions on Flow Behavior in γ -TiAl

Modifications of alloy chemistry are often used to tailor the intrinsic flow behavior of structural materials. Models of solution strengthening, high-temperature yield stress and creep must relate the effects of chemistry to the mechanisms that influence these material properties. In ordered alloys, additional information regarding the crystallographic site occupancy of ternary elements is required. Relaxed structures and energies for intrinsic and substitutional point defects are calculated using a first principles plane-wave-pseudopotential method. Calculated defect energies were used to predict the density and site preferences of solid solutions (Si, Cr, Nb, Mo, Ta and W) in γ -TiAl. Size and modulus misfit parameters were calculated and the interaction of these defects with a dissociated ordinary screw dislocation evaluated within anisotropic elasticity theory. The derived interaction strength was then related to solid solution strengthening for these defect centers. We found that the predicted solid solution effects were in good agreement with experimental observations for the binary alloy. Several papers were published using these data. The manuscripts entitled "Computational Tools for Alloy Design: Solid Solutions in γ -TiAl," and "Site Preferences and Formations Energies of Substitutional Si, Nb, Mo, Ta and W Solid Solutions in $L1_0$ TiAl," give the most comprehensive reviews of this work.

Models of creep in intermetallic alloys must account for the influence of chemistry on the available intrinsic creep mechanisms. As in simple metals the presence of vacancies strongly influences bulk diffusion processes in these materials. Limiting the density of constitutional and thermal vacancies by alloying may produce materials with enhanced creep properties. The energy of intrinsic and substitutional point defects in $L1_0$ TiAl were calculated within a first principles, local density functional theory framework. Relaxed structures and energies for vacancies, antisites and solid solutions are calculated using a plane-wave-pseudopotential method. Calculated defect energies were used within a canonical ensemble formalism to estimate the point defect densities as a function of temperature and composition. The density of vacancies was found to be sensitive to the underlying stoichiometry of TiAl. The dependence of the vacancy concentration for solid solutions of Si, Cr, Nb, Mo, Ta and W was also predicted. This work was published in a manuscript entitled "Density of Thermal Vacancies in γ -TiAl-M, M= Si, Cr, Nb, Mo, Ta, or W."

2.5.3.10 First Principles Simulation of Deformation Modes in Refractory Metals

Modern dislocation theory suggests that the flow and fracture of these materials is mediated by screw dislocations spread on conjugate glide planes. Unfortunately, these dislocation cores cannot be imaged using transmission electron microscopy, and simulations of the dislocation core structures have had to rely on physically unrealistic atomistic potentials. We are using first principles electronic structure methods in conjunction with a novel boundary condition scheme to directly model isolated straight dislocations. Previously, the lattice Green's function boundary condition (GFBC) method has been used in atomistic simulations where simulation sizes were significantly reduced (>90 percent) while maintaining the integrity of the core region. We have derived the lattice Green's function using a first principal plane-wave-pseudopotential method. Also, we have successfully relaxed $a/2<111>$ screw dislocations in BCC Mo and Ta using the first principles-GFBC method (FP-GFBC). The derived dislocation cores for Mo and Ta are spread symmetrically around a central point in the (111) plane. All previous atomistic work has shown the Mo core to spread asymmetrically on (110) planes. While the shape of the Mo core is different from previous atomistic results the lattice friction stress for movement on the (110) and (112) planes is in good agreement with recent atomistic results based on state-of-the-art potentials (modified generalized pseudopotential method). Also, in Mo the straight dislocations always moves on (110) planes, as found in previous by atomistic simulations. This suggests that we cannot accurately characterize the macroscopic behavior of the group V and VI BCC transition metals by the shape of their respective $a/2(111)$ screw dislocation cores as has been the practice for the last 20 years. These results have been published in a manuscript entitled "Ab-initio Simulation of Isolated Screw Dislocations in BCC Mo and Ta." Another manuscript, entitled "First Principles Method for Simulating Extended Defects in Metals: Dislocations in BCC Ta and Mo," which discusses the method in more detail, has been submitted to *Physical Review Letters*.

2.5.3.11 First Principles Simulation of Deformation Modes in Intermetallics

We have completed simulations of the equilibrium $a/2<110]$ screw dislocation in γ -TiAl, which is thought to play the same role in TiAl as the $a/2<111>$ screw dislocations in the BCC metals. We have determined one possible geometry of the equilibrium core. The core is found to be spread on two conjugate (111) planes, similar to previous atomistic results. The placement of the core can be correlated to the bonding found in TiAl, the dislocation tends to favor a configuration that shears weak bonds between nearest neighbor Al atoms (Figure 2).

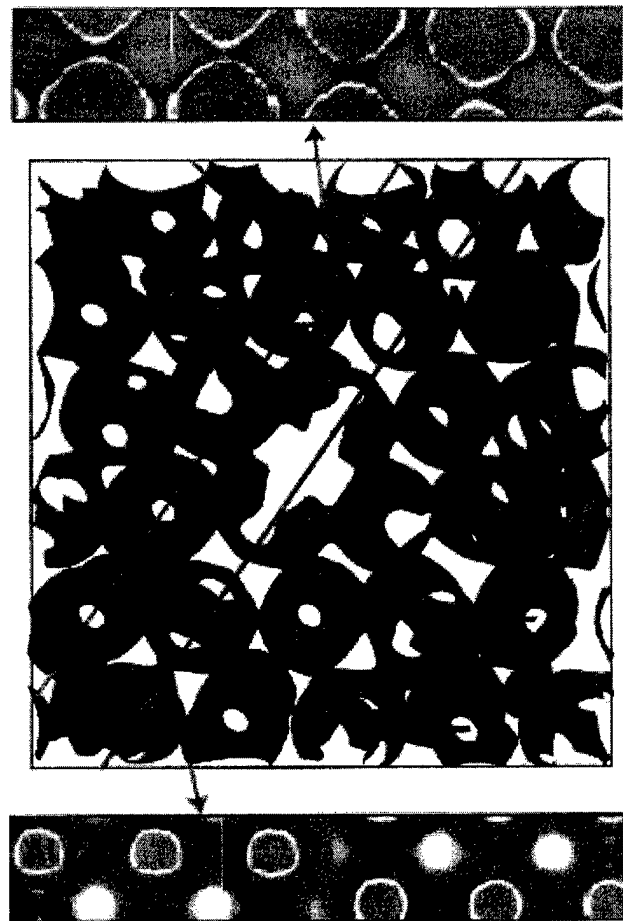


Figure 2. Isosurface Charge Density Plot of the Charge Density Near an $a/2\langle 110 \rangle$ Screw Dislocation in $L1_0$ -TiAl

This work was presented at the February The Minerals, Metals & Materials Society (TMS) meeting in a contributed talk entitled 'First Principles Simulations of $a/2\langle 110 \rangle$ Screw Dislocations in g-TiAl.'

2.5.3.12 First Principles Simulation of Metal/Oxide Interfaces

The evolution of metal/oxide interfaces (e.g., oxidation and corrosion) is an extremely important materials problem for high-temperature structural materials. The lifetime of in-service components (materials) is often limited by oxidation properties. Similarly, oxidation resistance continues to be the main limiting factor for new materials systems, such as the refractory metal-intermetallics. We have performed for the first time ab-initio calculations of an incoherent metal/oxide interface ($\{111\}$ MgO-Cu). These were accomplished in collaboration with Dr. Roy Benedek using part of the Grand Challenge time allocated by the HPCMO. This model system has been studied extensively using field

ion probe microscopy making it an ideal model system to study using first principle methods. The work of cohesion is also being calculated with and without ternary additions (Ag) on the interface. A paper on this work, entitled "Electronic Structure of a Model Ceramic-Metal Interface: {222} MgO-Cu," was published in *Physical Review Letters*.

In the titanium aluminides, γ -TiAl, incoherent (or semicoherent) carbide, silicide and oxide precipitates are being used to improve creep properties at high temperatures. These are typically small precipitates, formed under heat treatments tailored to dissolve a second, α_2 phase, which has a high solubility for O, C and Si. The particles precipitate out of α_2 as the volume fraction of this phase decreases. Specific dislocation-precipitate interactions are not well documented, and in general it is not well known if the major strengthening component is due to these precipitates or very small coherent precipitates in the TiAl matrix. Coherent interfacial boundaries between the γ -TiAl matrix and the H-type (Ti_2AlC hexagonal) phase have been characterized in samples of a commercial TiAl alloy after undergoing creep at 800 °C. We are studying this interfacial boundary using electronic structure calculations. Preliminary calculations have determined the hierarchy of boundary energies as a function of termination. We will then calculate the energy of point defects (constitutional and thermal) near the interface planes. These data will be used to fit interatomic potentials for the TiAl-Ti₂AlC system. The interaction of dislocations with microscopic precipitates will then be modeled using large scale atomistic simulations.

2.5.3.13 Predicting Solubility and Trends in Ternary and Higher Order Phase Diagrams Using the Dilute Solute Model (DSM)

The DSM for calculating the free energy of a multicomponent alloy was published by Dr. C. Woodward as part of a Phys., Rev. B manuscript in 1998. In collaboration with Dr. M. Asta (Sandia National Laboratory), we are now using a similar scheme to calculate host-precipitate interfacial energies in the Al-Al₃Sc alloy system. These results can be used to predict the solubility of the Sc in the Al host. Further, we are predicting the density of ternary elements (Mg and Hf) in the two phases and how changes in chemistry will influence the interfacial energies. The defect energies are calculated using first principles methods and then incorporated into a Grand Canonical Ensemble representing the two phases in equilibrium. By including the interface energies, the difference in the chemical potentials and an estimate of the host/precipitate vibrational entropy we can predict the solubility of Sc in Al as a function of temperature and alloy composition. A similar procedure can be used to predict the size distribution and stability of γ' in the nickel superalloys. A preliminary manuscript entitled "Density of Constitutional and Thermal Point Defects in L₁₂ Al₃Sc" was published in *Physical Review B*.

2.5.3.14 The Hierarchy of Planar Fault Energies in γ TiAl

From FY95 to FY97 we used a first principles method (LKKR-CPA) to calculate planar fault energies in γ TiAl over a range of compositions, for both the binary alloy and for ternary additions (Cr, Nb and Mn). The predicted variation in planar fault energies was used in conjunction with anisotropic theory to examine the influence of composition on the driving forces for the cross-slip of <101] super dislocations in TiAl. A manuscript documenting this work, entitled "Planar Fault Energies and Sessile Dislocations in Substitutionally Disordered TiAl with Nb and Cr Additions," was published during the previous

contract. The results of these calculations have been controversial in that the hierarchy of energies was found to be inconsistent with traditional, bond counting models of planar defect energies. In 1992, Dr. C.L. Fu (Oak Ridge National Lab.) found the traditional ordering of the planar defect energies using FLAPW methods. However, in FY97 we confirmed the hierarchy of energies found in our original LKKR work using an alternative method (pseudo potential-plane-wave method), and these results have been confirmed by a group of researchers at Sandia National Lab. (Dr. M. Asta). In addition, C.L. Fu has made corrections to his previous work which verify our original findings. These new values for the planar defect energies have been corroborated by Dr. M. Mehl (Naval Research Lab.) and Dr. A. Quong (Sandia Nat. Lab) using the FLAPW method.

2.6 PUBLICATIONS

1. E.S.K. Menon, P.R. Subramanian, and D.M. Dimiduk, "Phase Transformations in Nb-Al-Ti Alloys," *Metall. Mater. Trans. A*, 27A, pp. 1647-59 (1996).
2. P.R. Subramanian, M.G. Mendiratta, D.M. Dimiduk, and M.A. Stucke, "Advanced Intermetallic Alloys—Beyond Gamma Titanium Aluminides," *Mater. Sci. & Engr. A*, A239-240, pp. 1-13 (1997).
3. G.A. Henshall, P.R. Subramanian, M.J. Strum, and M.G. Mendiratta, "Continuum Predictions of Deformation in Composites with Two Creeping Phases -II. Nb₅Si₃/Nb Composites," *Acta Mater.*, 45, pp. 3135-3142 (1997).
4. T.A. Parthasarathy, M.G. Mendiratta and D.M. Dimiduk, "Observations on the Creep Behavior of Fully Lamellar Polycrystalline TiAl Alloys: Identification of Critical Effects," *Scripta Mater.*, 37, pp. 315-321 (1997).
5. D.M. Dimiduk, P.M. Hazzledine, T.A. Parthasarathy, S. Sriram and M.G. Mendiratta, "The Role of Grain Size and Selected Microstructural Parameters in Strengthening Fully-Lamellar Ti-Al Alloys," *Met. and Mater. Trans. A*, 29A, pp. 37-47 (1998).
6. M.G. Mendiratta and D.M. Dimiduk, "Flow Behavior of PST and Fully Lamellar Polycrystals Ti-48Al in the Microstrain Regime," *Acta Mater.*, 46, pp. 4005-4016 (1998).
7. T.A. Parthasarathy, M. Keller and M.G. Mendiratta, "The Effect of Lamellar Lath Spacing on the Creep Behavior of Fully Lamellar Ti-47Al," *Scripta Mater.*, 38, pp. 1025-1031 (1998).
8. B.P. Bewlay, M.R. Jackson, and P.R. Subramanian, "Processing High-Temperature Refractory-Metal Silicide In-Situ Composites," *JOM*, 51(4), pp. 32-36 (1999).
9. S. Veeck, M.G. Mendiratta, and D.J. Evans, "Cast and HIP'ed Ti-62222S Alloy," *Adv. Mater. and Proc.*, 156, pp. 41-44 (1999).

10. T.A. Parthasarathy, P.R. Subramanian, M.G. Mendiratta and D.M. Dimiduk, "Phenomenological Observations of Lamellar Orientation Effects on the Creep Behavior of Ti-48%Al PST Crystals," *Acta Mater.*, 48, pp. 541-551 (2000).
11. M.G. Mendiratta, T.A. Parthasarathy, and D.M. Dimiduk, "Oxidation Behavior of α -Mo₃Si-Mo₅B₂(T2) Three Phase System," AFRL/MLLM, Wright-Patterson AFB OH 45433 and UES Inc., 4401 Dayton-Xenia Rd., Dayton, OH 45432, paper in review in *Intermetallics*.
12. Y-W. Kim and D.M. Dimiduk, "Design Gamma TiAl Alloys," *Structural Intermetallics*, Seven Springs, PA, 21-26 September 1997, pp. 531-543 (1997).
13. Z. Jin, G.T. Gray III, Y-W. Kim, and M. Yamaguchi, "Mechanical Behavior and Microcrack formation in g-TiAl Alloys as a Function of Strain-Rate and Temperature," In *Structural Intermetallics*, eds. M. V. Nathal, R. Darolia, et al., TMS, Warrendale, PA, pp. 225-233 (1997).
14. Y-W. Kim and D.M. Dimiduk, "Deformation and Fracture Behavior in TiAl Alloys under Monotonic and Cyclic Tensile/Tension Loading Conditions," in *Cleavage Fracture: Theory, Experimental, and Modeling*, eds. Kwai S. Chan and Rao K. Mahidhara, TMS, Warrendale, PA, pp. 305-317 (1997).
15. T.L. Lin, Y. Wang, Y. Lin, and Y-W. Kim, "Strain-Rate Sensitivity of Mechanical Behavior in a Two-Phase TiAl Alloy," *MRS Proc.* Vol. 460, pp. 65-71 (1997).
16. Z. Jin, G.T. Gray III, and Y-W. Kim, "Texture Characterization in a-Forged g-TiAl Alloys," *Materials Sci. & Eng.*, A239-240, pp. 729-739 (1997).
17. Y-W. Kim and D.M. Dimiduk, "Designing Gamma TiAl Alloys: Fundamentals, Strategy and Production," in *Structural Intermetallics*, eds. M. V. Nathal, R. Darolia, et al., TMS, Warrendale, PA, pp. 531-543 (1997).
18. D.M. Dimiduk, P.L. Martin, and Y-W. Kim, "Microstructure Development in Gamma Alloy Mill Products by Thermomechanical Processing," *Mater. Sci. & Eng.*, A 243, pp. 66-76 (1998).
19. H.S. Cho, S.W. Nam, and Y-W. Kim, "Primary Creep Deformation Behaviors in a Fully-Lamellar TiAl Alloy," *Metals & Materials*, 4 (1), pp. 33-37 (1998).
20. P. I. Gouma, Y-W. Kim, and M. J. Mills, "Characterization of the Precipitation Process in a TiAl-Based Alloy with Carbon and Silicon Additions," *Phil Mag. Lett.*, 78(1), pp. 59-66 (1988).
21. P.I. Gouma, K. Subramanian, Y-W. Kim, and M.J. Mills, "Annealing Studies of γ -Titanium Aluminides Alloyed with Light Elements for Creep Strengthening", *Intermetallics*, 6, pp. 689-693 (1998).

22. H.S. Cho, S.W. Nam, and Y-W. Kim, "Primary Creep Deformation Behaviors in a Fully-Lamellar TiAl Alloy, *Metals & Materials*, 4 (1), 33-37 (1998).
23. P.I. Gouma, G.B. Viswanathan, Y.-W. Kim, and M.J. Mills, "Creep-Deformed Microstructures of a TiAl-based Alloy Containing Carbon and Silicon Additions," submitted to *Phil. Mag.* for publication (1998).
24. Y-W. Kim, "Designing Gamma Alloys for Improved Balance in Properties," in *Ordered Intermetallics and Composites-III*, eds. D.L. Lin and C.T. Liu, Hangzhou, China, in press (1998).
25. Y-W. Kim, "Strength and Ductility of TiAl Alloys," *Intermetallics*, 6, pp. 623-628 (1998).
26. Y-W. Kim, "Design Fundamentals for Gamma TiAl Alloys," in *Interstitial and Substitutional Solute Effects in Intermetallics II*, eds. I. Baker and R. Noebe, TMS, Warrendale, PA, pp. 189-200 (1998).
27. Y-W. Kim, "Advances in the Fundamental Understanding for Designing Engineering Gamma TiAl Alloys," *J. of the Chinese Institute of Engineers*, 22 (1), pp. 13-25 (1999).
28. P.I. Gouma, K. Subramanian, Y-W. Kim and M.J. Mills, "Precipitation and Creep Strengthening Mechanisms in K5 Series γ -TiAl alloys," *MRS Proc.*, 487, p. KK2.11.1 (1999).
29. W.J. Zhang, Z.C. Liu, G.L. Chen, and Y-W. Kim, "Deformation Mechanism in a High-Nb Containing -TiAl Alloy at 900°C," *Phil. Mag.*, A79, pp. 1073 (1999).
30. Y. Wang, D. Lin, and Y-W. Kim, "High Strain-Rate Tensile Properties of a TiAl Alloy in Duplex and Fully-Lamellar Microstructural Forms," *Trans. of Nonferrous Met. Soc. of China*, 9, pp. 437-441 (1999).
31. G. Chen, W.J. Zhang, Z.C. Liu, S.J. Li, and Y-W. Kim, "Microstructure and Properties of High-Nb Contained TiAl-Based Alloys," in *Gamma Titanium Aluminides*, eds. Y-W. Kim, D.M. Dimiduk and M.H. Loretto, TMS, Warrendale, PA, pp. 371-380 (1999).
32. G.B. Viswanathan, Y-W. Kim, and M.J. Mills, "On the Role of Precipitation Strengthening in Lamellar Ti-46Al Alloy with C and Si Additions," in *Gamma Titanium Aluminides*, eds. Y-W. Kim, D.M. Dimiduk and M.H. Loretto, TMS, Warrendale, PA, pp. 653-660 (1999).
33. Y-W. Kim and K.V. Jata, "Crack Growth in a Nearly Fully-Lamellar Gamma TiAl Alloy at 650°C and 800°C under Sustained Load," in *Gamma Titanium Aluminides*, eds. Y-W. Kim, D.M. Dimiduk and M.H. Loretto, TMS, Warrendale, PA, pp. 509-516 (1999).

34. M. Yoshihara and Y-W. Kim, "A Comparative Study of Oxidation Resistance of Engineering Gamma TiAl Alloys," in *Gamma Titanium Aluminides*, eds. Y-W. Kim, D.M. Dimiduk, and M.H. Loretto, *TMS*, Warrendale, PA, pp. 753-760 (1999).
35. K.V. Jata and Y-W. Kim, "Creep Crack Growth in Nearly Fully Lamellar Gamma TiAl Alloys," in *8th Int'l Conf. on Creep and Fracture of Engineering Materials and Structures, (CFEMS-8)*, 1-5 Nov., 1999, Tsukuba, Japan, *Key Eng. Materials*, Trans Tech Publications, vol. 171-174, pp.147-152 (2000).
36. M. Yoshihara and Y-W. Kim, "Oxidation Behavior of Engineering Gamma Titanium Aluminide Alloys," in *Corrosion*, NACE, Houston, TX, 1999, Conference paper No. 244 (2000).
37. Z. Jin, C. Cady, G.T. Gray III, and Y-W. Kim, "Mechanical Behavior of a Fine-Grained Duplex TiAl Alloy," *Metall. and Mater. Trans. A*, 31A (3), pp. 1007-1015 (2000).
38. M. Yoshihara and Y-W. Kim, "The Oxidation Behavior of Engineering Titanium Aluminide Alloys," in *J. of Japan Institute of Metals*, Vol. 64 (11) (2000), in press.
39. M. Yoshihara and Y-W. Kim, "Oxidation Resistance of Various Engineering Gamma Titanium Aluminide Alloys," in *Proc. of Int'l Symp. on High-Temperature Corrosion and Protection 2000*, 17-22 Sep. 2000, Hokkaido, Japan, in press.
40. Y-W. Kim and D.M. Dimiduk, "Gamma TiAl Alloys: Emerging New Structural Metallic Materials," in *Proc. of Int'l Symp. on Advanced Materials (ISAM)*, October 11-13, 2000, Beijing, China, to be published.
41. Y-W. Kim and K.V. Jata, "High Temperature Crack Growth in a TiAl Alloy under Constant Loading Conditions," revised version submitted for publication *Metall. and Mater. Trans. A*. (2001).
42. Y-W. Kim and D.M. Dimiduk, "Effect of Boron Addition on Grain refinement and Lamellar formation in Wrought-Processed Gamma Alloys," in *Structural Intermetallics*, eds. K. Hemker and D. M. Dimiduk, *TMS Book*, Warrendale, PA (2001), in press.
43. P.M. Hazzledine and S.I. Rao, "Yield Stress of Nano- and Micro- multilayers," in *Layered Materials for Structural Applications*, eds J.J. Lewandowski, C.H. Ward, M.R. Jackson, and W.H. Hunt, *MRS*, Pittsburgh, PA, pp. 135-140 (1996).
44. M.A. Grinfeld and P.M. Hazzledine, "Role of Vacancies in Slow Evolution of Traction-free Interfaces," *Europhysics Letters*, 37, pp. 409-414 (1997).

45. S. Sriram, D.M. Dimiduk, P.M. Hazzledine, and V.K. Vasudevan, "The Geometry and Nature of Pinning Points of $1/2<110]$ Unit Dislocations in Binary TiAl Alloys," *Philos. Mag.* 76A, pp. 965-993 (1997).

46. V. Berdichevsky, P.M. Hazzledine, and B. Shoykhet, "Micromechanics of Diffusional Creep," *International Journal of Engineering Science*, 35, pp.1003-1032 (1997).

47. B.K. Kad and P.M. Hazzledine, "Monte Carlo Simulations of Grain Growth and Zener Pinning," *Materials Science and Engineering A238*, pp. 70-77 (1997).

48. D.M. Dimiduk, P.M. Hazzledine, T.A. Parthasarathy, S. Sriram, and M.G. Mendiratta, "The Role of Grain Size and Selected Microstructural Parameters in Strengthening Fully-Lamellar Ti-Al Alloys," *Met. Mat. Trans.* 29A, pp. 37-47 (1998).

49. M.A. Grinfeld, P.M. Hazzledine, B. Shoykhet and D.M. Dimiduk, "Coherency Stresses in Lamellar Ti-Al," *Met. Mat. Trans.* 29A, pp. 937-942 (1998).

50. B. Shoykhet, M.A. Grinfeld, and P. M. Hazzledine, "Internal Stresses and Strains in Coherent Multilayers," *Acta Materialia*, 46, pp. 3761-3766 (1998).

51. S. Sriram, D.M. Dimiduk, and P.M. Hazzledine, "Deformation Substructure Evolution pertaining to $1/2<110]$ Unit Dislocations in TiAl Alloys," in Structural Intermetallics, eds. M.V. Nathal, R. Darolia, C.T. Liu, P.L. Martin, D.B. Miracle, R. Wagner, and M. Yamaguchi, *TMS*, Warrendale, PA, pp. 157-166 (1997).

52. P.M. Hazzledine, M.A. Grinfeld, and S.I. Rao, "Coherency and Loss of Coherency in Multilayers" in Thin Films- Stresses and Mechanical Properties VII, eds. R.C. Cammarata, M.A. Nastasi, E.P. Busso, and W.C. Oliver, *MRS Symposium Proceedings*, 505, pp. 180-186 (1998).

53. Y.Q. Sun, P.M. Hazzledine, and D.M. Dimiduk, "Stress-biased Collective Nucleation of Dislocation Loops," in Phase Transformations and Systems Driven Far from Equilibrium, eds. E. Ma, P. Bellon, M. Atzmon and R. Trivedi, *MRS Symposium Proceedings*, 481, pp. 261-267 (1998).

54. Y.Q. Sun, P.M. Hazzledine, and D.M. Dimiduk, "Formation of Dislocations in Ni-Al Single Crystals Studied by In-situ Electrical Resistively Measurement," in *Electrically Based Microstructural Characterization II*, eds, R.A. Gerhardt, M.A. Alim, and S. R. Taylor, *MRS Symposium Proceedings* 500, pp. 214-220 (1998).

55. P.M. Hazzledine, B. Shoykhet, and M.A. Grinfeld, "Coherency Strains and Stresses in Lamellar Ti-Al," P.M. Hazzledine, *Solid State Phenomena*, 59-60, pp. 133-144 (1998).

56. R.A. Masumura, P.M. Hazzledine, and C.S. Pande, "Yield Stress of Fine Grained Materials", *Acta Materialia*, 46, pp. 4527-4534 (1998).
57. P.M. Hazzledine, "Coherency and Loss of Coherency in Lamellar Ti-Al," *J. Intermetallics*, 6, pp., 673-677 (1998).
58. P.M. Anderson, T. Foecke and P.M. Hazzledine, "Physical and Computer Simulations of Grain Growth in a Pinned Microstructure," eds. H. Weiland, B.L. Adams, and A.D. Rollett. *TMS*, Warrendale, PA, pp. 147-152 (1998).
59. S.I. Rao and P.M. Hazzledine, "Simulation of an Edge Source in the Cu-Ni Multilayer System," *Scripta Mater.*, 41, pp. 1085-1090 (1999).
60. P.M. Hazzledine and D. M. Dimiduk, "Microstructural Strengthening of Fully Lamellar Ti-Al Alloys," in Gamma Titanium Aluminides, eds. Y-W Kim, D.M. Dimiduk and M.H. Loretto, *TMS*, Warrendale, PA, pp. 481-487 (1999).
61. S.I. Rao and P.M. Hazzledine, "Atomistic Simulations of Tiny Glide loops in FCC Ni," *Scripta Mater.*, 42, pp. 57-60 (2000).
62. S.I. Rao and P.M. Hazzledine, "Atomistic Simulations of Dislocation-Interface Interactions in the Cu-Ni Multilayer System," in *Multiscale Phenomena in Materials Experiments and Modeling*, eds. D.H. Lassila, I.M. Robertson, R. Phillips and B. Devincre, MRS, Warrendale, PA, pp. 389-394 (2000).
63. S.I. Rao and P.M. Hazzledine, "Atomistic Simulations of Dislocation-Interface Interactions in the Cu-Ni Multilayer System," *Philos. Mag. A*80, 2011 (2000).
64. P.M. Anderson, S.I. Rao, Y. Cheng, and P.M. Hazzledine, "The Critical Stress for Transmission of a Dislocation Across an Interface: Results from Peierls and Embedded Atom Models," in *Interface Engineering for Optimized Properties*, eds. C.B. Carter, E.L. Hall, C.L. Brian, and S. Nutt. MRS, Warrendale, PA, pp. 267-272 (2000).
65. Y.H. Wen, L.Q. Chen, P.M. Hazzledine, and Y. Wang, "A Three-Dimensional Phase Field Model for Computer Simulation of Lamellar Structure Formation in γ Ti-Al Intermetallic Alloys," *Acta Materialia*, (2001), in press.
66. M. Olguin, C.H. Ortiz, O. Worner, B.K. Herrera, B.K. Kad, and P.M. Hazzledine, "Zener Pins and Needles," *Philos. Mag. B*, 2001, in press.
67. C. Woodward and S.I. Rao, "First Principles Method for Simulating Extended Defects in Metals: Dislocations in BCC Ta and Mo," submitted to *Phys. Rev. Let.*, (2000).

68. C. Woodward and S.I. Rao, "Ab-initio Simulation of Isolated Screw Dislocations in BCC Mo and Ta," *Phil. Mag.*, A81, pp. 1305, (2001).

69. S.I. Rao, and C. Woodward, "Atomistic Simulations of $a/2<111>$ Screw Dislocations in BCC Mo Using a MGPT Potential," *Phil. Mag.* A81, pp. 1317, (2001).

70. C. Woodward, M. Asta, J. Hafner, and G. Kresse, "Density of Constitutional and Thermal Point Defects in $L1_2$ Al_3Sc ," *Phys. Rev.* B63, 94103 (2001).

71. R. Benedek, A. Alavi, D.N. Seidman, L.H. Yang, D.A. Muller, and C. Woodward, "Electronic Structure of a Model Ceramic-Metal Interface: {222} MgO-Cu," *Phys. Rev. Lett.* 84, pp. 3362 (2000).

72. S. Rao, T.A. Parthasarathy, and C. Woodward, "Atomistic Simulation of Cross-slip Processes in Model FCC Structures," *Phil. Mag.* A79, pp. 1167, (1999).

73. C. Woodward and S.A. Kajihara, "Density of Thermal Vacancies in γ -TiAl-M, M= Si, Cr, Nb, Mo, Ta, or W," *Acta Mater.* 47, pp. 3793 (1999).

74. C. Woodward, S.I. Rao, and D.M. Dimiduk, "Computational Tools for Alloy Design: Solid Solutions in γ -TiAl," *JOM*, 50, No. 7, pp. 37 (1998).

75. C. Woodward, S. Kajihara and L.H. Yang, "Site Preferences and Formations Energies of Substitutional Si, Nb, Mo, Ta and W Solid Solutions in $L10$ TiAl," *Phys. Rev. B* 57, pp. 13459 (1998).

76. S. Rao, C. Hernandez, J.P. Simmons, T.A. Parthasarathy, and C. Woodward, "Green's Function Boundary Conditions in 2-D and 3-D Atomistic Simulations of Dislocations," *Phil. Mag.* A77, pp. 231 (1998).

77. J.P. Simmons, S. Rao, and D. Dimiduk, "Simulation of Kink Properties in γ -TiAl Using Embedded Atom Potentials," *Phil. Mag. Letters*, 77, pp. 327 (1998).

78. J.P. Simmons, S.I. Rao, and D. Dimiduk, "Atomistic Simulations of Structures and Properties of $1/2[110]$ Dislocations Using Three Different Embedded-Atom Method Potentials Fit to γ -TiAl," *Phil Mag.* A75, pp. 1299 (1997).

2.7 PRESENTATIONS

1. D.M. Dimiduk, P.R. Subramanian, and M.G. Mendiratta, "Alloy Selection, Processing, Structure and Mechanical Behavior of Ductile-Phase Toughened Advanced Intermetallic Alloys," to be presented, Oak Ridge National Laboratory, 26 September 1996.

2. P.R. Subramanian, M.G. Mendiratta, and D.M. Dimiduk, "Overview of Research on Nb-base Advanced Intermetallic Alloys," High Temperature Ordered Intermetallic Alloys VII, MRS Fall Meeting, Boston, MA, 5 December 1996.
3. P.R. Subramanian, M.G. Mendiratta, D.M. Dimiduk, and M.A. Stucke, "Overview of Research on Nb-base Advanced Intermetallic Alloys," NASA Lewis Research Center, Cleveland, OH, 24 April 1997.
4. D.M. Dimiduk, P.R. Subramanian, M.G. Mendiratta, and M.A. Stucke, "Advanced Intermetallic Alloys - Beyond Gamma Titanium Aluminides," 4th International Conference on High-Temperature Intermetallics at San Diego, CA, 27 April 1997.
5. P.R. Subramanian, M.G. Mendiratta, and D.M. Dimiduk, "Nb-Base Refractory Metal-Silicide Multiphase Systems," presented at GE-Advanced Intermetallic Blade Contract Kickoff Meeting, 23 November 1998.
6. P.R. Subramanian, M.G. Mendiratta, and D.M. Dimiduk, "Observations and Challenges in Developing Refractory Metal-Silicide Multiphase Systems," presented at US-Japan Workshop on Very High Temperature Structural Materials, Turtle Bay, HI, 9-11 December 1998.
7. M.G. Mendiratta, P.R. Subramanian, T.A. Parthasarathy, and D.M. Dimiduk, "Development of Molybdenum Silicides + Molybdenum Composites for High-Temperature Structural Applications," presented at Symposium on Structural Silicides, TMS Annual Meeting, San Diego, CA, 2 March 1999.
8. P.R. Subramanian, M.G. Mendiratta, and D.M. Dimiduk, "Advances in the Development of High Temperature Nb-Based Intermetallic Systems," presented at Advanced Intermetallics/Refractory Metal Alloys, ASM "AeroMat '99," Dayton, OH, 23 June 1999.
9. M.G. Mendiratta, P.R. Subramanian, and D.M. Dimiduk, "Development of Molybdenum Silicides and Molybdenum Composites for High-Temperature Structural Applications," presented at Advanced Intermetallics/Refractory Metal Alloys, ASM "AeroMat '99," Dayton, OH, 23 June 1999.
10. M.G. Mendiratta, T.A. Parthasarathy, and D.M. Dimiduk, "Overview of Research on Mo-Mo Silicide Composites," 5th International Conference on Structural & Functional Intermetallics, TMS, Vancouver, July 16-19, 2000.
11. Y-W. Kim, "Alpha Forging of Gamma TiAl Alloys," 4th International Conference on High Temperature Intermetallics, San Diego, CA, 27 April-1 May 1997.

12. Y-W. Kim and D. M. Dimiduk, "Deformation and Fracture in Gamma Titanium Aluminide Alloys under Monotonic and Cyclic Loading Conditions," Symposium on Cleavage Fracture: Theory, Experimental, and Modeling, TMS Fall Meeting, Indianapolis, IN, 14-18 September 1997.
13. Y-W. Kim, "Designing Gamma Alloys for Improved Balance in Properties," International Symposium on Ordered Intermetallic Alloys and Composites (IWOIAC-III), organized by D.L. Lin and C.T. Liu, Hangzhou, China, 6-10 April, 1998,
14. Y-W. Kim, "Strength and Ductility in TiAl Alloys," Workshop on High Temperature Intermetallics, Organized by M. Yamaguchi, Kyoto, Japan, 14-16 May 1998.
15. Y-W. Kim, "Current Status and Future of Gamma TiAl Alloys," European TiAl Workshop, organized by M. Loretto, Neuchatel, Switzerland , 7-9 June, 1998.,
16. Y-W. Kim, "Design Fundamentals for Gamma TiAl Alloys," Symp. on Interstitial and Substitutional Solute Effects in Intermetallics II, TMS Fall Meeting, Rosemont, Illinois, 11-15 October 1998.
17. Y-W. Kim, "Gamma TiAl Alloys: Emerging Structural Materials and Future Development," Symp. on Intermetallics for the Third Millennium, ASM International Solutions, Cincinnati, Ohio, 1-4 November 1999.
18. Y-W. Kim, "Application-Specific Wrought Processing for Engineering Gamma Alloys," ASM Ottawa Chapter, Ottawa, Canada, 9 November 1999.
19. Y-W. Kim, "Fatigue Behavior in TiAl Alloys at Elevated Temperatures," Symp. On Structural and Functional Intermetallics, TMS, Vancouver, BC, Canada, 16-20 July 2000.
20. Y-W. Kim and D. M. Dimiduk, "Gamma TiAl Alloys: Emerging Structural Materials and Future Development," Workshop on Advanced Propulsion Materials for IHPTET and Beyond, in Conjunction with IHPTET Symposium, Dayton, Ohio, 11-14 September 2000.
21. P.M. Hazzledine, "Grain Growth and Zener Pinning," Universidad Catolica de Valparaiso, Chile, January 1997.
22. P.M. Hazzledine, "Internal Stresses in Lamellar Ti-Al," TMS Annual Meeting, Orlando, FL February 1997
23. P.M. Hazzledine, "The alpha 2 -> gamma Shear Transformation," TMS Annual Meeting, Orlando, FL, February 1997.
24. P.M. Hazzledine, "Shear Boundaries in Lamellar Ti-Al," The David A. Smith Symposium, TMS, Indianapolis, IN, September 1997.

25. P.M. Hazzledine, "Yield Stress of Fully Lamellar Ti-Al," MRS Fall Meeting, Boston, MA, December 1997
26. P.M. Hazzledine, "Coherency and Loss of Coherency in Multilayers," MRS Fall Meeting, Boston, MA, December 1997.
27. P.M. Hazzledine, "Strength of Nanocrystals and Multilayers," Naval Research Laboratory, Washington, DC, February 1998.
28. P.M. Hazzledine, "The Yield Strength of Semi-Coherent Lamellar Intermetallics," TMS Symposium Strengthening in High Temperature Intermetallics, San Antonio, TX, February 1998.
29. P.M. Hazzledine, "The Influence of Lamellar Statistics on the Hall-Petch Strengthening in Fully Lamellar Ti-Al Alloys," TMS Annual Meeting, San Antonio, TX, February 1998.
30. P.M. Hazzledine, "The Yield Stress of Coherent Cu-Ni," APS March Meeting, Los Angeles, CA, March 1998.
31. P.M. Hazzledine, "Properties of Fully Lamellar Ti-Al alloys," "Strength of Multilayers," and "50th Anniversary of Zener Pinning," Van Horn Lectures, Case Western Reserve University, Cleveland, OH, April 1998.
32. P.M. Hazzledine, "Coherency and Loss of Coherency in Lamellar Ti-Al," Kyoto Workshop on High Temperature Intermetallics, May 1998.
33. P.M. Hazzledine, "Strength of Lamellar Ti-Al," Ohio State University, Columbus, OH, May 1998.
34. P.M. Hazzledine, "Transmission of Twinning and Slip at Lamellar Interfaces in Ti-Al," TMS International Symposium on Advances in Twinning, San Diego, CA, March 1999.
35. P.M. Hazzledine, "The Strength of Coherent Layered Materials," Johns Hopkins University, Baltimore, MD, June 1999.
36. P.M. Hazzledine, "The Strength of Multilayers," McMaster University, Hamilton, ON Canada, October 1999.
37. P.M. Hazzledine, "Ultrastrong Multilayers," Naval Research Laboratory, Washington DC, June 2000.
38. P.M. Hazzledine, "Deformation of Multilayers," Los Alamos National Laboratory, Los Alamos, NM, August 2000.

39. P.M. Hazzledine, "The Jogged Screw Unit Dislocation in Gamma Ti-Al," TMS Symposium Rate Processes in Plastic Deformation II, Fall Meeting, St. Louis, MO, October 2000.
40. C. Woodward and S.I Rao, "Influence of Solid Solutions on Flow Behavior in γ -TiAl," Multi-scale Modeling of Materials, Brown University, Newport, RI, 17 May 2000.
41. C. Woodward, "Dilute Solution Model for Poly-component Alloy Systems," Annual Materials Research Society Meeting, San Francisco, CA, April 2000.
42. C. Woodward and S.I Rao, "First Principles Simulations of Isolated Screw Dislocations in BCC Mo and Ta," Physics H Division, Lawrence Livermore National Laboratory, April 2000.
43. C. Woodward and S.I Rao, "Computation Alloy Design of High Temperature Structural Intermetallics," Materials Design: Computational and Experimental Challenges, Baton Rouge, LA, March 2000.
44. C. Woodward and S.I Rao, "Ab-initio Studies of Dislocations: Core Structures of Screw Dislocations in BCC Metals and Misfit Dislocations at Metal Oxide Interfaces," Physics H Division, Lawrence Livermore National Laboratory, September 1999.
45. S.I Rao and C. Woodward, "a/2<111> Screw Dislocations in BCC Mo: MGPT Atomistic Simulations," Physics H Division, Lawrence Livermore National Laboratory, September 1999.
46. C. Woodward, "Computational Assisted Development of High Temperature Structural Materials," DoD High Performance Modernization Program, 1999 Users Group Conference, Monterey, CA, June 1999.
47. C. Woodward and S.I Rao, "Modeling Solid-Solution Effects in High Temperature Structural Materials," AFOSR Contractor Review Meeting, San Diego, CA, March 1999.
48. S.I Rao and C. Woodward, "Modeling Ordinary Dislocations in γ -TiAl", AFOSR Contractor Review Meeting, San Diego, CA, March 1999.
49. C. Woodward and S.I Rao, "Influence of Solid Solutions on Flow Behavior in γ -TiAl", International Symposium on Gamma TiAl," TMS Meeting, San Diego, CA, March 1999.
50. C. Woodward and S.I Rao, "Modeling Solid-Solution Effects in High Temperature Structural Materials," U.S.-Japan AFOSR Workshop on Very High Temperature Structural Materials, Oahu, HI, December 1998.
51. C. Woodward with E.B. Eberhart and A.F. Giamei, "Charge Redistribution Accompanying Slip and Cleavage: Electronic Structure Calculations in Alloy Design," Annual Materials Research Society Meeting, Boston, MA, December 1998.

52. C. Woodward and S.I Rao, "Influence of Solid Solutions on Flow Behavior in γ -TiAl," Annual TMS Meeting, Rosemont, IL, October, 1998.
53. C. Woodward and S.I Rao, "Influence of Solid Solutions on Flow behavior in γ -TiAl," Annual TMS/ASM meeting, San Antonio, TX, February 1998.
54. C. Woodward, "Computation Alloy Design of High Temperature Structural Intermetallics," Materials and Microsystems for Extreme Environments, Baton Rouge, LA, February 1998.
55. C. Woodward, and S.I Rao, "Chemistry and Intrinsic Flow Behavior of TiAl," Annual Materials Research Society meeting, Boston MA, December 1997.
56. C. Woodward and S.I Rao, "Understanding the Influence of Chemistry on Flow Behavior in TiAl," Computer-Aided Design of High-Temperature Materials, AFOSR workshop, Santa Fe, New Mexico, July 1997.
57. C. Woodward, "Elastic and Point Defect Properties of γ -TiAl," Physics H Division, Lawrence Livermore National Laboratory, February 1997.
58. C. Woodward, "Elastic and Defect Properties of High Temperature Intermetallic Alloys," Complex Systems Theory Branch, Naval Research Laboratory, Washington, DC., February 1996.
59. S.I Rao, "Atomistic Simulation of Dislocation-interface Interactions in the Cu-Ni Multilayer System," TMS, 1998.
60. S.I Rao, "Atomistic Simulation of Cross-slip Processes in $L1_0$ TiAl + Properties of Fully Lamellar Ti-Al Alloys," "Strength of Multilayers," and "50th Anniversary of Zener Pinning," TMS Annual Meeting, 2000.
61. S.I Rao, "Greens Function Boundary Conditions in 2-D and 3-D Atomistic Simulations of Dislocations," Brown University, 2000.
62. S.I Rao, "Atomistic Simulation of Dislocation-Interface Interactions in the Cu-Ni Multilayer System," Los Alamos National Laboratory, 1999.
63. S.I Rao, "Atomistic Simulation of $a/2<111>$ Screw Dislocations in BCC Mo Using a MGPT Potential," Lawrence Livermore National Laboratory, 1999.
64. S.I Rao, "Atomistic Simulations of Dislocation Activation Processes," Lawrence Livermore National Laboratory, 2000.

2.8 INVENTION DISCLOSURE/PATENTS

1. P.R. Subramanian, M.G. Mendiratta, and D.M. Dimiduk, "Method of Making High-Temperature Melting Chromium-Molybdenum-Silicon Alloys," U.S. Patent No. 5,683,524, November 4, 1997.
2. P.R. Subramanian, M.G. Mendiratta, and D.M. Dimiduk, "High Temperature Melting Niobium-Titanium-Chromium-Aluminum-Silicon Alloys," US Letters Patent, Serial Number 08/647,215, Notice of Allowance 3 June 1997.
3. Y-W. Kim and D.M. Dimiduk, U.S. Patent 5,558,729, "Methods to Produce Gamma Titanium Aluminide Articles Having Improved Properties," (Methods to Design Microstructures for Improved Properties in New Gamma Titanium Aluminide Alloys Containing Small Amounts of Tungsten; K5; DP, NL and RFL; HT cycles), September 24, 1996.
4. Y-W. Kim and D. M. Dimiduk, U.S. Patent 5,746,846, "Methods to Produce Gamma Titanium Aluminide Articles Having Improved Properties," (Methods to Design Microstructures for Improved Properties in New Gamma Titanium Aluminide Alloys Containing Small Amounts of Tungsten; K5; DP, NL and RFL; HT cycles), May 5, 1998.
5. Y-W. Kim and D. M. Dimiduk, Invention Disclosure, "Methods to Produce Gamma Titanium Aluminide Articles Having Improved Properties," (Boron refinement for DP, NL, and FL; TMTL, HT cycles), submitted (17 April 1996) and filed (Ser. No. 09/111.258, 30 June 1998) for US Patent.
6. T.A. Parthasarathy, M.G. Mendiratta, and D.M. Dimiduk, "Oxidation Protective Coating for Mo-Si-B Alloys," Patent Filed, No. 09/542,788, AFRL Invention Disclosure (AFD373) - 6 Apr 1999.

2.9 BOOKS CHAPTER

1. Y.Q. Sun and P.M. Hazzledine, "Geometry of Dislocation Glide in the L1₂ γ'-Phase: TEM Observations," in *Dislocations in Solids*, Volume 10 eds F.R.N. Nabarro and M.S. Duesbery, North- Holland, Amsterdam, pp. 28-68, 1996.

2.10 CONFERENCE PROCEEDING EDITED

1. P.R. Subramanian, S. Krishnamurthy, S.T. Keller, and M.G. Mendiratta, "Development of the Matrix-Coated Fiber Process for Fabrication of Continuously Reinforced O-TMCs," in *Orthorhombic Titanium Matrix Composites II*, ed. P.R. Smith, WL-TR-97-4082, Wright-Patterson AFB, OH, pp. 168-195, 1997.

2. S. Krishnamurthy, P.R. Subramanian, and M.G. Mendiratta, "Microstructures and Interstitial Hardening Behavior of a Sputter-Deposited Nb-Ti-Al-Cr Alloy/"Orthorhombic" Ti Aluminide Bimaterial," in *Orthorhombic Titanium Matrix Composites II*, ed. P.R. Smith, WL-TR-97-4082, Wright-Patterson AFB, OH, pp. 289-310, 1997.
3. Y-W. Kim, D. M. Dimiduk and M. Loretto, "Gamma Titanium Aluminides," ed., *TMS*, Warrendale, PA, 1999.
4. International Symposium on Deformation and Microstructure in Intermetallics. TMS Annual Meeting, New Orleans LA, February 11 – 15, 2001. Proceedings edited by Professor S. H. Whang and Dr. P. M. Hazzledine, to appear in *Intermetallics*.
5. "Gamma Titanium Allumindes 1999," eds. Y-W Kim, R. Wagner, and M. Yamaguchi, *TMS*, Pittsburgh PA, 1999.

2.11 AWARDS

1. Y-W Kim, FASM (Fellow of American Society for Metals), 1998
2. Y-W Kim, Served as an invited referee for the Review Meeting for the national programs GKSS Institute (which takes place every four years), GKSS Institute, 30 &31 March, 1998, Geesthacht, Germany.
3. Y-W Kim, Served as the invited reviewer of a EC (European Community) TiAl consortium (1994-1998), COST 513, during the final review meeting, 8 & 9 June, 1998, Neuchatel, Switzerland. The EC official, Mr. Olive Pfaffenzeller, recognized my contribution and asked me to serve as the adviser for them to formulate an application-oriented TiAl consortium.
4. Y-W Kim, Recognized as an "excellent" reviewer for Metallurgical and Materials Transactions by the editor, David E. Lahghlin, 21 August 1998.
5. Y-W Kim, Recognized as an organizer of ISGTA1999 as the most-attended symposium during the 1999 TMS Annual Meeting.
6. Y-W Kim, Selected by EuroMat general chairman as the organizer for Symposium on Intermetallics and Superalloys, EuroMat 2000, Materials Week, 25-28 September 2000, Munich, Germany.
7. P.M. Hazzledine was the Van Horn Distinguished Lecturer, Case Western Reserve University, Cleveland OH, April 1998.
8. P.M. Hazzledine shared with Robert Masumura and Chandra Pande the Naval Research Laboratory's Alan Berman Research Publication Award. (Paper entitled "Yield Stress of Fine Grained Materials," *Acta Materialia*, 46, pp. 4527, 1998.

9. P.M. Hazzledine shared with Victor Berdichevsky and Boris Shoykhet the "Distinguished Paper Award 1999," from the Society of Engineering Science and the International Journal of Engineering Science. Paper entitled "Micromechanics of Diffusion Creep," *Int. J. Engrn. Sci* 35, pp. 1003, 1997.

2.12 REFERENCES

1. Materials Development Research, M.G. Mendiratta, et al., *Final Technical Report*, WL-TR-96-4113, Materials Directorate, Wright Laboratory, AFMC, Wright-Patterson AFB, OH 45433-7734.
2. T.A. Parthasarathy, M.G. Mendiratta, and D.M. Dimiduk, "Mechanisms of Oxidation of Mo-Si-B Alloys," *Acta Mater.*, in review, 2001.
3. Y.H. Wen, L.Q. Chen, P.M. Hazzledine, and Y. Wang, "A Three-Dimensional Phase Field Model for Computer Simulation of Lamellar Structure Formation in γ Ti-Al Intermetallic Alloys", *Acta Materialia*, (2001), In press.
4. P.M. Hazzledine and S.I. Rao, "Yield Stress of Nano- and Micro-Multilayers," in Layered Materials for Structural Applications, eds. J.J. Lewandowski, C.H. Ward, M.R. Jackson, and W.H. Hunt, *MRS*, Pittsburgh, PA, pp. 135-140, 1996.
5. P.M. Hazzledine, "Coherency and Loss of Coherency in Lamellar Ti-Al," *J. Intermetallics*, 6, pp. 673-677, 1998.
6. D.M. Dimiduk, P.M. Hazzledine, T.A. Parthasarathy, S. Sriram, and M.G. Mendiratta, "The Role of Grain Size and Selected Microstructural Parameters in Strengthening Fully-Lamellar Ti-Al Alloys," *Met. Mat. Trans.* 29A, pp. 37-47, 1998.
7. M.A. Grinfeld, P.M. Hazzledine, B. Shoykhet, and D.M. Dimiduk, "Coherency Stresses in Lamellar Ti-Al," *Met. Mat. Trans.* 29A, pp. 937-942, 1998.
8. P.M. Hazzledine and D. M. Dimiduk, "Microstructural Strengthening of Fully Lamellar Ti-Al Alloys," in *Gamma Titanium Aluminides*, eds. Y-W Kim, D.M. Dimiduk, and M.H. Loretto, *TMS*, Warrendale, PA, pp. 481-487, 1999.
9. T.A. Parthasarathy, M.G. Mendiratta, and D.M. Dimiduk, "Observations on the Creep Behavior of Fully Lamellar Polycrystalline TiAl Alloys : Identification of Critical Effects," *Scripta Mater.*, 37 [3], pp. 315-321, 1997 .
10. T.A. Parthasarathy, M. Keller, and M.G. Mendiratta, "The Effect of Lamellar Lath Spacing on the Creep Behavior of Fully Lamellar Ti-47Al," *Scripta Mater.*, 38 [7], pp. 1025-1031,

1998.

11. T.A. Parthasarathy, P.R. Subramanian, M.G. Mendiratta, and D.M. Dimiduk, "Phenomenological Observations of Lamellar Orientation Effects on the Creep Behavior of Ti-48%Al PST Crystals," *Acta Mater.*, 48 [2], pp. 541-551, 2000.
12. T.A. Parthasarathy, M.G. Mendiratta, and D.M. Dimiduk, "Flow Behavior of PST and Fully Lamellar Polycrystals Ti-48Al in the Microstrain Regime," *Acta Mater.*, 46 [11], pp. 4005- 4016, 1998.
13. R.A. Masumura, P.M. Hazzledine and C.S. Pande, "Yield Stress of Fine Grained Materials," *Acta Materialia*, 46, pp. 4527-4534, 1998.
14. Y.Q. Sun, P.M. Hazzledine, and D.M. Dimiduk, "Stress-biased Collective Nucleation of Dislocation Loops," in Phase Transformations and Systems Driven Far from Equilibrium, eds E. Ma, P. Bellon, M. Atzmon and R. Trivedi, *MRS Symposium Proceedings* 481, pp. 261-267, 1998.
15. S.I. Rao and P.M. Hazzledine, "Atomistic Simulations of Dislocation-interface Interactions in the Cu-Ni Multilayer System," *Philos. Mag. A*80, pp. 2011, 2000.
16. B.K. Kad and P.M. Hazzledine, "Monte Carlo Simulations of Grain Growth and Zener Pinning," *Materials Science and Engineering* A238, pp. 70-77, 1997.
17. A. Olguin, M. Oretiz, C.H. Womer, O. Herrera, B.K. Kad, and P.M. Hazzledine, "Zener Pins and Needles," *Philos Mag. B*, 2001, in press.
18. S. Rao, C. Hernandez, J.P. Simmons, T.A. Parthasarathy, and C. Woodward, "Green's Function Boundary Condition in 2-D and 3-D Atomisites Simulations of Dislocation," *Phil. Mag.* A77, pp. 231, 1998.
19. C. Woodward, S. Kajihara, and L.H. Yang, "Site Preference and Formation Energies of Substitutional Si, Nb, Mo, Ta and W Solid Solutions in L10 TiAl," *Phys. Rev. B* 57, 13459, 1998.
20. C. Woodward, Mark Asta, J. Hafner and G. Kresse, "Density of Constitutional and Thermal Point Defects in $L1_2A1_3Sc$," *Phys. Rev.* B63, 94103, 2001.
21. S. Rao and P.M. Hazzledine, "Atomistic Simulation of Dislocation-interface Interactions in the Cu-Ni Multilayer System," *MRS Proceedings*, pp. 578, 389, 2000.
22. S. Rao and P.M. Hazzledine, "Simulation of an Edge Source In the Cu-Ni Multilayer System," *Scripta Materialia*, 41, pp. 1085, 1999.

23. S. Rao and P.M. Hazzledine, "Atomistic Simulation of Tiny Glide Loops in FCC Ni," *Scripta Materialia*, 42, 57, 2000.
24. S.I. Rao and C. Woodward, "Atomistic Simulation of $a/2<111>$ Screw Dislocation in BCC Mo Using a MGPT Potential," *Phil. Mag.* A18, 1317, 2001.
25. S. Rao, "Atomistic Simulation of Cross-slip Processes in Model FCC Structures and $L1_0$ TiAl" *MRS Proceedings*, pp. 538, 77, 1999.
26. S. Rao, "Atomistic Simulation of Cross-slip Processes in $L1_0$ TiAl," accepted for publication in *TMS Proceedings*.
27. S. Sriram, D.M. Dimiduk, P.M. Hazzledine, and V.K. Vasudevan, "The Geometry and Nature of Pinning Points of $1/2<110>$ Unit Dislocation in Binary Ti-Al Alloy," *Philos. Mag.*, 761, pp. 965-993, 1997.
28. S. Sriram, D.M. Dimiduk, and P.M. Hazzledine, "Deformation Substructure Evolution pertaining to $1/2 <110>$ Unit Dislocations in Ti-Al Alloy," in *Structural Intermetallics*, eds. M.V. Nathal, R. Darobia, C.T. Liu, P.L. Martin, D.B. Miracle, R. Wagner, and M. Yamaguchi, TMS Warrendale, PA, pp. 157-166, 1997.

3. TASK II. ADVANCED METALLIC COMPOSITES

3.1 MAJOR FINDINGS

3.1.1 Discontinuously Reinforced Aluminum Composites (DRA)

3.1.1.1 Fracture Toughness Testing of DRA Materials

A number of experiments were performed to ascertain the effect of specimen thickness on the fracture toughness of a powder metallurgy 7093/SiC/15p DRA in different microstructural conditions. The fracture toughness in the under-aged condition was found to increase significantly with decreasing specimen thickness, even at thicknesses well above the value specified by ASTM E-813. The influence of specimen thickness was found to be considerably lower in the peak-aged condition, which was attributed to low strain to failure associated with severe flow localization. In these studies, the effect of precracking on the fracture toughness was also evaluated. The dependence of specimen thickness and precracking were both explained in terms of hydrostatic stress, which has a strong influence on the maximum level of plastic strain that can be sustained in the DRA. Modeling was also carried out, according to the Rice and Tracey model[1], and good agreement between the model and the experimental data was found.

3.1.1.2 Enhanced-Toughness DRA

In this work, two different architectural approaches were used for toughening of DRA materials. One approach was based on exploiting the higher apparent toughness of thin DRA lamina (see Section 1.1.1) to obtain a laminate of higher thickness and toughness. The laminated composite consisted of alternate layers of 7093/SiC/15p DRA plus an unreinforced Al-3003 alloy. Fracture toughness tests in the crack divider configuration showed a toughness improvement of 79 percent in an under-aged condition, and an improvement of 53 percent in a peak-aged condition compared to the monolithic DRA.

Fractographic observations of the primary void size, and its close correspondence with the fracture surface of thin specimens, provided evidence that the individual DRA lamina indeed experienced sufficient loss of constraint in the thickness direction. This was further confirmed by observations of delamination during fast fracture. However, the bond strength was characterized as quite strong. In essence, the work suggested that the laminate was a smart structure, being resistant to failure under normal conditions, but allowing full loss of constraint in the severe stress-strain field ahead of a loaded crack.

In another approach, the effects of adding various sized aluminum particles on the toughness of Al-7093/SiC/15p DRA were studied. The base material was selected to contain 10- μm -sized SiC particles. The remaining DRA materials contained Al particles of different size, volume fraction and composition, that were blended with the DRA, and powder metallurgically processed and extruded. It

was found that the modulus, yield strength and work hardening rates of the materials containing the Al particles were quite insensitive to the distribution of SiC particles. On the other hand, the strain to failure was most strongly influenced by the presence of pure Al and Al-alloy particles, based on local SiC particle volume fraction. Fracture toughness calculations showed that the ASTM E-561 procedure is more appropriate for DRA materials, which exhibit small-scale yielding conditions, than either of the E-318 and E-1152 procedures. The materials containing Al particles also exhibited improved crack growth toughness over the base DRA, and in some cases, the initiation toughness was also increased.

3.1.1.3 Analytical Modeling of Deformation and Fracture in DRA

A significant effort was spent in modeling the deformation and fracture behavior of DRA alloy composites. The material considered was Al-7093/SiC/15p, with approximately 10- μm -diameter SiC particles. The modeling illustrated the following: (1) Angular particles are best represented as unit cylinders. This geometry of particles provides better load transfer characteristics (hence higher Young's modulus) than spherical ones, in line with comparisons between experimental and predicted Young's modulus, and (2) The elastic-plastic model of Bao, Hutchinson and McMeeking [2] is able to provide a good prediction of the stress-strain behavior of these composites.

3.1.1.4 Characterization of Spatial Heterogeneity in DRA

A new, image analysis based multiscalar technique was developed for characterizing the spatial distribution of second-phase particles in two-dimensional distributed multiphase systems. The analysis was called Multi-scalar Analysis of Area Fractions, or MSAAF. The technique was successfully applied to the characterization of reinforcement distributions in two different DRA microstructures, each with different levels of spatial heterogeneity due to different powder processing parameters. A systematic variation in the degree of spatial heterogeneity (as characterized by the coefficient of variation in area fraction) was observed with increasing length scale. This result led to the definition of a parameter L_H , or homogeneous length scale. The relevance of L_H is believed to be in controlling the statistical variation in mechanical properties such as tensile strength, ductility, and fracture toughness, whose controlling mechanisms operate on different length scales in the microstructure. Experiments are currently underway to measure correlations between each of these mechanical properties and the level of spatial heterogeneity in model composite systems.

3.1.2 Fiber-Reinforced Titanium Matrix Composites (TMC)

3.1.2.1 Longitudinal Tension Testing of TMCs

A significant amount of work was carried out to investigate the load-sharing behavior seen in composites loaded in longitudinal tension. Tests were performed at room temperature on specimens from multi-ply and single-ply panels, in order to determine how load-sharing behavior and cumulative fiber fracture was altered by the presence of additional plies. Tensile testing of single-ply specimens revealed that local load sharing was present for all interfacial conditions, independent of whether the normal bond strength was very weak (Trimarc fiber), of medium strength (SCS-6), or if the bond was

of high strength (SCS-0). In addition, cumulative fiber fracture was observed to be dominated by matrix slip between 45 and 60 to the loading axis, rather than being coplanar, as is assumed in all local load-sharing models.

Longitudinal tensile tests of SCS-6/Ti-6Al-4V and Trimarc/Ti-22Al-23Nb specimens indicated that local load sharing was also dominant in the multi-ply panels. However, the fracture plane was perpendicular to the loading direction, rather than being inclined, as was the case with the single-ply specimens. Interestingly, the numbers of broken fibers were less than expected based on local load-sharing arguments, and acoustic emission data taken during the tests suggested that the fiber fractures occurred at the end of the test, rather than in a progressive fashion, with increasing strain.

From the standpoint of interface development, these results suggest that stress concentration effects from broken fiber ends will not play a large role in TMC longitudinal strength performance. Therefore, weakening the interface to prevent stress concentrations at room temperature may have only a small benefit. The real issue in these systems, therefore, becomes the prevention of interphase cracks from reaching the fiber, causing failure even without the presence of other fibers. This requires a low-toughness interphase. This is unfortunate, because interfacial toughness tends to scale with interfacial bond strength, which is one of the requirements for high transverse strength.

3.1.2.2 Transverse Tension Testing of TMCs Using Cruciform Specimen Geometry

A cruciform specimen geometry, developed previously [3, 4], was employed in order to effectively eliminate the influence of the fiber/free surface intersection during the transverse tension testing of fiber-reinforced TMCs. In these studies, extensive transverse tensile testing of single- and multiple-fiber specimens of SCS-6/Ti-6Al-4V composites was performed. The average remote debond stress for well-consolidated, damage-free single-fiber specimens was measured at 322 ± 14 MPa, while a Weibull analysis indicated that the characteristic strength was 328 MPa, with a Weibull modulus of 27. Stress analysis carried out using Finite Element Method (FEM) suggested that at this level of remote stress, the interface supports a tensile stress of approximately 120 MPa, a value much greater than previously thought. Experiments carried out on multiple-fiber specimens yielded very similar results.

In other experiments, measurements were made to ascertain the nature of the failure mechanism at the fiber/matrix interface. It was found that interfacial failure in several carbon/carbon-rich coated SiC/Ti-6Al-4V composites can occur by tangential shear stress before the observed nonlinearity in the experimental stress-strain curve caused by normal interfacial separation. The effect of frictional sliding before normal interface separation on the stress redistribution and stress-strain response of SiC/Ti-6Al-4V composites was examined using FEM. Results indicated that stress redistribution due to tangential shear sliding may significantly modify both interface radial stress distribution and matrix hoop stress. The matrix equivalent stresses, however, are not significantly affected by tangential shear sliding until normal interfacial separation occurs. A methodology was developed for determining the stress concentration factor and the normal bond strength of an interface where tangential shear sliding is occurring. Using this approach, the normal bond strengths for the Trimarc-1/Ti-6Al-4V and the SCS-6/Ti-6Al-4V interfaces

were estimated as 40 MPa and 145 MPa, respectively. These values are significantly higher than those calculated without considering frictional sliding.

3.1.2.3 Creep Behavior of TMCs

Although the cruciform specimen geometry has been identified (using FEM) as suitable for transverse tensile creep experiments in TMCs, the majority of the work in this area was completed using parallel-sided specimens, with embedded fibers designed to remove the stress singularity found where the fibers intersect the specimen edges. Constant load creep tests were carried out on embedded fiber specimens of SCS-6/Ti-6Al-4V, in order to understand how a finite interface bond strength influences the transverse creep behavior. Results indicated that the creep response is consistent with a bond strength of approximately 145 MPa. When the fibers are exposed at the edges, the creep rate increases significantly, indicating that stress singularity and oxidation effects have a large influence on the creep behavior. The results were modeled successfully, using a modified Crossman [5] approach, taking into account the finite interfacial bond strength of the fibers. A range in apparent debond stress was observed, and it was proposed that this is a result of nonuniform fiber spacing in the specimens, and also due to time-dependent relaxation of the thermal residual stresses in the matrix.

3.1.2.4 Fatigue and Interfacial Effects in TMCs

Work was carried out to study the effect of the interface on transverse FCG behavior of TMCs. In general, the results of these FCG tests indicated that independent of bridging, elastic shielding plays a major role on crack deceleration, with a stronger interface usually performing better. The crack deflection data with different interfaces (SCS-6, Trimarc and SCS-0) are broadly consistent with the models of Gupta, Argon and Suo [6]. Thus, interfaces can be designed and optimized simply by using the bond strength as measured from transverse tension testing, and experimental fiber strength values.

In one set of experiments, it was demonstrated that significant improvements in FCG behavior could be achieved by placing a thin stripe of weak interface ahead of the crack tip in composites which otherwise exhibited no fiber bridging behavior. This type of interfacial engineering is called spatially-varied interfacial bonding, or SVIB. In another set of experiments, transverse FCG behavior was also measured in mixed fiber composites, comprising both strongly and weakly bonded fibers in the same fiber ply. Results from these tests gave a simple rule-of- mixtures relationship between the crack growth rates and the proportions of strong and weak fibers.

3.1.2.5 Development of New Fiber Coatings for Optimized Mechanical Properties in TMCs

The purpose of this research project was to develop and characterize new interfaces that provide improved tensile (normal) bond strength, without significant degradation of fiber strength and resistance to FCG. Two new interface systems were studied: (1) titanium-yttrium-titanium (TYT), and (2) SiC fiber sheath.

The TYT system is based on the concept of using a thin Plasma Vapor Deposition (PVD) Ti layer adjacent to the SiC fiber for improved fiber/coating interfacial strength, coupled with a layer of Y to act as a diffusion barrier. An outer Ti layer was added to improve handling and reduce oxidation during processing. However, results from transverse tensile testing using the cruciform specimen geometry and from longitudinal testing using fragmentation techniques showed no significant improvement in composite strength. This was related to oxygen pickup in the Y coating during processing, forming undesirable yttrium oxides which were identified using TEM.

The SiC sheath system is based on the Amercom Trimarc fiber, which has an outer soft/hard/soft C layer which is easily debonded in the presence of a matrix crack. To this is added an additional strong SiC sheath of 5 to 15 μm thickness. The SiC is designed to bond strongly to the matrix to provide good transverse bond strength, while the underlying C layer would act as a weak interface to enhance FCG performance. Although the transverse strengths were measured to be higher than expected, results from single-ply longitudinal tensile tests showed lower strengths than a standard Trimarc composite, due to premature cracking in the SiC sheaths from unknown causes.

Work in both of these experimental coating technologies has been suspended indefinitely until the problems outlined above can be solved.

3.1.3 Fiber-Reinforced Orthorhombic Titanium Matrix Composites (OTMCs)

A significant amount of work was carried out to investigate the effects of heat treatment on the microstructure and mechanical properties of OTMCs. To extract maximum benefit from this new generation of alloys, it was considered important to obtain the desired matrix microstructure, based on an understanding of structure-property relationships. Heat treatment studies were conducted for this purpose, and they provided improvements both in strength and ductility of the OTMCs. It was found that the major problem with this system is C diffusion from the fiber coatings into the matrix during heat treatment. The associated microstructural changes, including stabilization of the alpha-2 phase, required careful adjustment of the heat treatment schedules, and often the required microstructures were simply unobtainable. However, a number of significant findings were made: (1) The B2 phase has wavy slip behavior with dimple fracture characteristics and is an important ingredient for imparting ductility to the matrix, (2) The alpha/alpha-2 grain boundary phases should be avoided, because they are potent cracking sites, (3) the orthorhombic (O) phase is more crack resistant, and is therefore important for high-temperature transverse strength and creep resistance of OTMCs, and (4) interstitial contamination (C and O) from the fiber coating to the matrix must be reduced to increase ductility.

3.2 CURRENT WORK

3.2.1 Discontinuously Reinforced Aluminum (DRA) Composites

3.2.1.1 Effect of Degassing on Mechanical Properties of a DRA Composite

Room-temperature tensile properties of two rods of a PM Al/SiC/20p composite produced from powders blended in air or in vacuum followed by extrusion at 450 °C with 25:1 extrusion ratio were determined. The properties did not depend on the blending conditions: YS = 17.3±0.8 ksi, UTS = 24.4±0.4 ksi, El = 15±1% and RA = 27±2% were the same for both conditions. Distribution and clustering of SiC particles in the extruded samples as well as fracture surfaces of tensile specimens were studied using SEM. No notable difference was found.

3.2.1.2 Microstructural Characterization and Simulation

The MSAAF technique for characterizing spatial heterogeneity in distributed multiphase systems is being extended from two dimensions to three dimensions. It is apparent that certain parallels exist between the two analyses, specifically in the theoretical dependency of coefficient of variation of volume fraction with increasing sampling size for random distributions of second phase particles in two and three dimensions. The theoretical predictions have recently been verified experimentally, using a three dimensional particle placement routine, written in IDL by Soouthern Ohio Council of Higher Education (SOCHE) student researcher Alan Frazier. It is hoped that further 3-D information will be gathered from currently running high-resolution x-ray computed tomography experiments, using Discontinuously Reinforced Copper (DRCu) materials (see section 3.2.2).

3.2.1.3 Effect of Particle Morphology on Mechanical Properties of DRA

Work is currently underway to study the effect of particle morphology on the tensile response and fracture behavior of DRA. Two powder metallurgy Al-6061/SiC/25p materials were fabricated using established powder blending, compaction, and extrusion techniques. One of the materials contained abrasive-grade SiC (F-600), while the second material was fabricated using a more rounded high bulk density (HBD) SiC powder. The mechanical testing of these two materials is yet to be completed. However, initial results are very encouraging and strongly suggest that the HBD specimens show increased tensile ductility up to 40 % higher than the F-600 materials with negligible decrease in strength and elastic modulus. SEM fractography results also suggest a transition from a brittle failure mode in the F-600 material to a more ductile failure mode, with increased dimpling of the fracture surface, in the HBD material. The ability to increase the specific modulus of these DRA materials by increasing the SiC content without significantly reducing the ductility is seen as enabling for many AF applications where high structural efficiency is key.

3.2.2 Discontinuously Reinforced Copper (DRCu) Composites

Under the LDF task, "Controlled-Microstructure Powder Metallurgy Discontinuously Reinforced Metallic (PM-DRX) Composites Via Coating of Reinforcement" (J.E. Spowart, P.I.), SiC powders were coated with metallic copper and direct powder forged (Ceracon, Inc.) into a fully dense billet. This material is currently undergoing microstructural and thermal property evaluation. Additional material was prepared at the Materials Laboratory (ML) using Hot Isostatic Process (HIP), both from the MCP precursor and via a conventional route, using a blend of SiC and Cu powders. The HIP'ed material is currently undergoing high-resolution x-ray computed tomography measurements (NRL) in order to extract 3-D microstructural information. This work complements the ongoing effort on microstructural characterization and simulation.

3.2.3 Amorphous Aluminum

3.2.3.1 Crystallization Kinetics of an Amorphous Al-based Alloy

$\text{Al}_{85}\text{Ni}_{10}\text{Y}_{2.5}\text{La}_{2.5}$ alloy powder produced by gas atomization was sieved into three grades with particle sizes –500 mesh, -325/+500 mesh, and –200/+325 mesh, and the phase composition of the each grade was determined. The –500 mesh powder was almost fully amorphous, the powder of –200/+325 mesh size was fully crystalline, and the intermediate grade powder was only partially amorphous.

Crystallization kinetics of the amorphous phase were studied in the –500 mesh powder (particle size $\leq 23 \mu\text{m}$) using DTA, XRD, and SEM. Crystallization occurred in the temperature range 230 °C to 450 °C in three steps by exothermic reactions. The activation energies of the mechanisms responsible for the three steps of the crystallization were determined as 148 kJ/mol, 336 kJ/mol, and 274 kJ/mol, respectively. XRD and SEM analysis of the powder heated to different temperatures showed that precipitation of Al-based particles occurred during the first exothermic reaction, crystallization of the Al_4La phase and an increase in the volume fraction of the Al-based phase took place during the second exothermic reaction, and development of the Al_3Ni phase occurred during the third exothermic reaction. After annealing at 550 °C, the powder consisted of Al-based matrix reinforced with very fine intermetallic particles of different morphologies.

3.2.3.2 Compaction of an Amorphous Powder

Possibility of compaction of an amorphous powder at moderate temperatures (below the crystallization temperature) using equal channel angular pressing (ECAP) was evaluated. The powder was cold compacted and ECAP processed at 290 °C. Although some regions were fully consolidated, the compacted material was highly porous. The microstructure of the compact has been studied using SEM and TEM. The work is in progress.

3.2.3.3 Topology-Based Structural Models for Amorphous Metals

An atomic structural model for amorphous Al alloys was explored and proposed. This model provides description of likely local atomic configurations and is consistent with experimental observations. An

analysis of atomic size distributions in ordinary and bulk amorphous alloys was performed. Ordinary amorphous alloys, which have a high critical cooling rate, were found to have single-peak distributions, with concave downward shape. These amorphous alloys have at least one alloying element with a smaller atomic radius and at least one alloying element with a larger radius relative to the base element. The concentration of an alloying element decreases rapidly as the difference in the atomic sizes of the base element and alloying element increases. Atomic size distributions of currently known bulk amorphous alloys based on Zr, Pd, or Ln, have completely different, concave upward shape with a minimum at an intermediate atomic size. The base alloying element in these alloys has the largest atomic size and the smallest atom often has the next-highest concentration. A topological model for glass formation that explains a concave upward shape of atomic size distributions for the bulk amorphous alloys has been developed. This model recognizes that all alloying elements in bulk glass formers are smaller than the matrix element. A critical feature of this model is that alloying element can occupy either substitutional or interstitial sites, or both, depending upon their atomic radius relative to the solvent atom. Further, elements may partition between these two sites and the relative site frequency is a function of the free energy increase associated with each site. According to this model, the critical concentration of a solute element required to destabilize the crystalline lattice decreases, reaches a minimum and then increases when the difference between atomic sizes of the solute and matrix elements increases.

3.3 PUBLICATIONS

1. S.G. Warrier, D.B. Gundel, B.S. Majumdar, and D.B. Miracle, "Stress Distribution in a Transversely Loaded Cross-Shaped Single Fiber SCS-6/Ti-6Al-4V Composite," *Scripta Mater.*, 34, pp. 293-299 (1996).
2. S.G. Warrier, D.B. Gundel, B.S. Majumdar, and D.B. Miracle, "Interface Effects on the Micromechanical Response of a Transversely Loaded Single Fiber SCS-6/Ti-6Al-4V Composite," *Metall. and Mater. Trans.*, 27A, pp. 2035-2043 (1996).
3. S.G. Warrier, B.S. Majumdar, and D.B. Miracle, "Determination of the Interface Failure Mechanism During Transverse Loading of Single Fiber SiC/Ti-6Al-4V Composites From Torsion Tests," *Acta Materialia*, 45(1), pp. 309-320 (1997).
4. D.B. Gundel, S.G. Warrier, and D.B. Miracle, "The Interface Debond Stress in Single and Multiple SiC Fiber/Ti-6Al-4V Composites under Transverse Tension," *Acta Materialia*, 45, pp. 1275-1284 (1997).
5. F. Chu, T.E. Mitchell, B.S. Majumdar, D.B. Miracle, T.K. Nandy, and D. Banerjee, "Elastic Properties of the O-Phase in Ti-Al-Nb Alloys," *Intermetallics*, 5, pp. 147-156 (1997).
6. B.S. Majumdar, T.E. Matikas, and D.B. Miracle, "Effects of the Interface on Local vs Global Load Sharing Behavior in Metal Matrix Composites Under Longitudinal Tension," *Proc. 11th International Conference on Composite Materials, Vol. III*, (ed. M.L. Scott), Woodhead Publishing, Abington, UK, pp. 238-249 (1997).

7. S.G. Warrier, B.S. Majumdar, and D.B. Miracle, "Effect of the Interface on Crack Deflection and Fiber Bridging During Fatigue Crack Growth of SiC/Ti-6Al-4V Composites," *Proc. 11th International Conference on Composite Materials, Vol. III*, (ed. M.L. Scott), Woodhead Publishing, Abington, UK, pp. 374–383 (1997).
8. C.J. Boehlert, B.S. Majumdar, S. Krishnamurthy, and D.B. Miracle, "Role of Matrix Microstructure on RT Tensile Properties and Fiber-Strength Utilization of an Orthorhombic Ti-alloy Based Composite," *Metall. and Mater. Trans.*, 28A, pp. 309–323 (1997).
9. S.G. Warrier and B.S. Majumdar, "Effects of the Interface on the Fatigue Crack Growth Response of Titanium Matrix Composites: Modeling and Impact on Interface Design," *Mat. Sci. Eng.*, A237, pp. 256-267 (1997).
10. S.G. Warrier, B.S. Majumdar, D.B. Gundel, and D.B. Miracle, "Implications of Tangential Shear Stress Induced Failure During Transverse Loading of SiC/Ti-6Al-4V Composites," *Acta Materialia*, 45(8), pp. 3469–3480 (1997).
11. S.G. Warrier, B.S. Majumdar, and D.B. Miracle, "Interface Effects on Crack Deflection and Fiber Bridging During Fatigue Crack Growth in Titanium Matrix Composites," *Acta Mater.* 45, 12, pp. 4969-4980 (1997).
12. B.S. Majumdar and D.B. Miracle, "Interface Measurements and Applications in Fiber-Reinforced MMCs," *Key Engineering Materials*, 116-117, pp. 153-172 (1996).
13. S.G. Warrier, B.S. Majumdar, and D.B. Miracle; "Interface Effects on Crack Deflection and Bridging During Fatigue Crack Growth of Titanium Matrix Composites," *Acta Materialia*, 45(12), pp. 4969–4980 (1997).
14. A.B. Pandey, B.S. Majumdar and D.B. Miracle, "Effects of Thickness and Precracking on the Fracture Toughness of Particle-Reinforced Al-Alloy Composites," *Metall. Mater. Trans. A*, 29A, pp. 1237-1243 (1998).
15. B.S. Majumdar, T.E. Matikas, and D.B. Miracle, "Experiments and Analysis of Fiber Fragmentation in Single and Multiple Fiber SiC/Ti-6Al-4V Metal Matrix Composites," *J. of Compos. B*, 29B, pp. 131-145 (1998).
16. S.G. Warrier, B. Maruyama, B.S. Majumdar, and D.B. Miracle, "Behavior of Several Interfaces During Fatigue Crack Growth in SiC/Ti-6Al-4V Composites", *Mat. Sci. Eng.*, A259, pp. 189-200 (1999).
17. A.B. Pandey, B.S. Majumdar, and D.B. Miracle, "Effect of aluminum particles on the fracture toughness of a 7093/SiC/15p composite," *Mat. Sci. Eng.*, A259, pp. 296-307 (1999).
18. D.B. Miracle and B.S. Majumdar, "Transverse Creep of SiC/Ti-6Al-4V Fiber-Reinforced MMC's," *Metall. Mater. Trans. A*, 30A, pp. 301-306 (1999).

19. C.J. Boehlert, B.S. Majumdar, V. Seetharaman, and D.B. Miracle, "Part I. The Microstructural Evolution in Ti-Al-Nb O + Bcc Orthorhombic Alloys," *Metall. Mater. Trans. A*, 30A, pp. 2305–2323 (1999).
20. A.B. Pandey, B.S. Majumdar, and D.B. Miracle, "Deformation and Fracture of a Particle-Reinforced Aluminum Alloy Composite: Part I. Experiments," *Metall. Mater. Trans.*, 31A, pp. 921-936 (2000).
21. D.B. Gundel, S.G. Warrier, and D.B. Miracle, "The Transverse Tensile Behavior of SiC Fiber/Ti-6Al-4V Composites: Part 2 - Stress Distribution and Interface Failure," *Compos. Sci. Tech.*, 59, pp. 1087-1096 (1999).
22. S.G. Warrier, D.B. Gundel, and D.B. Miracle, "Numerical Modeling of Interface Failure in a Transversely Loaded Single Fiber SiC/Ti-6Al-4V Composites," *Acta Materialia*, Submitted for publication.
23. C.J. Boehlert, B.S. Majumdar and D.B. Miracle, "Transverse Tensile Examination of a Sigma 1240/Ti-6Al-2Sn-4Zr-2Mo Composite", Submitted to Materials Science and Engineering
24. A.B. Pandey, B.S. Majumdar, and D.B. Miracle, "Laminated Particulate-Reinforced Aluminum Composites with Improved Toughness," *Acta Mater.*, Submitted for Publication.
25. O.N. Senkov and D.B. Miracle, "Effect of the Atomic Size Distribution on Glass Forming Ability of Amorphous Metallic Alloys," *Materials Research Bulletin*, 2001 (submitted).
26. D.B. Miracle and O.N. Senkov, "The Atomic Structure of Some Amorphous Metals," *Acta Materialia*, 2001 (submitted).
27. O.N. Senkov and D.B. Miracle, "Topological Criterion for Metallic Glass Formation," *Acta Materialia*, 2001 (to be submitted).
28. O.N. Senkov, J.M. Scott, K.L. Kendig, and D.B. Miracle, "Crystallization Kinetics of an Amorphous Al₈₅Ni₁₀Y_{2.5}La_{2.5} Alloy," *Pacific Rim International Conference on Advanced Materials and Processing, Proceedings*, 2001 (submitted).
29. J.E. Spowart, B. Maruyama, and D.B. Miracle, "Multi-Scale Characterization of Spatially Heterogeneous Systems: Implications for Discontinuously-Reinforced Metal-Matrix Composite Microstructures," *Mat. Sci. Eng.*, A307 (1-2), pp. 51-66 (2001).
30. J.E. Spowart, B. Maruyama, A. Frazier, and D.B. Miracle, "Multi-Scale Characterization of Spatially Heterogeneous Microstructures: Extension to Three Dimensions," *Mat. Sci. Eng.*, 2001 (to be submitted).

31. J.E. Spowart, and B. Maruyama, "Improved Multi-Functional Materials for Space-Based Thermal Management," *Proceedings of the 2001 National Space and Missiles Materials Symposium (Session 4: Operating in Space)*, (accepted for publication, 3/01).
32. J.E. Spowart, "Effect of Reinforcement Particle Morphology on the Tensile Response of 6061/SiC/20p Discontinuously-Reinforced Aluminum", Proceedings of the 2001 International Congress on Fracture - ICF-10, (accepted for publication 5/01).

INVENTION DISCLOSURE/PATENTS

1. O.N. Senkov, M.G. Mendirata, and D.B. Miracle, Method of Powder Compaction and Production of Near-net Shape Parts from Powders, AF Inv. D494, November 2000.
2. O.N. Senkov, M.G. Mendirata, and D.B. Miracle, Method of Semi-Solid Forming with the Use of Equal Channel Angular Pressing, AF Inv. D495, November 2000.

3.5 BOOKS

1. B.S. Majumdar, "Fiber-Matrix Interface," in *Titanium Matrix Composites*, (eds. S. Mall and T. Nicholas) Technomic Publications, pp. 113-167 (1997).
2. A.B. Pandey, B.S. Majumdar, and D.B. Miracle, "The Fracture Behavior of SiC_p/Aluminum Alloy Composites With and Without Large Al-Particles," in *Layered Materials for Structural Applications* (eds. J.J. Lewandowski, C.H. Ward, M.R. Jackson, and W.H. Hunt, Jr.), MRS Proceedings, 434, Pittsburgh, PA, pp. 249-254 (1996).
3. D.B. Miracle, D.B. Gundel, and S. Warrier, "Interfacial Structure and Properties for the Design of Fiber-Reinforced Metal Matrix Composites," in *Processing and Design Issues in High Temperature Materials* (eds. N.S. Stoloff and R.H. Jones), TMS, Warrendale, PA, pp. 277-286 (1996).
4. C.J. Boehlert, B.S. Majumdar, V. Seetharaman, D.B. Miracle, and R. Wheeler; "Phase Evolution, Stability, and Microstructure-Creep Relations in an Orthorhombic Ti-23Al-27Nb Alloy", *Structural Intermetallics 1997* (eds. M.V. Nathal, R. Darolia, C.T. Liu, P.L. Martin, D.B. Miracle, R. Wagner, and M. Yamaguchi), TMS, Warrendale, PA pp. 795-804 (1997).
5. B.S. Majumdar, S.G. Warrier, and D.B. Miracle, "Interface Effects on the Tensile and FCG Behavior of Fiber-Reinforced Metal Matrix Composites," in *Interfacial Engineering for Optimized Properties*, (eds. C.L. Briant, C.B. Carter, and E.L. Hall), MRS Proceedings Vol. 458, Pittsburgh, PA, pp. 185-190 (1997).

3.6 AWARDS

1. An Air Force SBIR Phase I Proposal: "Advanced Aluminum Materials for Rocket Turbopump Rotors" (O. Senkov, P.I.), submitted in January 2001 and selected for funding in May 2001.

2. An LDF Proposal "Controlled-Microstructure Powder Metallurgy Discontinuously-Reinforced Metallic (PM-DRX) Composites Via Coating of Reinforcement" (J.E. Spowart, P.I.) was selected for funding in FY'00 and FY'01.

3.7 REFERENCES

1. J.R. Rice, D.M. Tracey, *J. Mech. Phys. Solids*, 17 1969 201.
2. G. Bao, J.W. Hutchinson, and R.M. McMeeking, *Acta. Metall. Mater.* 39 1991 1871.
3. D.B. Gundel, B.S. Majumdar, and D.B. Miracle, *Scripta Materialia* 33 1995 2057.
4. D.B. Gundel, B.S. Majumdar, and D.B. Miracle, "The Intrinsic Transverse Response of Several SiC/Ti-6Al-4V Composites to Transverse Tension," in: A. Poursartip, K. Street (eds.), *Proc. of ICCM-10, Vol. 2*, Woodhead Publishing, Vancouver, Canada, 1995, p. 703.
5. F.W. Crossman, and R.F. Karlak, Creep of B/Al Composites as Influenced by Residual Stresses, Bond Strength, and Fiber Packing Geometry, in: J.N. Fleck, R.L. Mehan (eds.), *Failure Modes in Composites II: Proceedings of the 6th Annual Spring Meeting of The Metallurgical Society of the AIME*, TMS, New York, NY, 1974, p. 8.
6. V. Gupta, A.S. Argon, and Z. Suo, *Journal of Applied Mechanics*, 59 1992 S79.

SECTION 4. TASK III. CERAMIC COMPOSITES

As part of the 1996-2000 on-site contract (U.S. Air Force Contract #F33615-96-C-5258) with AFRL, UES, Inc. proposed to work towards the enhancement of the oxidation resistance of continuous fiber reinforced ceramic matrix composites (CMC), thereby retaining their damage tolerance. It was proposed that, in close collaboration with AFRL personnel, we explore oxidation-resistant interface concepts, establish a fiber (tow) coating methodology for selected coatings, establish and use a protocol to evaluate the effectiveness of such approaches, analyze (theoretically and experimentally) the mechanics of minicomposites and macrocomposites, and through such procedures/tasks identify promising oxide-oxide composite systems. We (UES, Inc.) in collaboration with government engineers in the Ceramics group (MLLN) and in the Mechanics branch (MLBP) have successfully completed these tasks and have identified two approaches that are most promising for further research. The two approaches involve using interlayers of either monazite (LaPO_4) or porous oxides ($\text{ZrO}_2\text{-SiO}_2$, ZrO_2 , YAG) between the fiber and matrix. This assessment was arrived at gradually through processing trials and advances, establishing thermomechanical stability, fiber push-out techniques and models, processing and testing of microcomposites and minicomposites, extensive SEM/TEM analysis, mechanics modeling, development of mechanistic understanding of fiber strength degradation, and clever process improvements.

In the case of monazite interlayers, coated Nextel™ 720 and Nextel™ 610 fibers embedded in matrices of alumina were shown to retain much of their fiber strengths in composites after long periods (100 hours) of exposure at temperatures as high as 1200 °C, significantly better than the control (coatingless) composites. Among the porous oxides tested, YAG is the most refractory and resistant to pore coarsening. The promise of porous YAG coatings on Nextel™ 610 fibers has been inferred from minicomposite testing, a protocol established as part of our on-site program. This test also showed that the porous YAG densified after long-term (100 h) exposures at 1200 °C; this makes it necessary to determine the use limits of these coatings and identify more refractory oxides for use at 1200 °C and above. Finally, we have started a collaborative research effort with the propulsion directorate on designing oxide-oxide ceramic composites for a very specific application in a combustion chamber. Thus from the efforts of the prior contract, we have identified monazite (in general, Xenotimes) and refractory porous oxides as the most promising interlayers for oxide-oxide composites. The following is a concise report giving details of the activities performed during this contract.

4.1 SUMMARY OF MAJOR FINDINGS

In this section we give a summary of each of the projects undertaken and completed (by reporting in recognized journals). Further details can be found in the publications cited. A list of the cited publications (all resulting from this contract) is given in Section 4.3 in chronological order.

4.1.1 Interface Control

4.1.1.1 Easy Cleaving Oxides: Hexaluminates

Calcium hexaluminate ($\text{CaAl}_{12}\text{O}_{19}$, hibonite) was used to produce highly textured fiber coatings and interphases in single-crystal alumina fiber-based ceramic matrix composites. Cracks were shown to deflect and propagate within the interphase by cleavage. Critical strain-energy release rates of 2.2 J/m^2 were measured for highly textured polycrystalline $\text{CaAl}_{12}\text{O}_{19}$ interphases [11, 13, 39]. An interesting outcome of this work was the invention of a method to form tubular inclusions of hexaluminates in sapphire [22]. The reactions between hot-pressed calcium hexaluminate and silicon carbide (SiC) at 1100°C to 1400°C in air and nominal argon atmospheres were also investigated. In inert atmospheres, there was no evidence of reaction at temperatures up to at least 1400°C . In air, the oxidation of SiC, produced a layer of silica or a multicomponent amorphous silicate (depending on impurities) that reacted with $\text{CaAl}_{12}\text{O}_{19}$. Below 1300°C , the reaction resulted in the stratification of two distinct interfacial layers; one was a partially devitrified $\text{CaO-Al}_2\text{O}_3-\text{SiO}_2$ glass adjacent to SiC, and the other was a $\text{CaAl}_2\text{Si}_2\text{O}_8$ (anorthite) layer adjacent to hibonite. At 1400°C , a large amount of liquid was formed, the majority of which was squeezed out from between the couple. No distinct layer of anorthite was present but was replaced by a layer of alumina between the glass-rich layer and hibonite. An activation energy of 290 kJ/mol was determined for the reaction, which is consistent with oxygen diffusion through a calcium aluminosilicate glass. The reaction between rare-earth hexaluminates and SiO_2 was predicted to produce a more viscous glass than $\text{CaAl}_{12}\text{O}_{19}$ and SiO_2 and, therefore, have slower reaction kinetics due to lower mass transport in the glass [12].

Subsequent work focused on lowering the temperature for synthesis and texturing of both calcium- and lanthanum-based hexaluminates. Doping of hexaluminates, primarily with transition-metal oxides, allows for their formation at temperatures as low as 1000°C . Grain-growth rates are about an order of magnitude greater than for undoped powders. Textured coatings have been grown on single-crystal YAG plates at 1200°C . However, there does not seem to be an adequate driving force for grain growth and texturing of the coatings on polycrystalline alumina fibers (Nextel™ 610) at 1200°C , the maximum processing temperature for these fibers. The lack of a more refractory, commercially available fiber that is phase compatible with the hexaluminates currently limits further development of a hexaluminate fiber-matrix interphase [14, 56].

4.1.1.2 Weakly Bonded Interface: Monazite

Monazite (LaPO_4) is under consideration as an oxidation-resistant fiber-matrix interface in CMCs in place of oxidation-prone carbon or boron nitride (BN). Liquid phase precursors and CVD have been used to coat fiber tows with monazite. A major problem with monazite fiber coatings is fiber strength degradation after coating and after long-term, high-temperature heat treatments. The work reported here focused on experiments designed to find a monazite Sol precursor that preserves fiber strength. Monazite coatings were initially deposited on sapphire filaments, followed by coatings on Nextel™ 720, 610 and SiC fibers using various monazite

precursors. Prior to coating the fiber, the monazite precursors' viscosities, densities, and concentrations were measured. The resultant solids were characterized by DTA/TGA, X-ray and mass spectrometry. The coatings were characterized for thickness, microstructure, and composition by optical microscopy, SEM, and TEM. Coated-fiber tensile strengths were measured by single filament tensile tests.

4.1.1.2.1 Coatings on Sapphire Monofilaments

Various routes to synthesize monazite sols were explored. Sapphire fibers were dip coated and cured at 700 ° to 1100 °C. The coating thickness varied from 60 to 150 nm and was found to depend on the monazite sol concentration and the number of coats. X-ray diffraction of the coated fibers showed the formation of monazite above 700 °C [3].

4.1.1.2.2 Coatings on Nextel™ 720 and 610 Fiber Tows

Seven different aqueous or ethanolic precursors were used to continuously coat monazite (LaPO_4) on Nextel™ 720 fiber tows. The coatings were cured in-line at temperatures of 1200 ° to 1400 °C and at a rate of $1.4 \text{ cm}^2\text{sec}^{-1}$. Fibers were continuously coated when precursors with $> 40 \text{ g/l}$ monazite yield and $< 2 \text{ mPa}\cdot\text{sec}$ viscosity were used. Coating bridges between filaments and crust around the tow perimeter were more abundant for more viscous precursors. Cracking in thinner coatings was uncommon, despite high heating, and cooling rates. Median coating thickness was typically 50 to 100 nm for precursors with 40 to 80 g/l monazite yield. Coating thicknesses fit a log-normal distribution, which was bimodal when the crust around the tow perimeter was abundant. Median coating thicknesses were nearly two orders of magnitude greater than those predicted for monofilaments. Therefore, filaments in a tow entrained much thicker liquid layers than monofilaments of the same diameter. There were significant thickness variations from filament to filament, but usually little variation in composition or microstructure. Amorphous AlPO_4 layers formed from phosphate rich precursors. Coated-fiber tensile strengths were from 25 to > 50 percent lower than those of the as-received fiber. Tensile strengths were not dependent on coating thickness and did not depend on precursor stoichiometry. A strong dependence of the tensile strength on the precursor used suggests great sensitivity to the chemical environment during coating [3, 21, 27].

4.1.1.2.3 Effect of Process Variables on Coated-Fiber Tensile Strength

Monazite made from diammonium-hydrogen phosphate and lanthanum nitrate was coated on Nextel™ 720 fibers. The coatings were phosphorus rich and were heat-treated in-line at 900 ° to 1300 °C. Some experiments were repeated with alumina-doped precursors. Coated fibers were heat-treated for 100 hours at 1200 °C. Coated-fiber tensile strength was lower for fibers coated at higher deposition temperatures. Heat treatments for 100 hours at 1200 °C reduced tensile strength further. Fibers with alumina-doped coatings had higher tensile strengths than fibers with undoped coatings after heat treatment for 100 hours at 1200 °C. Alumina added as α -alumina particles gave higher strengths than alumina added as colloidal boehmite. Both P-rich and La-rich monazite coatings enhanced alumina grain growth at the surface of Nextel™ 720. However, there was no correlation between grain growth and coated-fiber strength. AlPO_4 forms

rapidly from P-rich monazite but does not degrade fiber strength, and may slightly improve it. The addition of alumina to a slightly phosphate-rich monazite coating probably promotes the formation of AlPO₄ within the coating rather than at the coating-fiber interface, but this also had no obvious effect on fiber strength. It is possible that lanthanum magnetoplumbite monolayers, of sufficient size to be strength limiting flaws, may form along grain boundaries after long-term heat treatment at 1200 °C. If this is true, fiber strength should scale with 1/ $\sqrt{}$ grain size, but this was not observed. Alumina doping retarded monazite grain growth, and formed rough fiber-coating interfaces after 100 hour heat treatments at 1200 °C. Most observations and analysis are inconsistent with degradation by solid-state reaction between coating and fiber. The beneficial effect of alumina doping is tentatively attributed to scavenging surface active species. However, fibers with alumina-doped coatings, made with an in-line heat treatment of 1300 °C, displayed inferior strengths; this fact is currently unexplained [48].

4.1.1.2.4 Monazite Coating without Fiber Strength Degradation

A washed and unwashed rhabdophane (LaPO₄.xH₂O) sol was used to apply monazite coatings on Nextel™ 720 and 610 fibers. The colloidal rhabdophane sol was precipitated from lanthanum nitrate and phosphoric acid. The sol was characterized with light scattering and zeta-potential measurements. The rhabdophane sol was washed by centrifugal separation of the particles from nitric acid and redispersed in deionized water. The washing process minimizes stress corrosion from gaseous decomposition products at high temperature. TGA and pH measurements showed that the washed sol had a higher pH and lower weight loss than the unwashed sol. The as-coated fibers were tensile tested along with coated fibers heat treated in air at 1200 °C for 100 hours. Coatings with the washed sol did not degrade fiber strength when applied at or below 1200 °C. The lack of strength degradation correlated with the low precursor weight loss of the washed sol. This will allow fibers to be coated multiple times, building thicker coatings without strength degradation. Coatings thicker than 1 μm tended to crack off, probably from Coefficient of Thermal Expansion (CTE) mismatch. Furthermore, fibers coated with the washed sol and heat treated for 100 hours at 1200 °C were stronger than uncoated fibers given the same heat treatment. A comparison of coated fiber strength to coating precursor weight loss for a variety of precursors and temperatures shows a strong correlation between low precursor weight loss and high coated-fiber strength. Filament strengths were also retained after Nextel™ 610, Tyranno™-SA, Hi-Nicalon™, Hi-Nicalon-S™ and Sylramic™ fibers were coated with the washed monazite sol. This observation and others are consistent with a strength degradation mechanism of stress corrosion by surface-active decomposition products from the coating precursor [27, 43, 44, 46].

4.1.1.3 Fugitive Coatings

Carbon coatings on Nextel™ 550 and 720 fibers were studied in batch (furnace) and continuous (solution fiber coating apparatus) modes, and in an inert atmosphere. Ashland Aerocarb™ 240 pitch in toluene was used as the precursor material for the carbon coatings. The effect of processing variables (i.e., pitch concentration, Nextel™ fiber sizing, and oxidative curing) was studied. Characterization was done by tactile evaluation, SEM, and TGA/DTA. Coating adherence, thickness, and uniformity were investigated. Applied carbon coatings adhered well onto the filaments; however, the thickness and uniformity of the carbon coatings were poor, mainly because of melting and wicking of the pitch inside the tow prior to pyrolysis [1]. Further

work on fugitive carbon coatings (Section 4.1.4.1) was completed using commercially applied CVD carbon coatings (Synterials, Inc.).

4.1.1.4 Porous Coatings

A porous oxide may be a functional and oxidative-resistant interface, as the inherent weakness of porous materials is well known. Porous oxide coatings can be made from homogeneous carbon-oxide mixtures. The carbon is a fugitive phase that holds and prevents densification of the coating during matrix processing under nonoxidizing conditions. After matrix processing, the carbon can be oxidized, leaving a porous oxide fiber-matrix interface. A problem encountered in making homogeneous carbon/oxide mixtures is the prevention of phase segregation. During in-line curing of the coatings on fiber tows, the interior solvent is carried to the fiber surface by capillary forces. When the coating sol contains two solutes, e.g., a carbon and an oxide precursor, the solutes may be carried to the fiber surface at different rates during drying, causing segregation. In this work, we show a potential solution of solving the segregation problem by bonding the carbon and oxide precursors via electrosteric interactions, e.g., zircon/carbon, or by forming a complex between the carbon and oxide precursor, e.g., carbon/rare earth oxides.

4.1.1.4.1 Porous ZrO₂-SiO₂

Zircon (ZrSiO_4) is a refractory oxide with a coefficient of thermal expansion of $4.3 \times 10^{-6}/^\circ\text{C}$ and density of 4.7 g/cc. Zircon is expected to resist sintering and pore coarsening because of low diffusion rates. Except for hydrofluoric acid, it is chemically resistant to organic and inorganic acids. It decomposes to silica and zirconia at ~1600 to 1700 °C. In the presence of impurities that react with silica, such as water, the decomposition temperature is lower. Thermodynamic calculations show zircon to be compatible with carbon at a temperature of 1527 °C. It is stable with alumina, mullite, silica, and SiC. The pore coarsening resistance, corrosion resistance, thermochemical and thermoelectric compatibility with other common structural ceramics make zircon an attractive candidate for a porous fiber-matrix interface.

Zircon was synthesized by hydrolysis of zirconyl nitrate hydrate (ZN) and tetraethoxysilane (TEOS) in ethanol. Zircon was also made by hydrolysis of zirconium ethoxide (ZEOS) and TEOS in ethanol. Polyacrylic acid (PA) was added as the carbon precursor. Ammonium vanadate and lithium nitrate were added to decrease the zircon formation temperature. Powders from these precursors were characterized by x-ray diffraction, thermogravimetric analysis (TGA) and DTA. Zircon did not form when the zircon-carbon precursors composed of ZN, TEOs, ammonium vanadate, and PA or ZEOS, TEOs, and PA were heat treated in argon at temperatures of 1200 to 1400 °C. Zircon did form when the precursors were heat treated in air as low as 1000 °C. Ammonium vanadate was an effective mineralizer when the heat treatment was done in air, but ineffective in argon. Preheating of the sol precursor in air at 300 to 400° C was found to enhance zircon formation. The relative percent of zircon formed increased as the preheat temperature was increased. But the relative percent of carbon in the zircon-carbon mixtures decreased as the preheat temperature increased, indicating that the formation of zircon in an inert atmosphere is hindered by carbon. TEM and X-ray analysis of coated Nextel™ 720 fiber show the coatings to be a mixture of tetragonal zirconia-silica dispersed in carbon. Preheating of the

coated fibers prior to curing in argon at temperatures greater than 1200 °C enhanced the formation of zircon-carbon phases [26, 32].

4.1.1.4.2 Porous Rare-Earth Aluminate Fiber Coatings

Several types of porous rare-earth aluminate coatings were developed and examined for use in oxide-oxide composites. Specifically, porous lanthanum hexaluminate ($\text{LaMnAl}_1\text{O}_{19}$, LAM) and yttrium aluminum garnet ($\text{Y}_3\text{Al}_5\text{O}_{12}$, YAG) coatings were produced using citrate-based polymeric solutions that yielded the oxide plus a fugitive carbon phase. The intimate mixing of the carbon phase with the oxide allowed for homogenous, fine-scale porosity to be formed. These coatings were deposited onto Nextel™ 610 fiber; the coated fiber was subsequently evaluated through tensile testing after various heat treatments and after incorporation into minicomposites. Test results indicated that the LAM/C coatings degraded the fiber tow strength significantly after deposition. Alternately, the as-deposited YAG/C coatings had little effect on fiber tow strength and only a slight (~20 percent) loss in strength was seen after heat treatment at 1200 °C. Both porous coatings improved the strength of minicomposites, as compared to control samples produced with uncoated fiber. The loss in fiber strength from the LAM/C coatings, however, precludes its use in composites and this coating type was not examined further. The retention of tow strength and high minicomposite strengths found with the porous YAG coatings demonstrated that this coating type has the potential to provide the interfacial crack deflection needed in dense matrix ceramic matrix composites [40, 60].

4.1.1.5 Others

Electrostatic attraction has been used to deposit alumina and mullite coatings onto woven cloths of Nicalon™ fiber. This approach produced uniformly coated cloths, while minimizing the dependence on the wetting relationship between fiber and coating precursor. The use of low sol concentrations (=1 g/L) facilitated the removal of excess sol from the cloth. Water was used to further displace excess aqueous sol from the cloth to give minimal fiber-fiber bridging, while maintaining uniform fiber coatings. The use of a polyelectrolyte enabled multiple deposition of coatings onto the fibers in the cloth. Multiple coating steps resulted in completely coated fiber surfaces; coverage was limited to <50 percent with only a single coating step. Vacuum infiltration was necessary to remove entrapped air from the cloths during coating; however, a poor coating was still obtained at points of tow-tow crossover. The time required to outgas the cloth under vacuum suggests that a significant area of fiber remained in contact with air, rather than with the precursor liquid, especially during coating at atmospheric pressure [6].

4.1.2 Experimental Mechanics and Models

4.1.2.1 Evaluation Protocol: Micro-CMCs and Mini-CMCs

As part of the developmental effort on oxidation-resistant interphase concepts, it was necessary to establish a protocol to evaluate the effectiveness of the designs. This included the mechanical testing and fractography of individual fibers, fiber tows, microcomposites and minicomposites for each interphase concept, and finally testing CMC panels on the most promising interphase

concepts. With fiber testing, the measurement of the actual diameter of each test fiber was a bottleneck and ways to avoid this were studied with some promising outcomes.

4.1.2.1.1 Fiber Strength

The validity of using an average diameter (measured on a sample lot) instead of the actual fiber diameter for each tension test, was evaluated. Strengths and Weibull moduli for alumina/yttrium aluminum garnet eutectic (AYE) filaments and for Si-C-O (NicalonTM) filaments were calculated using measured and average filament diameters. The strengths agreed closely. Thus, an average filament diameter could be used instead of the measured filament diameter in calculating strengths. The Weibull modulus obtained from an average filament diameter approximates the Weibull modulus obtained using the measured filament diameter. The strength obtained using an average filament diameter for a set of specimens is in good agreement with the strength found using measured filament diameters. The estimator of the Weibull modulus derived using an average filament diameter is a good approximation of the estimator of the Weibull modulus derived from measured filament diameters. In practice, the determination of an average diameter for a particular type of filament should be necessary only once, provided that the filaments from which the average diameter was obtained are representative of all filaments from the same lot. Verification of the average diameter for different lots would be prudent. The alumina/YAG eutectic (AYE) filaments are an example of filaments that can vary significantly in diameter with different processing conditions. However, for most commercially available filaments, occasional confirmation should be sufficient. This work concluded that proper use of an average filament diameter is a valid procedure that will greatly facilitate determining the tensile strengths and Weibull moduli of filaments in an efficient manner [7].

Subsequent simulations reported in the literature had claimed errors from such methods. To determine its validity, the possible errors in the above conclusion from insufficient sampling size were examined. The errors in the use of average fiber diameter in calculating the mean strength (σ_m), Weibull reference strength (σ_o), and Weibull modulus (m) from failure loads of fibers were examined experimentally using sample sizes greater than the recommended value of 30. While the use of an average diameter gave very good estimates of the mean strength, the Weibull parameters (σ_o , m) were in significant error, supporting the simulation results. Computational approaches to reduce these errors were considered and a numerical procedure to extract the Weibull parameters from the means and standard deviations of the load and fiber diameter was found to be feasible provided the sample size was large. Parametric studies showed that, to obtain results within 10 percent error, sample sizes of ~175 are required. The recommended sample size for commercial fibers ranges from 75 to 200 depending on the scatter in the fiber diameter and the acceptable error [52].

4.1.2.1.2 Micro-CMCs

Oxide/oxide microcomposites were fabricated and tested to evaluate the effectiveness of monazite (LaPO_4) and hibonite ($\text{CaAl}_2\text{O}_{19}$) as interlayers in sapphire-reinforced alumina matrix composites. For interlayer thicknesses of 0.3 to 0.5 μm , both interlayers showed evidence of crack deflection; however, debond lengths in hibonite-coated specimens were limited to just a small fraction of the fiber diameter. Monazite-coated specimens showed multiple matrix cracks

and extensive debonding at the coating/matrix interface. Composite strengths were relatively high for both coatings, considering the fiber strength degradation during processing; the strengths were greater than the calculated matrix cracking stresses. However, the mean strengths were not significantly different from that of the control specimens, although coated composites had higher Weibull moduli. The lack of difference in strength is attributed to the porosity in the matrix. The results imply that the matrix density needs to be above 85 percent to evaluate novel interface strategies reliably [31].

4.1.2.1.3 Mini-CMCs

A procedure was developed to fabricate oxide-fiber-reinforced minicomposites with a dense matrix and evaluate oxidation-resistant interface coatings. Porous oxide (zirconia-silica mixture) and monazite coatings were evaluated using Nextel 720TM fiber-reinforced BlackglasTM matrix minicomposites. BN-coated and uncoated fibers were used as controls for comparison. The evaluation was based on ultimate failure strengths, fractography, and fiber push-in tests. All of the composites that used fiber coatings had ultimate strengths significantly better than the control that used uncoated fibers. In addition, porous-oxide-coated fibers were found to be similar to BN-coated fibers in strength, fractography and fiber push-in behavior. Monazite coated fibers resulted in similar ultimate strengths, but showed no appreciable fiber pullout. Fiber push-in tests showed that monazite debonds readily, but the frictional resistance is higher than BN or porous oxide [55].

The effectiveness of monazite coatings in dense matrix composites was evaluated by incorporating monazite-coated NextelTM 720 into three model matrices. Two glasses, SiO₂-Al₂O₃-CaO-MgO (1723 glass, Corning, Inc.) and K₂O-B₂O₃-SiO₂ (KBS, Corning, Inc.) were chosen as model matrices; however, it was found that these materials wet the monazite grain boundaries and the monazite/fiber interface, which precludes their use with monazite coatings. Dense SiO_xC_y (Blackglas, Allied-Signal) was chosen as the third model material and minicomposites produced with the monazite-coated NextelTM 720 displayed improved tensile properties over control samples containing uncoated fiber. Although the strength was improved, little fiber pull-out was seen on the fracture surface. Additionally, the overall strength was significantly lower than predicted from fiber tow strength values. Subsequent push-in testing revealed that the monazite did debond readily, indicating that the lack of fiber pull-out and the low strength were most likely caused by fiber degradation during processing. This work demonstrated that monazite can provide a weak interface in a dense matrix CMC [33].

4.1.2.1.4 CMC Panels

Fiber coatings are essential in dense matrix composites, where a crack-deflecting mechanism is needed in the interfacial region; in porous matrix CMCs, the matrix itself generally enables the crack deflection. There are certain cases in which monazite coatings could be beneficial in porous matrix composites by either increasing the temperature capability of the material through prevention of fiber/matrix interaction or by protecting the fiber from environmental attack. To demonstrate this fact, monazite-coated NextelTM 610, 650 and 720 fibers were incorporated into porous alumina matrices, and the resultant samples were tensile tested after various heat treatments. The results of this work indicate that monazite coatings do extend the lives of

NextelTM-based composites at 1200 °C for short time periods (5 hours). NextelTM 610/monazite/alumina composites displayed good strengths after long-term exposure (100 hours) at 1200 °C, compared to control samples, which displayed poor strength after only 5 hours at 1200 °C. Examination of the fracture surfaces revealed that debonding occurred either at the fiber/coating interface, at the coating/matrix interface, or within the coating. The NextelTM 650-based composites did not fare as well after the long-term exposure, due presumably to fiber strength degradation. Further work is needed to determine the cause and ideally eliminate this degradation. NextelTM 720-based composites displayed similar strengths either with or without the monazite coating. For these samples, therefore, no coatings may be needed. Optimization of the monazite coatings (thickness, porosity, etc.) is needed to further enhance and control the properties of oxide-oxide, NextelTM 610 and 650-based composites [53].

4.1.2.2 Tests and Models to Understand/Evaluate Interface Behavior

Modeling efforts focused on developing an understanding of the interface behavior. Crack deflection at the fiber-matrix interface was revisited to examine the He-Hutchinson criterion for the more realistic case of an axisymmetric fiber-matrix system. Modeling of relative fiber-matrix sliding was focused on including the interface roughness effects during progressive debonding and its relevance to oxide-oxide developmental composites. Further, the effect of the thermoelastic properties of the coating on the fiber-matrix interface behavior was modeled and simple design curves were generated. Finally, the ability to predict composite ultimate strength was explored.

4.1.2.2.1 Crack Deflection

Deflection of a matrix crack at the fiber/matrix interface is the initial mechanism required for obtaining enhanced toughness in CMCs. In this work, energy release rates were calculated for matrix cracks that either deflect or penetrate at the interface of an axisymmetric composite as a function of elastic mismatch, fiber volume fraction, and length of the deflected or penetrated crack. The energy release rates for the competing fracture modes were calculated numerically by means of the axisymmetric damage model developed by Pagano, which utilizes Reissner's variational principle and an assumed stress field to solve the appropriate boundary value problems. Crack deflection versus penetration was predicted by using an energy criterion analogous to that developed by He and Hutchinson. Results showed that, for equal crack extensions in deflection and penetration, crack deflection is more difficult for finite crack extension and finite fiber volume fraction than in the He and Hutchinson limit of zero volume fraction and/or infinitesimal crack extension. Allowing for different crack extensions for the deflected and penetrating cracks was shown to have a small effect at larger volume fractions. Fracture-mode data on model composites with well-established constitutive properties show penetration into the fibers (brittle behavior), as predicted by the present criteria for crack extensions larger than 0.2 percent of the fiber radius and in contrast to the He and Hutchinson criterion, which predicts crack deflection. This result suggests that the latter criterion may overestimate the prospects for crack deflection in composites with realistic fiber volume fractions and high ratios of fiber to matrix elastic modulus [16].

4.1.2.2.2 Progressive Debonding with Roughness

Potential effects of interfacial roughness in ceramic composites were studied using a model that includes the progressively increasing contribution of roughness with relative fiber/matrix displacement during debonding of the fiber/matrix interface. A parametric approach was used to study interfacial roughness in conjunction with other parameters such as strength, radius, and volume fraction of the fiber. The progressive roughness contribution during initial fiber/matrix sliding causes a high effective coefficient of friction as well as an increasing clamping stress, which leads to rapidly changing friction with increasing debond length. Calculated effects imply potentially significant contributions to the behavior of real composite systems and the necessity for explicit consideration in the interpretation of experimental data in order to correctly understand composite behavior. In a tension test, the Poisson's contraction of the fiber may negate the effects of roughness, allowing an effective constant shear stress approximation. This was evaluated using a piece-wise linear approximation to the progressive roughness model in the analysis of Curtin for composite stress-strain behavior; for the NicalonTM/SiC system, the effective μ was found to be lower than the values that would be obtained from fiber push-out tests and/or matrix crack spacings [10]. The model was successfully used to extract interface parameters from fiber push-out test data obtained on treated and untreated NicalonTM-reinforced SiC composites [17].

4.1.2.2.3 Fiber Coating Thermoelastic Effects

A method to incorporate the thermoelastic effects of fiber coatings into models of fiber/matrix composites was determined. The coated fiber is replaced by an effective transversely isotropic fiber such that the properties of this effective fiber can be used in composite models. This approach was used to determine the magnitude of errors resulting from neglect of the coatings in modeling fiber/matrix debonding and sliding and in the reduction of data from real composites. The effects of carbon and boron nitride coatings in the NicalonTM/SiC system were found to be significant. It was found that major errors can be expected from fitting models to experimental data if the compliance and CTE of the coatings are ignored, even when the coatings are thin. Wide use of the approach requires revision of composite models to allow inclusion of a transversely isotropic fiber. Such a revision was derived for a popular model for matrix cracking stress and again, significant effects were found to result from neglect of coatings [29].

4.1.2.2.4 Interface Debond Crack and UTS of CMC

The ultimate tensile strengths of a unidirectional glass-matrix composite were measured as a function of fiber volume fraction. The results were compared with predictions, using a refined solution of the stress field generated by an axisymmetric damage model, which incorporated the effect of stress concentration in the fiber caused by the presence of a matrix crack both before and after deflection at the fiber/matrix interface. Two possible locations for the fiber failure were considered: (1) at a transverse matrix crack, near a bonded fiber/coating interface, and (2) at the tip of a debond crack, at the fiber/coating interface. At low fiber volume fractions, the measured ultimate tensile strength matched the calculated prediction, assuming no crack deflection. For higher volume fractions, the calculated predictions for a debonded crack matched the observed values. The model results were relatively insensitive to debond length and interfacial shear stress

for the range of values in this study. In comparison, the global load-sharing model, which does not account for the stress singularity at the fiber/matrix interface, was found to overpredict the values of the ultimate tensile strength for all fiber volume fractions. An important contribution of the present work was to introduce the use of fiber volume fraction as a parameter for testing theoretical predictions of the mode of fiber failure [50].

4.1.3 Identify and Evaluate New System

4.1.3.1 Single-Crystal Yttrium Aluminum Garnet (YAG)

The fracture toughness of single-crystal YAG was measured as a function of temperature in air and under vacuum using the Single Edged Notched Beam (SENB) technique up to 1600 °C. The measured K_{IC} was 2.2 MPa·m^{1/2} at room temperature, and it increased with temperature above 1200 °C, reaching a value of 4.5 MPa·m^{1/2} at 1600 °C in air. The effects of crystallographic orientation and oxygen partial pressure on toughness were studied at 1600 °C. The toughness increased further to 5.5 MPa·m^{1/2} when tested under vacuum (10^{-5} torr) at 1600 °C. Both temperature and testing environments were found to influence the fracture toughness, but there was no significant effect of crystallographic orientation [9].

4.1.3.2 Alumina-YAG Eutectic Polycrystal

Dense polycrystalline eutectics of alumina and YAG were fabricated by hot pressing powders of pulverized arc-melted buttons at homologous temperatures of 0.9 to 0.93 T_{eu} (where T_{eu} is the eutectic temperature). The eutectic microstructure of arc-melted buttons was retained after densification, although the grain boundaries were decorated with equiaxed grains of alumina and YAG, ~1 to 5 μm in size; possible causes for their formation have been discussed in the cited reference. A comparison of the measured strength of the polycrystalline eutectic (274±61 MPa) with grain size and fracture toughness suggests that the strength-limiting flaws were significantly smaller than the mean grain size and larger than the mean eutectic spacing [45].

4.1.4 Ceramic Composite Processing

After developing the various interface control methods studied under this contract, the challenge then became incorporating the coatings into ceramic matrix composites. Differing composite processing techniques were employed depending upon the constituent materials and the desired density of the final product. Hot pressing and pressure infiltration/pressureless sintering were used for the evaluation of fugitive carbon coatings in dense (glass) and porous (mullite-alumina) matrix composites, respectively. For composites containing oxide coatings, gel casting and reaction bonding were utilized independently and in combination in an attempt to achieve a dense (>90 percent) alumina matrix reinforced with monazite-coated fiber. Vacuum bagging/pressureless sintering was used to fabricate porous matrix alumina samples containing an in situ YAG coating. The effectiveness of the various coatings will be discussed in the following sections.

4.1.4.1 CMCs with Fugitive Coatings

Fugitive carbon coatings were shown to be useful in hot-pressed, dense (>90 percent) matrix composites. Nextel™ 720/"C"/CAS composites retained ~80 percent of their as-processed strength after long-term heat treatment in air at 1000 °C for 500 hours. The coating thickness appeared to affect the composite properties, with the slightly thicker coating producing better results in unidirectional composites, while the thinner coating was more advantageous in the ±45° samples. For a given system, the coating thickness will have to be optimized with respect to off-axis properties and high temperature behavior. The overall strengths of the dense matrix composites in this work were significantly lower than anticipated, due to fiber strength loss during carbon coating and presumably to chemical interaction between the fiber and matrix at regions where the coating was discontinuous. This is supported by the continuing strength loss in the samples containing uncoated Nextel™ 720. To avoid this problem, carbon coatings with complete fiber coverage should be used, along with a more compatible matrix for the Nextel™ 720 fibers.

Porous matrix composites (Nextel™ 720/mullite-alumina) were fabricated using pressure infiltration/pressureless sintering and it was shown that the composite strength, after long-term exposure at elevated temperatures (1150 °C), was not dependent upon the state of the interface. This agrees with the existing views concerning these materials. Coatings may be beneficial in porous matrix composites for exposures at higher temperatures or for reactive fiber/matrix porous matrix composites for exposures at higher temperatures or for reactive fiber/matrix combinations [51]. This will be system specific, as shown by the beneficial effect of monazite in porous matrix Nextel™ 610/alumina composites [53].

4.1.4.2 CMCs with Oxide Coatings

Gel casting (GC) and reaction bonding (RB) were evaluated both independently and in combination for the production of dense alumina matrix minicomposites. Gel-cast alumina minicomposites displayed many radial cracks after sintering, giving a high (>25 percent) overall porosity; however, areas between the cracks appeared relatively dense (>90 percent). Minicomposites produced with monazite-coated Nextel™ 610 fiber displayed improved strengths and fiber pull-out over samples containing uncoated fiber. Most importantly, the monazite coating appeared to be deformed during pull-out, which supports work of other researchers on push-out specimens. Reaction-bonding studies were initiated using two compositions: (1) aluminum, titanium, alumina, and zirconia, or (2) Ti₃Al, alumina and zirconia. Both yielded reasonable monolith samples; however, the particle size of the Ti₃Al was easier to reduce. Therefore, the latter composition was used along with gel-casting agents to produce minicomposites using uncoated Nextel™ 610 fiber. Oxidation, sintering, and subsequent examination of the minicomposites revealed little radial cracking, along with a possible reaction between the fiber and matrix; a fiber coating is likely needed for protection. Aside from this result, the combined GCRB process appears to produce desirable minicomposites; further work is needed to optimize this process [37].

Yttrium aluminum garnet (YAG, Y₃Al₅O₁₂) was synthesized using a polymeric precursor derived from a mixed-metal citric acid/ethylene glycol/ethanol solution. YAG was found to crystallize

directly from an amorphous precursor beginning at temperatures as low as 600 °C within 1 hour in air. The polymer resin concentration was found to have an effect on the temperature of crystallization initiation. However, all precursors produced a well-crystallized YAG powder within 1 hour at 800 °C in air. Formation of phase-pure YAG in an argon atmosphere did not occur until heating for 1 hour at 1000 °C. An optimum cation-to-resin ratio to maximize reactivity provides a polymeric network to ensure a homogeneous dispersion of cations, yet minimizes cation diffusion distances within the char by limiting excess free carbon after polymer pyrolysis [47]. This solution-derived YAG was used in forming a two-phase matrix consisting of alumina particles bonded with the YAG; this matrix was reinforced with Nextel™ 610 cloth or Nextel™ 650 tows. The use of the solution-derived YAG as a second phase in the matrix was intended to provide an *in situ* fiber coating as well. However, due to the small amount of YAG allowed in the matrix during composite processing, YAG was not homogeneously distributed throughout the matrix and filled only a small fraction of the porosity. Segregation of yttrium was observed at all alumina grain boundaries in the matrix. The stress-strain behavior of the composites was compared to that of composites that did not contain the YAG second phase. In all cases, the YAG-containing composites gave higher ultimate stresses and greater strains to failure than the all-alumina composites when processed at 1200 °C. The composite strength of the alumina-YAG matrix composites was likely increased by minimizing either fiber degradation or matrix densification. Nextel™ 650 fiber-reinforced composites heat treated at 1200 °C for 100 hours had the same reduced strength, due to severe fiber degradation [60].

4.1.5 Structure-Property Understanding

4.1.5.1 Characterization and Experimental Techniques

In-depth characterization of materials is necessary for understanding structure-property relationships and designing of materials with improved properties and performance characteristics. This is particularly true for ceramic composites, whose properties may often depend strongly on subtle changes in the properties of their components, i.e., the fibers or fiber-matrix interfaces. Transmission electron microscopy (TEM) is a powerful and often irreplaceable tool to study such phenomena. However, technical difficulties in preparing thin foils of ceramic composites, in particular those utilizing the weak interface concept, and coated ceramic fibers often hinder the application of TEM in composite research. To overcome this obstacle, a new method of preparing TEM specimens of coated ceramic fibers was developed that produces large areas containing many electron transparent fibers, due to the minimal preferential milling of the epoxy matrix. In this method, multiple individual fibers or tows are impregnated with a high-temperature epoxy and constrained to assure a high fiber-to-epoxy volume ratio. The samples are then sectioned and mechanically thinned either parallel or normal to the fiber axes using a wedge polisher on diamond lapping films to achieve a thickness of less than 5 µm. The thinned sample is then ion milled to electron transparency in less than 30 minutes, giving representative specimens of the coatings, fiber, and coating-fiber interface. This technique is also well suited to preparing extremely flat specimens for both light microscopy and SEM analysis of the coatings [2, 5].

4.1.5.2 Long-Term Effects and Environmental Stability

Ceramic composites are generally materials for applications at high temperatures and/or aggressive environments. In addition, their fabrication usually involves high-temperature processing. Criteria important for the use of a material in ceramic composites include, chemical compatibility with other materials and thermal and environmental stability. Therefore, the effects of both the processing and the long-term exposure to the environment during service on the properties of ceramic composites and their components (fiber, interphase coatings, and matrices), and possible interactions between thereof, have been the focus of extensive research.

The effects of thermal exposure on the strengths of NextelTM 550 and 720 tows, bare and coated with carbon, were determined by room-temperature tensile testing. Single filaments were extracted for testing from tows that had been exposed to different thermal environments (i.e., air or vacuum) at temperatures from 550 ° to 1400 °C. It was found that uncoated NextelTM 550 filaments retained 75 percent of their as-received room temperature strength after thermal exposure at 1200 °C for 2 hours in air. CVD carbon coated NextelTM 550 filaments retained 75 percent of their strength after thermal exposure at 1000 °C for 2 hours in vacuum. NextelTM 550 filaments exhibited a higher room temperature tensile strength after thermal exposure in air than under vacuum. Strength after a thermal exposure at 1050 °C was not affected by the presence of the carbon coatings. Strength after thermal exposure under vacuum at 1050 ° and 1150 °C did not deteriorate as rapidly as after thermal exposure under vacuum between 950 ° and 1050 °C or between 1150 and 1250 °C. NextelTM 720 filaments maintained 75 percent of their as-received room temperature strength when thermally exposed at 1300 °C for 2 hours in air. They exhibited a higher room temperature tensile strength after thermal exposure in air than after being thermally exposed under vacuum. Strength was not influenced by the presence of the carbon coatings after a thermal exposure of 1050 °C. Strength loss between 1200 and 1300 °C (air thermal exposure) was not as great as between 1100 and 1200 °C or between 1300 and 1400 °C. The results of this study helped define the allowable composite processing conditions when using these tows. It was found that composite processing for a short period of time (2 hours) at 1100 and 1300°C, while maintaining > 70 percent of the as-received strength, is possible for NextelTM 550 and 720 filaments, respectively [28].

Furthermore, grain growth and its effect on the tensile strength of NextelTM 720 after thermal exposure from 1000 to 1500 °C for 20 minutes to 300 hours was investigated. Alumina grain growth in NextelTM 720 fibers was observed at temperatures above 1250 °C. Grain size distributions were log-normal, but exhibited slight bimodality at higher temperatures and longer times from intragranular alumina grains in the mullite. Above 1300 to 1350 °C, alumina grains grew with an activation energy of ~380 kJ/mol and a growth exponent, n, of 2–3. For a particular heat-treatment temperature, fiber tensile strengths decreased with $(\text{grain size})^{-1/2}$ with time as typically observed for ceramics. However, there was also a strength decrease with heat-treatment temperature that was unrelated to alumina grain size. Below 1250 to 1300 °C, the strength decrease with time at temperature was not associated with grain growth and was inferred to be related to stress corrosion and/or boundary grooving. Slight strength increases observed between 1250 and 1350 °C may be due to flaw healing [23].

Oxidation resistance is another environmental factor that is of key importance in the development of ceramic composites, particularly those incorporating nonoxide components, i.e., SiC-based ceramics. The oxidation behavior of SiC-reinforced CMCs was modeled by UES personnel, assisted by external collaboration [25]. With regard to fibers, the environmental stability of uncoated and BN-coated Nicalon™ fiber was investigated by studying the effect of annealing in air at 1000 °C (2 hours) on the strength of the fibers. The results imply that both uncoated and BN-coated fibers degrade in strength, with the BN-coated fiber suffering a higher strength loss. The degradation is significantly enhanced if the fibers are exposed to salt (NaCl) water prior to the air anneal and if the concentration of salt is more than 0.5wt%. The BN-coated Nicalon™ fibers were also studied at 800 and 900 °C. The degradation in strength due to salt water exposure was found to be greater at 800 °C than at 900 °C or 1000 °C [18]. A developmental amorphous SiBCN fiber was also investigated to evaluate its oxidation behavior. Fibers were heat treated in stagnant laboratory air at temperatures of 1300°-1500°C for 1 or 2 hours. It was found that the oxidized SiBCN fibers contained three distinct concentric layers, each increasing in oxygen concentration from the core to the outer surface. The unreacted fiber core retained its amorphous nature. The first oxidation layer, next to the core, consisted of a mixture of amorphous SiBCNO and turbostratic BN, which evolved into a more oxygen-rich glass with hexagonal and turbostratic BN grains dispersed throughout nearer the surface. The second layer consisted of essentially pure silica glass with no detectable B, C, or N present. The outermost layer in the fiber oxidized at 1500 °C had devitrified to cristobalite. The fiber suffered significant strength degradation after oxidation [54]. More recent work has suggested that oxidation of SiC could be inhibited by the presence of monazite on the fiber surface. The effect is significant even when the coating is not continuous, implying a chemical effect [34].

Monazite is considered one of the oxide-based alternatives to carbon and boron nitride fiber coatings to improve high-temperature environmental stability of ceramic composites. A major obstacle to the application of monazite in oxide-oxide CMCs, however, was fiber degradation during the fiber coating process. The effect of monazite coating deposition temperature on Nextel™ 720 fibers was studied from 900 to 1300 °C. The effects of long-term heat exposure were evaluated on fibers coated at 900 °C that were subsequently heat treated at 1200 °C for up to 100 hours. Coated fibers were characterized by analytical TEM, and tensile strengths were measured by single-filament tensile tests. The monazite precursor was characterized by X-ray diffraction, DTA/TGA, and mass spectroscopy. Microstructure evolution was complex and may have involved recrystallization of large defective grains into smaller grains, with subsequent growth of these grains, along with coarsening of the porosity. After 100 hours at 1200 °C, there was significant roughening of the coating-fiber interface, with faceting of alumina grains in the fiber and some lanthanum segregation to these faceted boundaries. Spheroidization of thin coatings was also observed. It was found that the tensile strength of coated fibers decreased with increasing deposition temperature and with time at temperature after deposition. The results suggested an environmental cause for the fiber strength decrease [35].

Al-Y-O compounds have received attention as candidate materials for turbine jet applications, both as fibers and matrices of ceramic composites. To evaluate their high-temperature environmental stability, heat treatments in several environments were performed on a series of compounds in the Al₂O₃ and Y₂O₃ system: Al₂O₃-Y₃Al₅O₁₂ eutectic, Y₃Al₅O₁₂, YAlO₃, Y₄Al₂O₉, and Y₂O₃. The yttrium aluminates were found to be stable at high temperatures under vacuum

and in air. However, when they were heat treated under vacuum in proximity of SiC, degradation was observed. This was found to be primarily a result of carbothermal reduction. In a similar reducing environment without Si, the yttrium aluminates, Al_2O_3 , and Y_2O_3 all exhibited degradation by carbothermal reduction. Based upon the experimental results, a degradation mechanism for yttrium aluminates was proposed [4].

4.1.5.3 Design Issues

As our understanding of composite behavior and the effect of process and structure variables increased, the focus shifted towards design implications. Several reports were prepared that summarized our state-of-the art understanding and the design issues that remain. Topography of the interfacial fracture surface has been shown to be a significant contributor to interfacial friction and is, therefore, a strong determinant of debond length and, hence, composite properties. The nuances of interface failure behavior have direct implications on the design of alternative fiber coatings for interface control. One requirement involves control of the coating compliance while another involves control of the interfacial fracture path, in addition to the first order requirement of accomplishing crack deflection. Such issues will require explicit attention for development of effective oxide-based approaches. These design requirements have been inferred as a result of consideration of the effects of fiber debond surface topography. Rough-surface modeling of experimental data has also provided preliminary evidence that the design space for coating toughness is larger than previously thought. Current understanding of the design requirements for fiber coatings, as derived from roughness related work, was summarized and the outstanding issues were identified [8, 19, 30, 59].

A key issue with oxide-oxide CMCs is the thermal gradient stresses resulting from the inferior thermal conductivity of oxides compared to nonoxides. However, since there are several different oxide fibers of different CTE available, the concept of mixing and using fibers of different CTE can be used to manage thermal stresses. For example, when there is a temperature gradient in the plane of a sheet-like part, the fibers of low CTE would be placed in the middle of the sheet/plate and the fibers of high CTE at the ends, which are colder. The differential CTE of fibers can also be used to minimize the extent of tensile and compressive stress regions, with the potential for increasing the operating temperature of the composite. Fiber degradation limits the use temperature of oxide-oxide composites. Using this invention, it will be possible to design weaves that are imbalanced in fiber type to allow for the degradation of the fibers near the hotter surface, since this surface will see only compressive stresses. The approach will allow simultaneous stress management and the use of hotter surface regions with degraded fiber properties as a thermal barrier for the load-carrying portion of the composite. A patent was filed and approved by the US Patent office [20]. The scientific component of the work was presented at the 25th Annual Conference on Composites, Advanced Ceramics, Materials and Structures, January 2001. A manuscript is in preparation and will be submitted for publication.

In an on-going work, the direct application of an oxide-oxide CMC in a novel combustor application was explored. Working closely with combustion designers in the Propulsion Directorate of AFRL, preliminary studies were conducted on an Inner Turbine Burner (ITB) that uses CMC materials on the cavity walls. A well-tested 2-D CFD code was used for the simultaneous simulation of reacting flow in the combustor and heat transfer in the metal parts.

Calculations made with stainless steel and CMC back plates showed that a reduction in wall temperature can be achieved with the latter. Numerical experiments were performed using fictitious metals with different material properties, such as back plates in the cavity, to understand the role of individual material properties on combustor performance [41].

4.1.6 Miscellaneous

4.1.6.1 Review of Structural Ceramic Composites

A review of major recent advances was conducted and published in "*Current Opinion in Solid State and Materials Science*." The review concluded that near-stoichiometric, small-diameter SiC fibers with excellent properties are now available and that new polycrystalline oxide fiber offers significantly improved temperature limits. Further, oxide fiber coatings that substitute for C and BN for deflecting cracks and promoting distributed damage appear feasible. Two show substantial low-temperature plasticity in constrained loading. Properties of SiC-BN-SiC and coatingless oxide composites have been improved markedly, but combustion atmospheres have proven more problematic than thought for the former [24]. Another review on interfaces has been submitted to the *Journal of the American Ceramic Society* [59] and a chapter on "Composite Mechanics and Behavior" has been contributed toward a *Ceramic Engineering Handbook* by Marcell Decker, Inc. [58]. A concise summary of the status and projected future of interfaces in CMCs was written as a chapter for a *Ceramic Engineering Handbook* [57].

4.1.6.2 In Situ Reinforced Mullite

The microstructural evolution, anisotropic grain growth, and in situ toughening of dense mullite annealed above 1550 °C were studied. Grain growth was relatively slow at 1550 °C and the microstructure remained nearly equiaxial. Annealing at temperatures above the eutectic temperature (~1590 °C) produced fairly rapid anisotropic grain growth. Stoichiometric mullite doped with 1.5 to 5wt% SiO₂ and 0.5 to 1.0wt% Y₂O₃ were also studied. Compared to the undoped mullite, the addition of SiO₂ and Y₂O₃ produced a small reduction in the grain growth kinetics. TEM analysis revealed that the glassy second phase was concentrated at the triple junctions or distributed inhomogeneously at the grain boundaries. For the samples annealed at 1750 °C, the indentation fracture toughness at room temperature increased from 2.0 to 2.5 MPa·m^½ for the undoped mullite to values as high as 4.0 to 4.5 MPa·m^½ for the doped mullite [36, 38, 49].

4.1.6.3 Processing of YAG

YAG powders were synthesized by precipitation of hydroxides using three types of precursors: nitrates (nitrate process), isopropoxides (alkoxide process), and isopropoxides chelated with ethyl acetoacetate (modified alkoxide process). The phase development in the powders during heat treatments was investigated with DTA and XRD. An intermediate hexagonal YAlO₃ (YAH) phase was formed at 800 °C in all powders regardless of the synthesis processes, but its complete transformation to YAG at higher temperatures (>1000 °C) occurred only in the powders prepared by the nitrate and modified alkoxide processes. The alkoxide process led to

the largest deviation from the bulk composition, producing a single phase of YAH that transformed into YAG plus a stable YAM ($\text{Y}_4\text{Al}_2\text{O}_9$) phase. The modified alkoxide process led to the most homogeneous bulk composition, resulting in the least amount of YAH in the powder. The poor chemical homogeneity in the powders prepared by the nitrate and alkoxide processes was attributed to the segregation of the hydroxides and to the presence of the double alkoxide, respectively [42].

4.1.6.4 SiC/MoS₂ Nanocomposite

A novel concept for in situ processing of SiC/MoS₂ nanocomposites has been developed that combines the pyrolysis of MoS₂ particles coated with polycarbosilane and subsequent densification by hot pressing. After densification, a uniform dispersion of SiC particles is obtained in the MoS₂ matrix. The strength at both and elevated temperature is dramatically improved by the processing protocol employed. The average room temperature flexural strength measured for the SiC/MoS₂ nanocomposite was 760 MPa versus 150 MPa for unreinforced MoS₂. The average 1250 °C flexural strength measured for the SiC/MoS₂ nanocomposite was 606 versus 77 MPa for unreinforced MoS₂ [15].

4.2 SUMMARY OF CURRENT WORK NOT REPORTED

4.2.1 Oxide CMC

4.2.1.1 Microstructural Evolution of Monazite Coatings for Oxide-Oxide Ceramic Composites: from Processing Sols to Minicomposites

Monazite microstructure has been studied from the coating sol to the interface coatings in the composites after extended exposure to heat (up to 100 hours at 1200 °C). It was found that the water sol contains needle-shaped nanocrystals of the monazite precursor rhabdophane ($\text{LaPO}_4 \cdot 0.5\text{H}_2\text{O}$), which form highly aligned bundles (Figure 3). Upon curing, the hexagonal lattice of rhabdophane transforms into the monoclinic lattice of monazite with the orientation relationship $[001]_{\text{R}} \rightarrow [100]_{\text{M}}$. The resulting monazite coating has bimodal crystallographic texturing with respect to the fiber axis (Figure 4). It was found that heat treatment of coated fibers at 1200 °C results in the coating spheroidization and loss of continuity, apparently due to the high energy of the fiber/monazite interface. However, in a composite, the matrix restrains this process, resulting in porous coatings with no spheroidization or discontinuity (Figure 5). Heat treatment results in significant grain growth in the monazite. A TEM study of the orientation of individual grains has revealed that this process is accompanied by an eventual complete loss of crystallographic orientation, typical for as-deposited coatings (Figure 6). A general schematic of the microstructural development of monazite fiber coatings in oxide-oxide composites is shown in Figure 7.

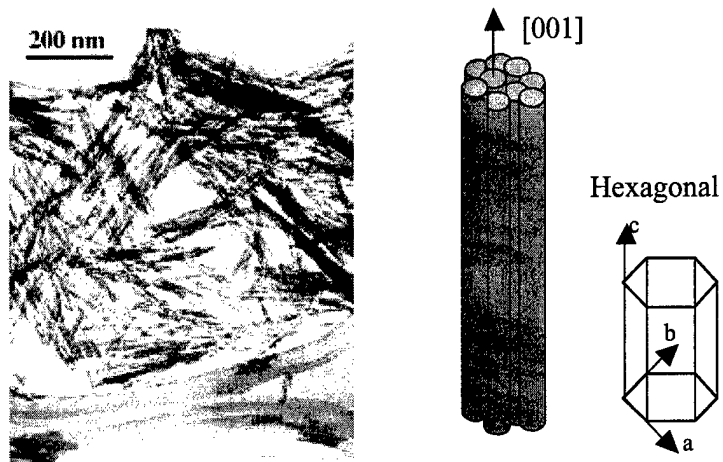


Figure 3. TEM Micrograph and Schematics Showing the Arrangement of Rhabdophane Nanocrystals in the Coating Sol

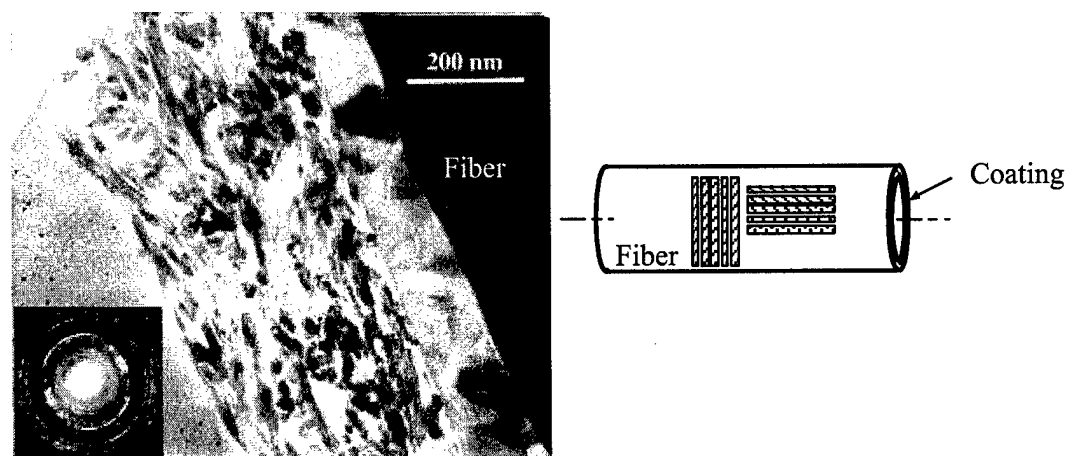


Figure 4. TEM Micrograph and Schematics of the Microstructure of As-Deposited Monazite Coating on Nextel™ 610 Fiber

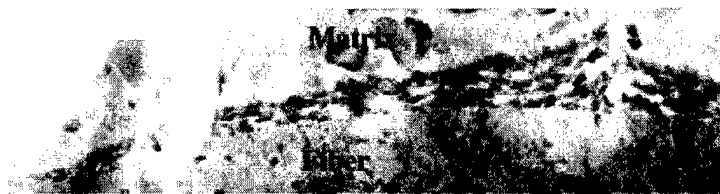


Figure 5. COI Nextel™ 720/Monazite/AS Composite As-Fabricated at 2100 °F

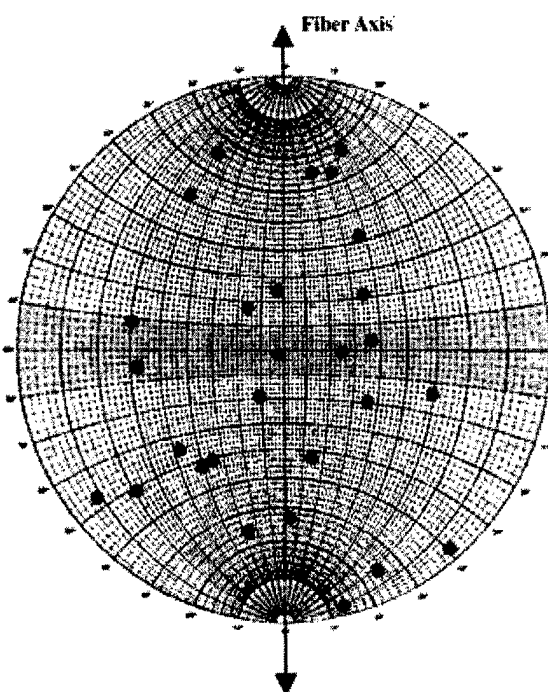


Figure 6. [100] Pole Figure Collected From Individual Grains in Monazite Coating in Nextel™ 610/Monazite/Al₂O₃ Minicomposite After Heat Treatment at 1200 °C For 100 Hours. Shaded Areas Show the Expected Locations Of The [100] Vectors if the Initial Texturing in the Coating was Preserved

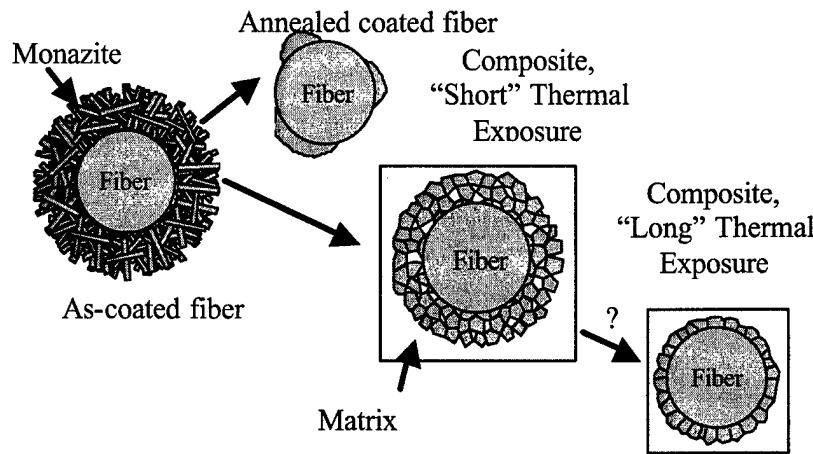


Figure 7. Schematic of Microstructural Development of Monazite Fiber Coatings in Oxide-Oxide Ceramic Composites

4.2.1.2 Microstructural Characterization of COI Nextel™ 720/Monazite/AS Composites

The microstructure of COI Nextel™ 720/Monazite/AS composites, both unidirectional and 0/90°, was studied using TEM. The materials were studied in the as-fabricated (2100 °F) condition and after additional heat treatment at 2200 °F. It was found that the monazite coating survived during the processing. Good coverage was typically observed, as seen in Figure 5. It was also found that in the as-fabricated materials, the coatings still showed evidence of the preferred orientation typical for as-deposited coatings (Figure 8a). Heat treatment at 2200 °F resulted in grain growth and the apparent loss of crystallographic orientation (Figure 8b), along with partial infiltration of silica into the coating. The latter agrees well with the results of the oxidation of monazite-coated SiC fibers and CVD SiC, which indicated that monazite is easily wet by silica. In some locations, this process was apparently accompanied by the dragging of small alumina particles from the matrix into the monazite coating (Figure 9).

In addition, a specimen heat treated at 1200 °C for 100 hours has been examined. It was found that, for areas where the coating was thin, such a prolonged heat treatment resulted in spheroidization of the coating, leaving isolated discontinuous grains of monazite at the fiber/matrix interface, as shown in Figure 10a. In other areas, where the coating was originally thicker, the heat treatment resulted in the formation of denser, uniform coatings (Figure 10b). Electron diffraction analysis and HRTEM imaging of the monazite grains and monazite/fiber interfaces confirmed the thermodynamic stability of monazite under these conditions (Figure 11).

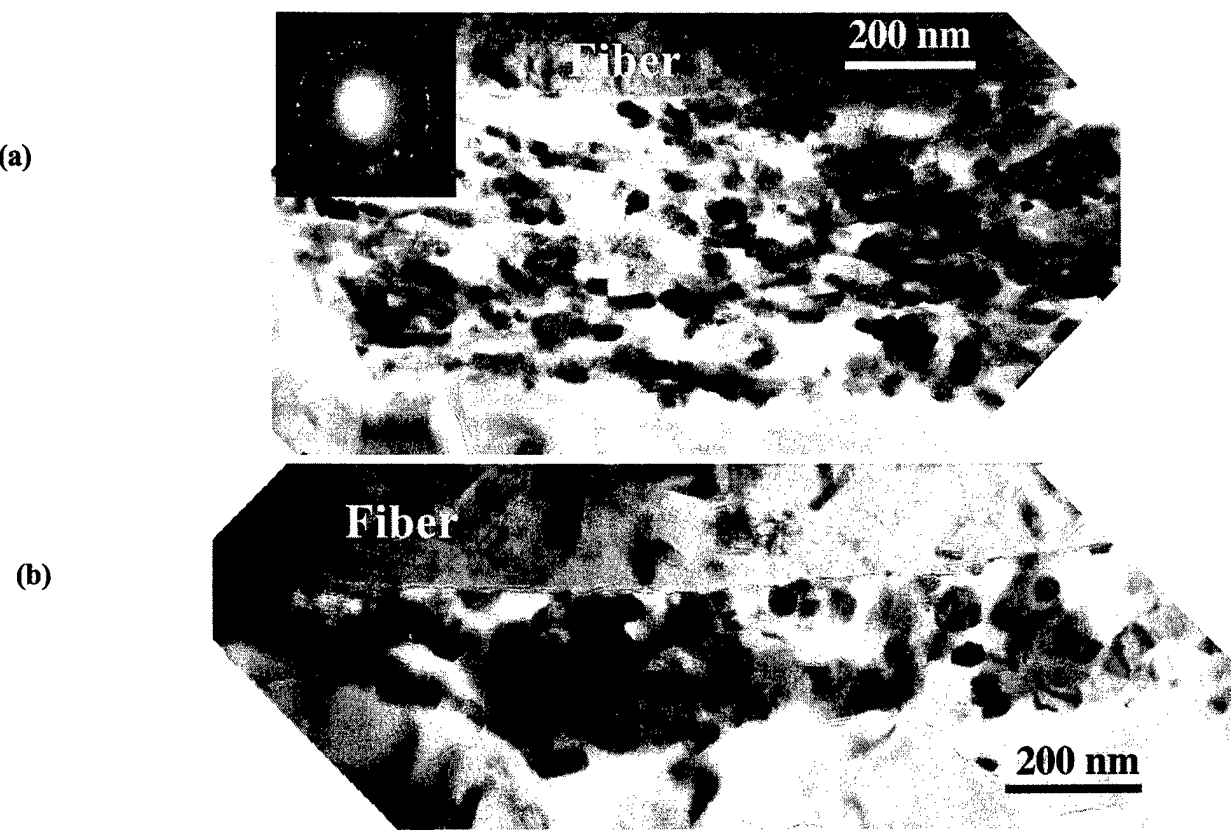


Figure 8. (a) TEM Micrograph Showing Preferred Orientation of the Coating in the As-Fabricated COI NextelTM 720/Monazite/AS Material; (b) Grain Growth and Apparent Loss of Crystallographic Orientation in the Same Material After Heat Treatment at 2200 °F

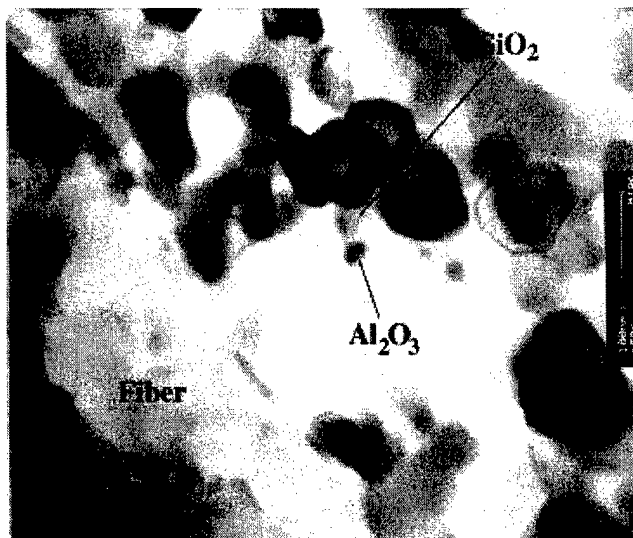


Figure 9. TEM Micrograph Showing Partial Infiltration of Silica and an Al_2O_3 Particle Dragged Into the Monazite Coating in the As-Fabricated COI NextelTM 720/Monazite/AS Material

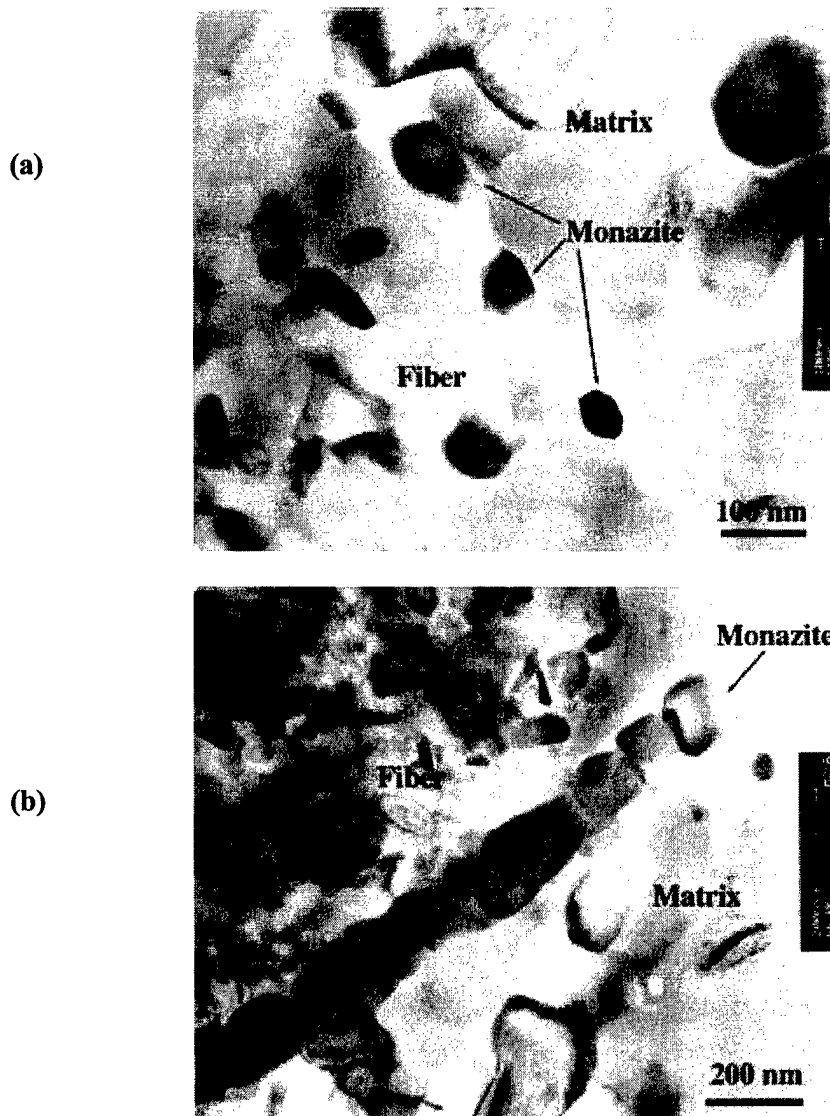


Figure 10. (a) TEM Micrographs Showing Spheroidization and Formation of Isolated Discontinuous Grains of Monazite in Thin Coatings, and (b) Formation of Thicker Dense Uniform Coatings in COI Nextel™ 720/Monazite/AS Material After Heat Treatment at 1200 °C for 100 Hours

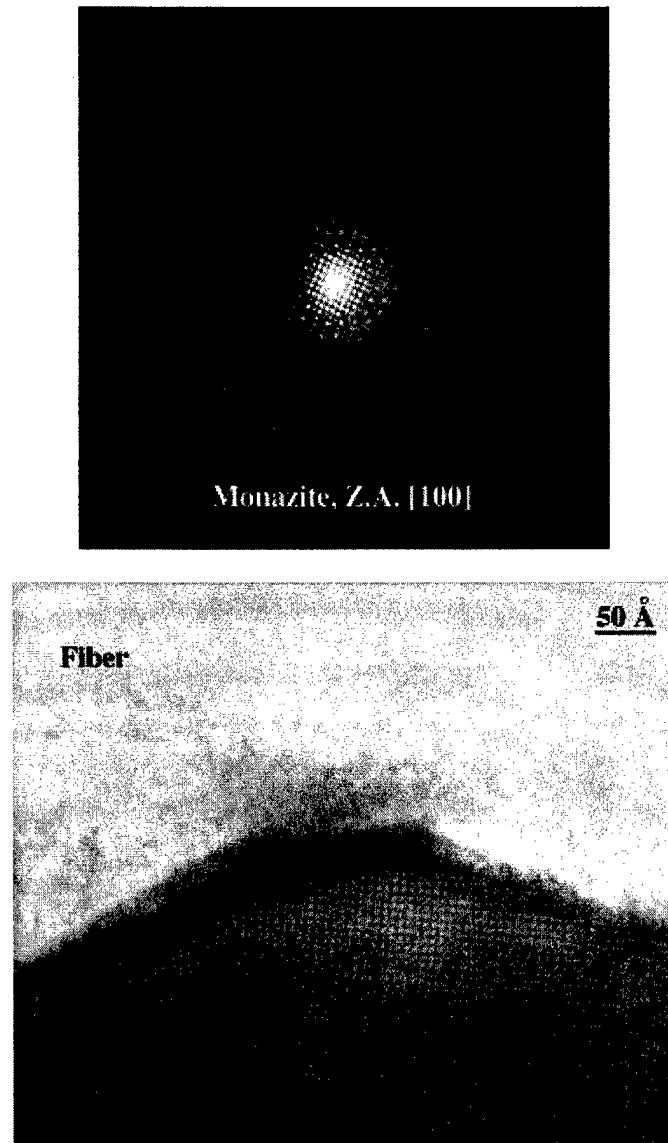


Figure 11. CBED Pattern from Monazite and HRTEM Image of the Monazite/Fiber Interface Confirming the Thermodynamic Stability of Monazite in COI Nextel 720/Monazite/AS Material after Heat Treatment at 1200 °C for 100 hours

4.2.1.3 Effect of Long-Term, High-Temperature Exposures on Nextel™ 610/Monazite/Alumina Composites

Porous matrix Nextel™ 610/monazite/alumina composites have been subjected to long-term, high-temperature heat treatments (1200 °C/100 hours/air), as reported in Section 4.1.2.1.4. Since publishing the aforementioned data, further work has been accomplished in this system. Fiber push-in tests were performed on samples after heat treatment at 1200 °C for 5 or 100 hours in air. Both control samples (uncoated fiber) and monazite-containing specimens were evaluated. Preliminary examination of the data revealed that, as expected, the fibers in the control samples could not be pushed. Alternately, the monazite-coated fibers could be pushed after either 5 or 100 hours at 1200 °C, indicating that a weak interface was retained during the heat treatments. These results are supported by the fractographic analysis. No fiber pull-out is seen in control samples, while fiber pull-out is seen in the Nextel™ 610/monazite/alumina samples. Further fiber push-in/push-out testing will be conducted, since the loads required to push the monazite-coated fiber after the 100 hour exposure were significantly lower than after the 5 hour exposure. Fiber tow testing revealed that the heat treatment alone would not degrade the fiber strength; therefore, the state of the interface must be changing. One possibility for the lower loads is the spheroidization of the monazite coating during heat treatment; this would leave a gap at the fiber/matrix interface, similar to fugitive coatings. TEM analysis of the push-in specimens is currently underway to determine if this is the case.

Another set of Nextel™ 610/monazite/alumina specimens were produced for longer term (250, 500 and 1000 hour) exposures at 1200 °C. Results of the 250 hour hold appear promising, since the composite retained approximately two-thirds of its strength, which is significantly better than control samples, where over 70 percent strength loss was seen after only 5 hours at 1200 °C (Figure 12).

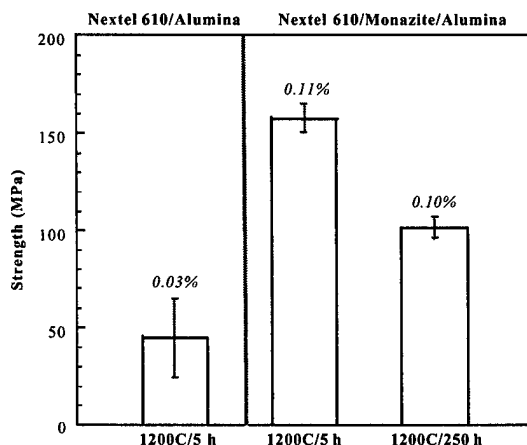


Figure 12. Tensile Test Results for Oxide-Oxide CMCs (Note: Values in Italic are Average strain).

The fracture surfaces of these samples also appeared "woody", indicating fiber pull-out. Additionally, tensile testing at high temperature (1200 °C) will be conducted. The results of this work will serve to confirm the long-term, high-temperature stability of monazite coatings in oxide-oxide composites. An article will ultimately be written and submitted for publication in the *Journal of the American Ceramic Society*.

4.2.1.4 Tow Weavability

Making CMCs with fiber cloth may be easier and more practical than with the tow alone. But sol-gel coatings of fiber cloths have an inherent disadvantage in that the fibers are in close

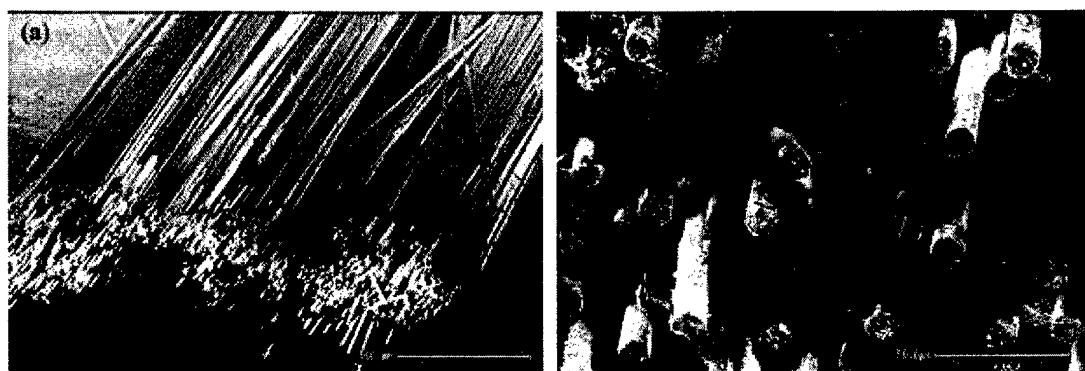


Figure 13. PVA Sizing of Coated Nextel™ 720 Showing: (a) Filaments Bundled Together and (b) PVA crust.

proximity and cross-over points are difficult to coat. Preliminary experiments were carried out to produce coated cloth by weaving monazite-coated tows. Monazite coatings on tows have been made, but the coated fibers have to be sized before they are woven. A 1.4 g/l polyvinyl acetate sizing was applied on coated Nextel™ 720 fiber tows (Figure 13a). The sizing did not coat individual filaments but formed bridges and crusts that bundled the filaments together (Figure 13b). The sized tows were run through an experimental weaving apparatus, and the filaments were then separated and tested. The average filament strength was 1.65 GPa. Some sized tows were tested for weavability, desized at 1000 °C, separated, and tensile tested. The average filament strength was 1.95 GPa. The coated tows will be sent to Techniweave (Albany International, Rochester, NH) to assess the weavability of the coated tows.

4.2.1.5 Commercial CMC Characterization for Thermal Gradient Exposure

As part of a collaborative research effort with the Propulsion Directorate, a study was initiated to evaluate the mechanical properties and microstructural stability of a commercial porous matrix ceramic composite (Nextel™ 720/Aluminosilicate, Composite Optics, Inc.) exposed to a thermal gradient, where one surface was above the material use temperature. To accomplish this goal, a maximum temperature of 1300 °C was chosen, which is well over the <1100 °C constant use temperature. Initially, samples were isothermally exposed to various temperatures (1100, 1200

and 1300 °C) for 100 hours in air and then either tensile tested or subjected to mercury porosimetry. Mercury porosimetry revealed that the as-received samples contained ~23 percent porosity, which decreased to ~18 percent porosity after the 1300 °C heat treatment. It should be noted that mercury intrusion accounts only for open porosity, not closed. In all conditions, the majority of pores were in the range of 0.2 to 0.01 µm, although the pore size distribution shifted to larger sizes with increasing temperature, presumably due to pore coarsening and crack opening. Few pores were evident with sizes below 0.01 µm. SEM analysis of the as-received materials revealed a microcracked matrix, which is common in porous matrix composites and arises from shrinkage of the matrix while being constrained by the fabric. In mercury porosimetry analysis, these cracks will show as pores with diameters proportional to the crack opening. Further microstructural characterization is needed to correlate the mercury intrusion and SEM results. The use of mercury porosimetry as a composite evaluation tool will be written and submitted for publication.

Along with microstructural evaluation, the mechanical properties of the composites after the isothermal and thermal gradient exposures will be measured. These values will be used in modeling the behavior of the composite after exposure to a thermal gradient. Preliminary tests were conducted wherein the commercial composite was exposed to a thermal gradient of ~250 °C, with one side at 1200 or 1250 °C and the cool side at ~950 to 1000 °C. Samples were held for either 8 or 24 hours under these gradients and subsequently tensile tested. For the samples exposed to a maximum temperature of 1200 °C, degradation or brittle failure was seen in only the outer layer of the composite. With a maximum temperature of 1250 °C, between two and three fiber layers were degraded. The depth of degradation in both cases agrees roughly with a simplistic model that assumes a linear thermal gradient through the sample. Additional thermal gradient exposures will be conducted, using 1250 °C or above as the maximum temperature and up to 100 hour heat treatments. Tensile test results from the thermal gradient samples will be correlated with the isothermal composite strengths and subsequently used in modeling the behavior of these materials under a thermal gradient. Upon conclusion of the study, the results will be written and submitted for publication.

4.2.1.6 Porous Matrix Composite Processing

Over the course of the contract period, extensive work has gone into producing oxide-oxide CMCs using pressure infiltration/pressureless sintering and vacuum bagging/pressureless sintering. Various fiber/matrix combinations have been utilized, as discussed in the summary of completed work. For future commercial use of porous matrix, oxide-oxide CMCs, pressure infiltration and/or vacuum bagging appears to be the most viable processing technique(s). This is particularly true if fiber coatings are utilized; coating a cloth will be much more efficient than coating the individual tows. Work will continue in the area of CMC production using pressure infiltration and vacuum bagging, with a goal of reproducibility and increased density. For example, in the area of increased density, multiple infiltrations of green composites with various oxide sols have been studied; weight increases of over 10 percent have been obtained in some cases. In terms of reproducibility, Nextel™ 610/alumina composites have been routinely fabricated with strengths of approximately 200 MPa after sintering at 1100 °C. Alternately, heat treating at 1200 °C for the same time period results in a dramatic (>70 percent) loss in strength,

which suggests the need for the interface coating. The experience gained in producing these samples will be utilized in future CMC experimental studies.

4.2.1.7 NextelTM 610/Alumina-YAG Composites

Work concerning the NextelTM 610/alumina-YAG composites discussed in Section 4.1.4.2 has continued. In the previous work, bulk composites could be heat treated only in air, due to furnace constraints. However, in this later work, NextelTM 610/alumina-YAG composites were heat treated in argon at 1000 °C, prior to final sintering at 1200 °C in air. This allowed for the crystallization of YAG from the precursors in the matrix, while still retaining the carbon phase. The carbon was then burned from the matrix, ideally leaving a continuous, porous YAG phase between the alumina particles and at the alumina particle/fiber interface. Tensile testing of these samples after heat treatment at 1200 °C for 5 hours demonstrated high strengths, as compared to control samples (NextelTM 610/alumina). Long-term exposures of these composites are needed to determine if the porous YAG phase is stable and if it helps retain the composite strength. TEM analysis is also underway to determine if the desired microstructure was attained. Further work in this area will be decided upon after reviewing the results of this work.

4.2.1.8 NextelTM 650 Fiber Characterization

NextelTM 650 fiber was examined as part of the reported work [53]. Due to the “kinking” and strength degradation seen in the fiber at higher temperatures (1200 °C), additional characterization of the fiber has been initiated. XRD analysis indicated that the fiber was initially alumina plus cubic zirconia; however, after heat treatment at 1200 °C, the peak splits indicate the presence of tetragonal zirconia. TEM analysis of the fiber has been conducted and will be correlated with XRD and fiber tow testing. UES, Inc. has been in contact with 3M, Inc. to transfer data obtained on this material. Ideally, the cause of the fiber degradation can be elucidated and a better fiber obtained.

4.2.1.9 Dense Matrix Processing Through Reaction Bonding

Preliminary experiments were carried out to explore processing schemes for achieving near-net shape, dense (and/or impermeable) refractory matrices in CMCs. Initially, an alumina-based matrix, produced through RB, was considered. The underlying main issue in the reaction bonding of aluminum is volume change. First, there is approximately a 14 percent volume increase in going from solid aluminum to liquid aluminum. Promoting high solid/gas oxidation (<660 °C) may alleviate this problem. The overall volume increase due to oxidation of solid aluminum is ~28 percent. The initial oxidation product of aluminum is gamma alumina, which transforms to the stable alpha phase around 1000 °C. This transformation involves about a 20 percent specific volume decrease. Thus, the oxidation of aluminum undergoes a series of volume changes depending upon the processing conditions. The specific volume decrease from the gamma to alpha phase transformation would be detrimental to filling the pore space in the CMC matrix.

Other RB candidate metals were considered, based on their refractoriness and the compatibility of the final oxides with the CMC constituents. Two other candidates were selected along with

aluminum: titanium (also Ti₃Al) and niobium. The RB mixtures were attrition milled (ZrO₂ lining, arms, and balls) with mineral spirits, followed by cleaning and drying. The oxidation behavior of the milled powder mixtures was evaluated using DTA/TGA to determine the oxidation processing temperature. The oxidation products were characterized using XRD. Pellets were made from the attrition-milled powder mixtures using a cold isostatic press. A series of reaction bonding experiments were carried out. Invariably, the pressed pellets increased their volume after RB without densification. Constraining (e.g., encapsulation) the expansion during RB improved the bulk density of the pellets somewhat (less volume expansion) without forming cracks. A considerable particle size reduction of Ti₃Al was achieved through attrition milling and the Ti₃Al was amorphotized during the milling process. However, the final oxides after RB were the same as those of the mixed powder. The attrition-milled Ti₃Al appears to be a good candidate matrix material for further study.

It should be pointed out that there is a fundamental difference between RB of metal oxide (RBMO) and silicon nitride (RBSN). For RBSN, the reaction mechanism is primarily a gas/gas reaction and takes place within the void space of the silicon preform. Thus for RBSN, the silicon preform shape is maintained throughout the reaction densification period. Typically, the metal oxidation involves a solid/gas reaction and the growth direction of the oxide scale can not be controlled, which results in volume expansion.

Another processing scheme was explored to alleviate RBMO difficulties. This scheme involved the melt-infiltration of metal (e.g., liquid aluminum) into a porous matrix oxide containing a fugitive carbon phase. After melt-infiltration, the fugitive carbon phase is burned-out, followed by oxidation RB. The merit of this approach is to promote directional oxidation of the metal toward the gap created by the fugitive carbon, thus minimizing the oxidation volume expansion. An initial experiment was unsuccessful due to the nonwetting (melt-infiltration) behavior of liquid aluminum with the oxide-carbon mixture preform.

Dense matrix processing through RB does not appear to be a viable route at present. However, a combination of melt-infiltration and gas/gas reactions (through reactive gases that generate a metal-containing gas phase) may be interesting for further study.

4.2.2 Nonoxide CMCs

4.2.2.1 Monazite Coatings of Tyranno™-SA Tows

4.2.2.1.1 *Effects of Sol Concentration on Coating Uniformity*

Tyranno™-SA fiber tows were coated with 20 g/l and 35 g/l washed rhabdophane precursors using 1-octanol as an immiscible liquid displacement agent. SEM analysis showed crust formation in coatings made from both the 20 g/l and 35 g/l precursors. However, coatings from the 35 g/l precursor displayed far more crusting (Figure 14). The viscosity of the 20 g/l monazite sol was 3 cP and the viscosity of the 35 g/l sol was 7.2 cP. Crusting is the result of the inability of 1-octanol to fully displace the highly viscous sols, typically sols of viscosity > 3 cP.

4.2.2.1.2 Oxidation Protection

The coated and uncoated Tyranno™-SA tows were heat treated in air at 1200 °C for 1, 2, 5, and 10 hours. The coated filaments were separated and tensile tested after heat-treatment. The uncoated filaments were bonded together by silica, which prevented the separation of individual filaments. Therefore, the uncoated filaments were not tensile tested. The silica layer thickness was measured from SEM and TEM micrographs.

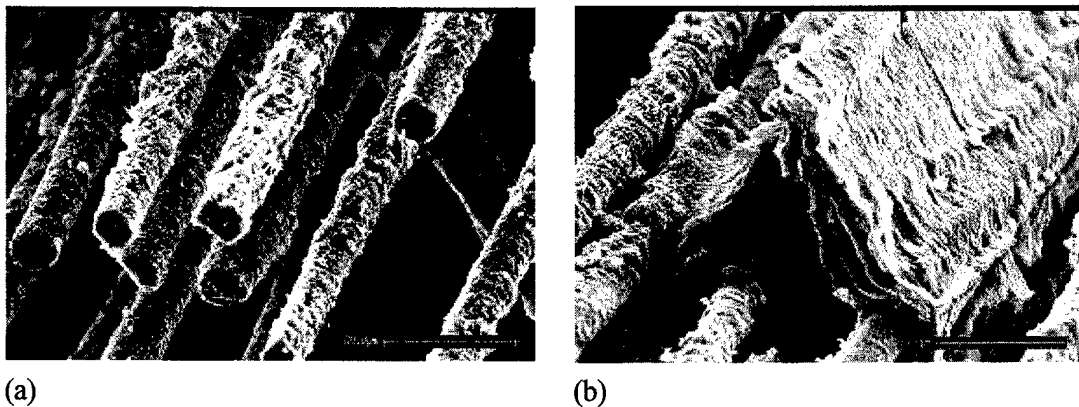


Figure 14. SEM micrographs of Monazite Coating on Tyranno-SA Fiber With (a) No Crusting and, (b) Crusting

Monazite-coated fibers were more oxidation resistant than uncoated fibers for all heat treatments (Figure 15). The silica oxidation product was amorphous. The monazite coating thickness was variable, while the silica film thickness was uniform and independent of the monazite coating thickness (Figure 15). Silica growth followed parabolic kinetics. The parabolic rate constants with and without monazite coatings were $10.2 \text{ by } 10^3$ and $50.1 \text{ by } 10^3 \text{ nm}^2/\text{h}$, respectively.

TEM electron diffraction and Energy Dispersion Spectroscopy (EDS) showed that the monazite coatings were pure and did not interact with the fiber after heat treatment at 1200 °C in air. Monazite coatings were porous before heat treatment, but still inhibited silica growth. Coatings heat treated at 1200 °C in air for 10 hours were dense, but thinner coatings spheroidized and were discontinuous. The observed oxidation inhibition is clearly unrelated to oxygen diffusion through monazite.

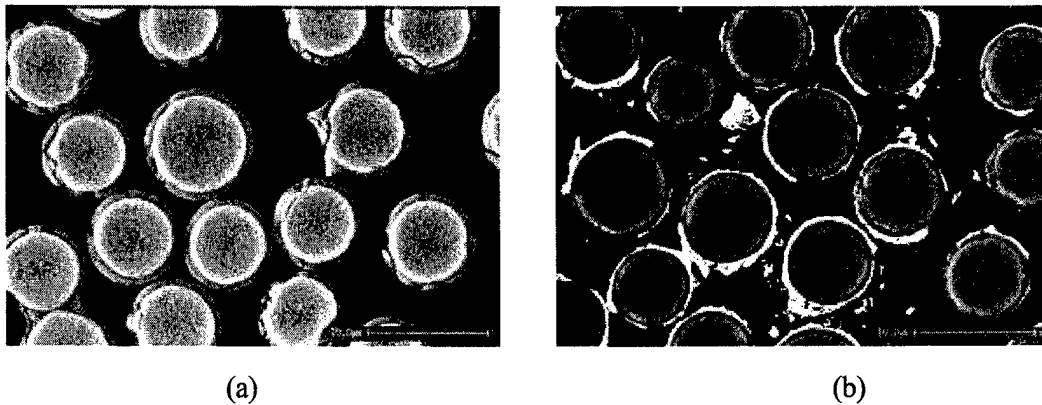


Figure 15. SEM Micrographs of Tyranno-SA Heat Treated in Air at 1200 °C/10 Hours:
(a) Without, and (b) With Coatings

4.2.2.1.3 Filament Tensile Strength

Table 3 summarizes the strengths of coated fibers. Tensile filament strength is retained for the four-, five-, and six-pass coatings. Similar strength retention results were observed for monazite coatings on oxide fibers with the washed rhabdophane sol. A plot of the tensile filament strength of the monazite-coated Tyranno™-SA fiber heat treated at 1200 °C in air versus the silica film thickness is presented in Figure 16. The tensile filament strength of the as-coated fiber was 2.61 GPa. The tensile filament strength of the heat-treated fiber decreased with increasing silica film thickness. The strength value of the fiber corresponding to a silica film thickness of 90 nm was higher than the control, which may be due to flaw healing by silica. This implies that there may be a threshold silica film thickness that strengthens the Tyranno™-SA fiber.

Table III. Tensile Filament Strength of Tyranno™-SA Coated Fiber

# of Coats	Control	4	5	6
Strength (GPa)	2.30	2.44	2.61	2.49
Weibull Modulus	5.1	7.9	8.0	6.3

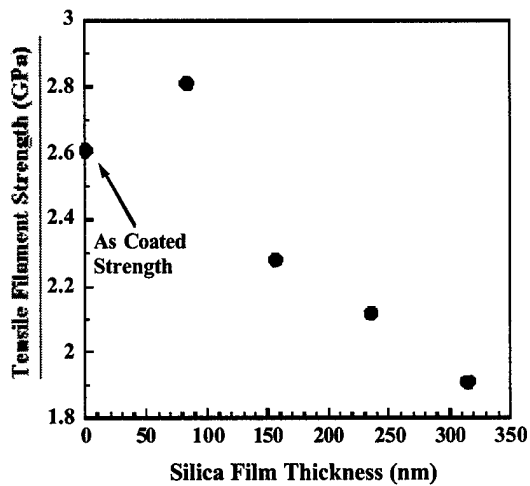


Figure 16. Tensile Filament Strength of Heat-Treated Monazite Coated TyrannoTM-SA Fiber Versus Silica Film Thickness.

4.2.2.2. Monazite Coatings of SylramicTM, TyrannoTM-SA, Hi-NicalonTM, and Hi-NicalonTM-S: Coating Retention

SylramicTM, TyrannoTM-SA, Hi-NicalonTM, and Hi-NicalonTM-S fiber tows were coated with 20 g/l washed rhadophane sol. The monazite coating retention was assessed with SEM analysis, which indicated that the retention depended upon the surface roughness of the fiber. Coating retention was in the order: SylramicTM ~ TyrannoTM-SA > Hi-NicalonTM ~ Hi-NicalonTM-S (Figure 17). Surface roughness followed the same order (Figure 18). Mechanical interlocking of the coating on rough surfaces of the fiber may be responsible for coating retention on the fibers. In addition, the high surface area created by the roughness enhances the physical bond between the fiber and the monazite film. A thin carbon film on the fiber surface, formed from free carbon in the fiber, may cause monazite to debond. Quantification of the free carbon in the fiber and its relation to coating retention may be needed.

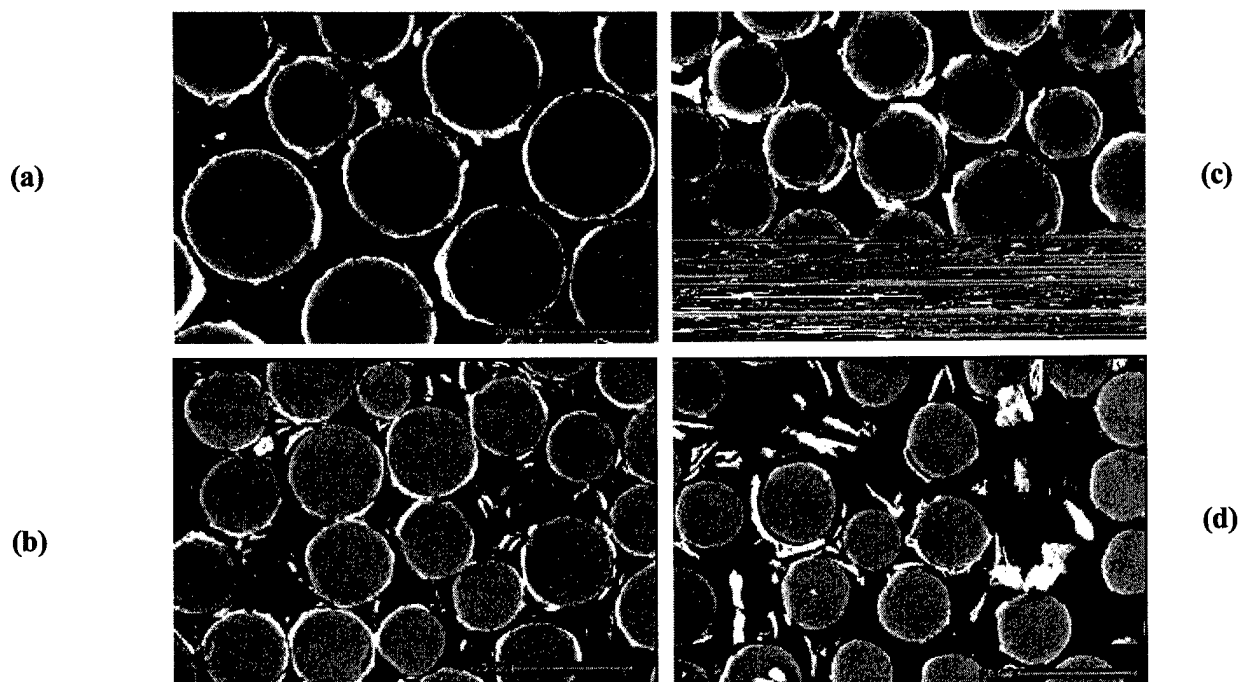


Figure 17. Monazite Coating on (a) SylramicTM, (b)TyrannoTM-SA, (c) Hi-NicalonTM , and (d) Hi-NicalonTM-S

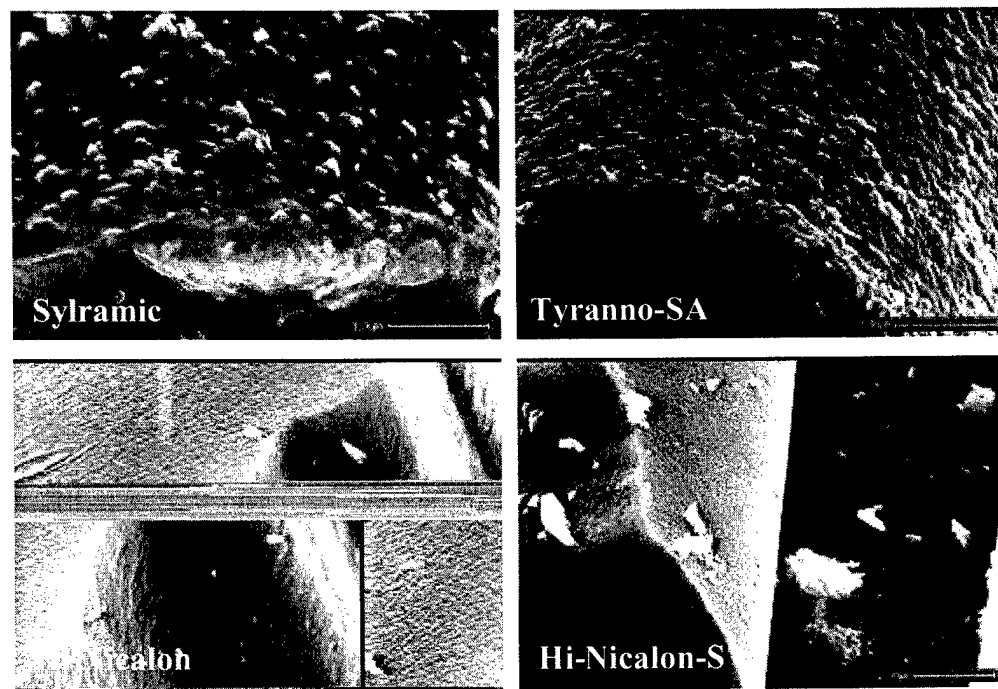


Figure 18. Surface Roughness of SylramicTM , TyrannoTM-SA, Hi-NicalonTM , and Hi-NicalonTM-S

4.2.2.3 Application of Monazite Coatings in SiC/SiC Composites:

The potential of monazite as an interphase in SiC/SiC CMCs was explored. In principle, monazite can enhance the resistance to oxidation/moisture of SiC/SiC CMCs, which otherwise are limited by the oxidation/moisture resistance of C or BN. The relevant issues are (1) Does monazite provide a weak interface? (2) Can monazite survive the Chemical Vapor Infiltration (CVI) processing of matrix SiC? (3) Is monazite stable with SiC at low PO₂? and (4) Does monazite provide a significant barrier to oxidation for the SiC fiber? To answer these questions, UES, Inc. worked with ORNL and with BF Goodrich and Hypertherm, Inc. through NASA. Results showed that the monazite-coated fibers retained fiber strength and showed signs of weak bonding. In fact, the real issue was survival of the monazite coating without spallation during transport and processing.

Four CVD-processed materials have been investigated using analytical TEM:

(1) Sylramic™/Monazite/CVI-SiC (Hypotherm), (2) Sylramic™/Monazite/CVI-SiC (BF Goodrich), (3) Tyranno™ SA/Monazite/CVI-SiC (ORNL), and (4) Hi-Nicalon™/Monazite/CVI SiC (BF Goodrich). The Hypotherm specimen possessed good integrity and under TEM investigation showed good overall retention of the coating, Figure 19a-d, although a layer of silica glass was easily detectable at the fiber/coating interface, Figure 19c. Element mapping and point EDX analysis revealed that the original monazite coating was severely affected by chemical reaction, with only isolated, if any, pockets of original monazite composition present (Figure 20).

In the BF Goodrich (Sylamic™) material, no coating or its remains could be detected using TEM and EDX analyses. However, it must be noted that since the specimen was very fragile, TEM specimen preparation was difficult and the number of fiber/matrix interfaces available for examination was extremely limited. A typical TEM image of a fiber/matrix interface is shown in Figure 21a. EDX examination revealed a significant amount of oxygen in the CVD-SiC matrix, Figure 21b. In one of the cases (BF Goodrich, Inc.), monazite was found to survive the CVI processing cycle. Figure 22 shows the TEM micrographs obtained for these mini-CMCs, showing that monazite survived the processing, although it was not physically continuous around the fiber.

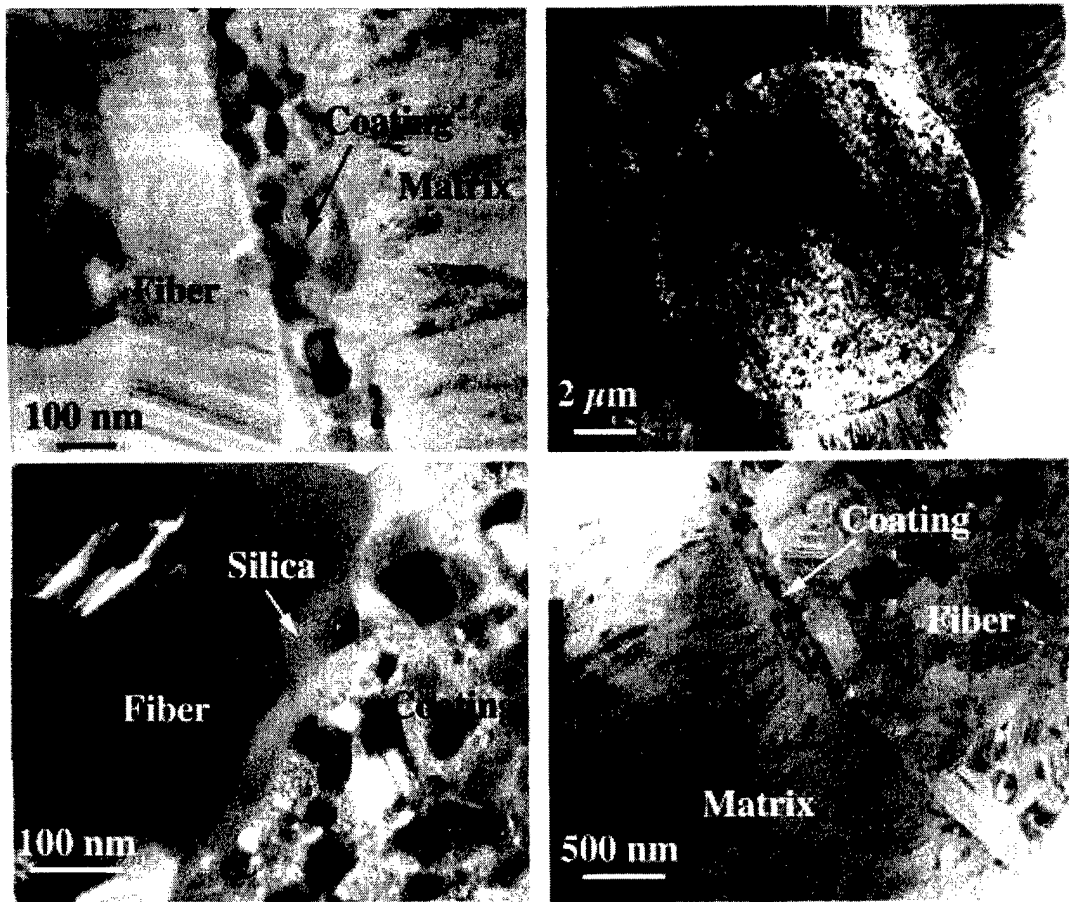


Figure 19. TEM Micrographs Showing Fiber/Coating/Matrix Interfaces in the Sylramic™/Monazite/CVD-SiC (Hypotherm) Material

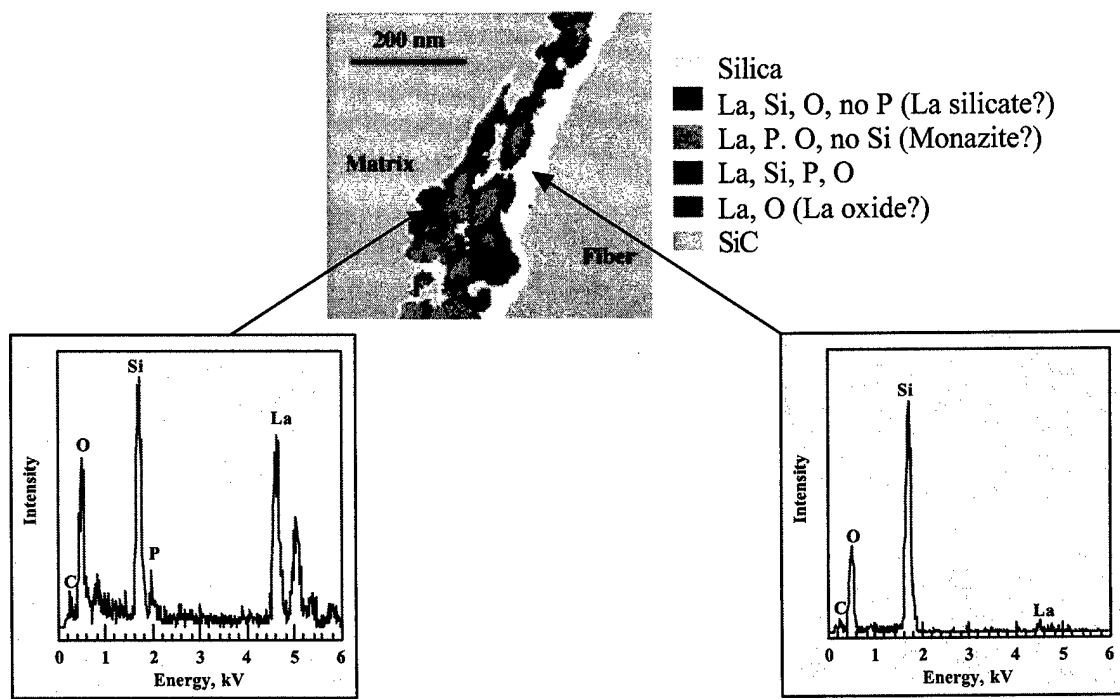


Figure 20. EDX Maps and Spectra Showing the Extent of Chemical Reaction at Fiber/Coating/Matrix Interfaces in the Sylramic/Monazite/CVD-SiC (Hypotherm) Material

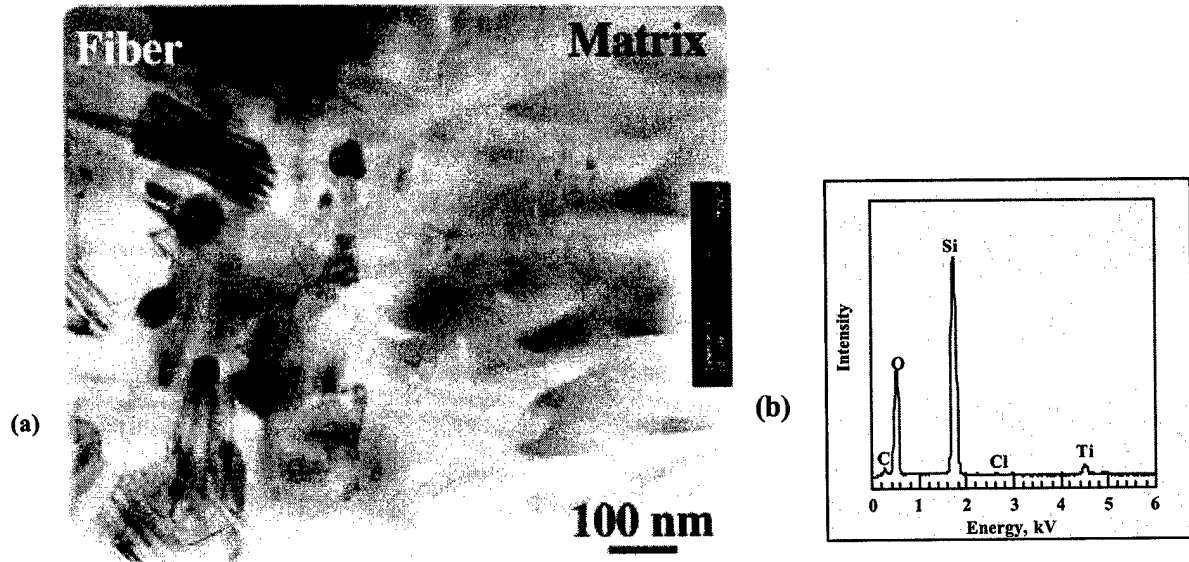


Figure 21. A TEM Image of the Fiber/Matrix Interface in the BF Goodrich Sylramic™/Monazite/CVD-SiC Material (a), and EDX Spectra from the matrix (b)

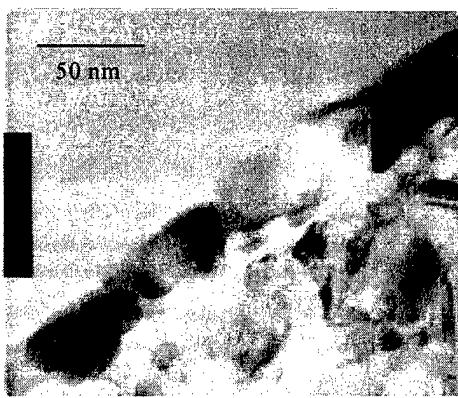


Figure 22. TEM Micrograph of a Hi-NicalonTM/monazite/CVI SiC Mini-CMC Showing the Presence of Monazite Grains (Confirmed by Diffraction) at the Fiber-Matrix Interface

In the ORNL material, the coating was physically present at the interfaces (Figure 23); however, similar to the Hypotherm material, it severely reacted during the processing, resulting in high concentrations of silicon throughout the coating (see EDX spectra inserts in Figure 23b). All mini-CMCs tested to date were brittle with poor strength. It is believed that the lack of survival of the coating is the main problem. There is also a problem of reproducibility with regard to survival of monazite during the CVI processing. A second batch of mini-CMCs fabricated by BFGoodrich showed that the monazite did not survive, although La was still present at/near the interface.

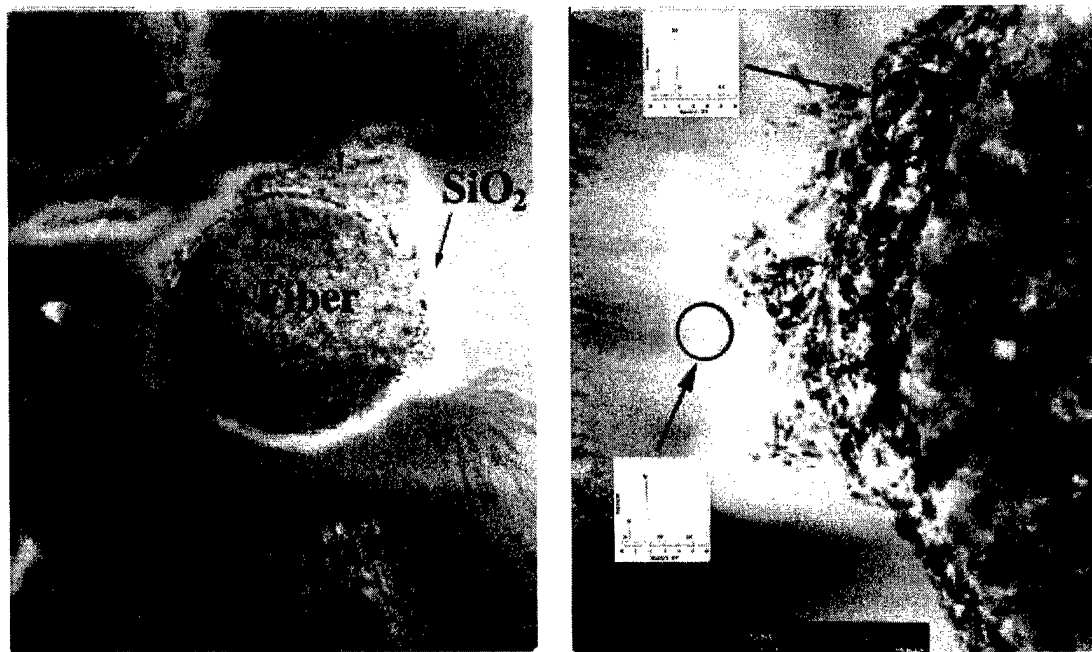


Fig. 23. TEM Images of the Fiber/Matrix Interface in ORNL TyrannoTM SA/Monazite/CVD-SiC Material. The Inserts Show the Respective EDX Data for Coating and the CVD Matrix Adjacent to it.

4.2.2.4 Ube SiC/SiC – Stress-Rupture Tests

Minicomposites fabricated by Ube, Inc. of Japan were tested as part of a collaboration between AFRL and UBE, Inc. It was decided that the most promising composites would be tested in the intermediate temperature range (800 to 1000 °C) under a temperature gradient; this is considered a severe test for these composites. Twelve samples of Tyranno™ ZMI/C/SiZrC Mini-CMC specimens, each nearly 1 foot in length, were obtained. Lengths of 150 cm were cut and mounted with 20 cm of each side embedded in epoxy tabs. The specimens were gripped using cold grips in a horizontal testing machine (MLLN/Life Prediction Group) and tested in tension at temperature using SiC air furnaces with a gauge length of 2.5 cm in the hot zone. The furnace was 7-cm long (total length) with 2.5 cm hot zone in the middle. There was a large temperature gradient along the length of the specimen (Figure 24).

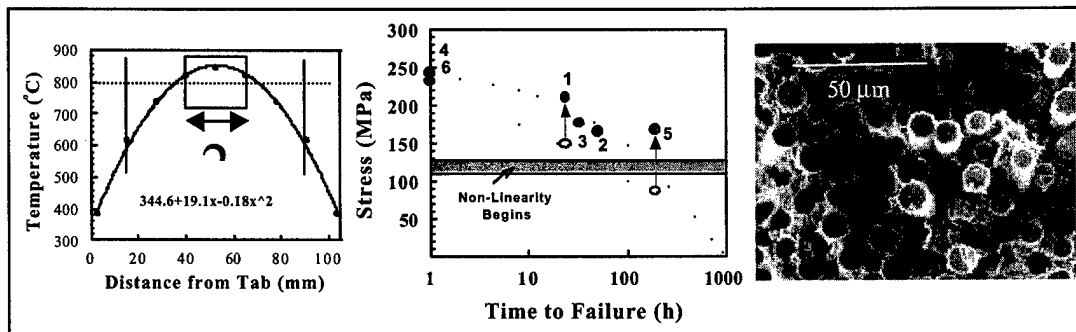


Figure 24. Results of Intermediate Temperature Gradient Tests on UBE minicomposites.

The results of intermediate temperature gradient tests on UBE minicomposites showed some loss in strength with temperature at stresses above the nonlinearity point. Fractography showed short pull-out lengths but no brittle failure. Six specimens were tested in all. Referring to Figure 24, samples #1 and #5 were held at load for a predetermined time; no failure occurred, and the tensile strength of the material was measured. Samples #2 and #3 were held at constant load to failure, while samples #4 and #6 were tested through fast fracture at temperature. Samples #4 and #6 failed in the middle of specimen, where the temperature was approximately 850 °C. Alternately, samples #1, #2, #3, and #5 all failed away from the hot zone, where the temperature was approximately ~800 °C.

4.2.3 Miscellaneous

4.2.3.1 Failure and Deformation Mechanisms in Scheelite

Scheelite, along with monazite, is considered one of the oxide-based alternatives to carbon and boron nitride fiber coatings for improving the high-temperature environmental stability of ceramic matrix composites. Deformation mechanisms in scheelite have been studied using TEM. During the first stage of the study, the focus was on cleavage in the tetragonal lattice of

scheelite. Cleavage planes were studied by the direct observation of the cleavage faults in thin TEM sections of scheelite using diffraction and high-resolution imaging techniques. It was found that, most commonly, scheelite cleaves parallel to the (001) crystallographic plane. However, other cleavage planes, such as (101), were also occasionally observed. In addition, in some cases (001) cleavage may be accompanied by occasional "slip" along the (114) plane (Figure 25a; in this example, the cleavage plane shifts by 9 lattice unit cells in the [001] direction). In some cases, (001) cleavage is combined with periodic kinks in the (011) planes, resulting in a complex cleavage with the general cleavage plane deviating from (001) by about 4 to 5°, Figure 25b.

4.2.3.2 Analyses of Hysteresis Loop to Extract Interface Roughness Parameters

The progressive roughness model was used to develop a code that predicts load-unload cycles during a tension test of a single-fiber microcomposite or multifiber unidirectional mini-composite. Test results from two different laboratories on different SiC-type fiber-reinforced SiC-matrix minicomposites and microcomposites were analyzed. The fibers were Nicalon™, Hi-Nicalon™, and Sylramic™. The interface coatings were C or BN, and the matrix was CVD SiC in all cases. The results are shown in the Figure 26.

The model was found to be helpful in the extraction of roughness parameters. The extracted parameters for Nicalon™ were the most reasonable. The results for Sylramic™ and Hi-Nicalon™ showed sensitivity to compliance removal and matrix crack density. The higher sliding resistance of Sylramic™ fibers was attributed to its shorter interfacial roughness period.

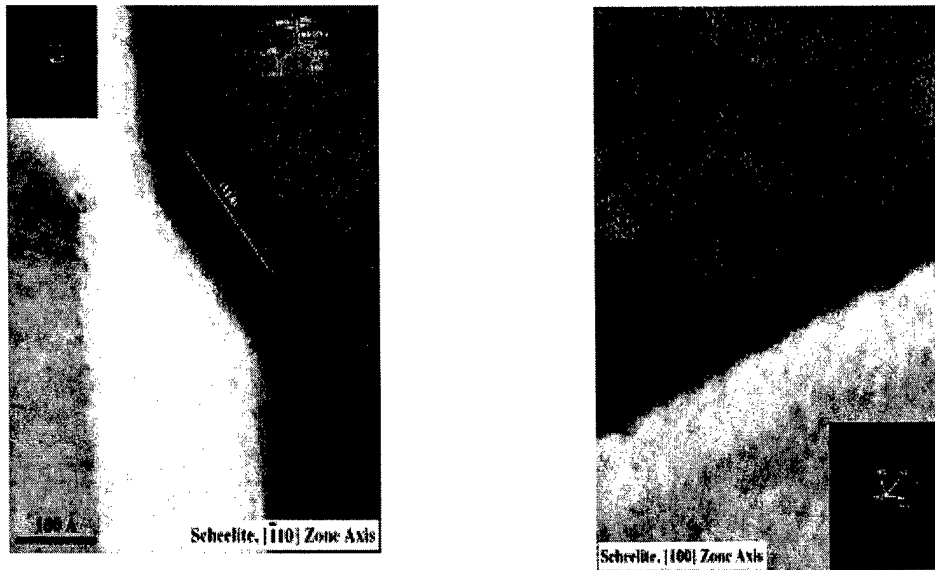


Figure 25. (a) (001) Cleavage Accompanied by Slip Along (114) Plane Resulting in the Offset of the Cleavage Plane by Nine Lattice Unit Cells in the [001] Direction; (b) (001) Cleavage Combined With Periodic Kinks in the (011) Plane, Resulting in the Average Cleavage Plane Deviating from (001) by About 4 to 5°

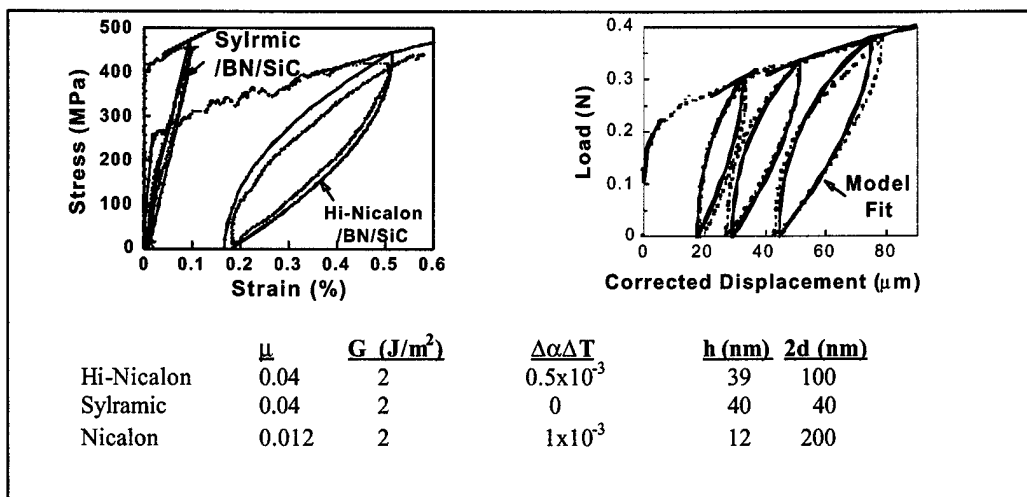


Figure 26. The Hysteresis Data Obtained on Various Micro-CMC and Mini-CMCs Along With the Fit of the Progressive Roughness Model to the Data are Shown (Extracted Interface Parameters.)

4.2.3.3 Fracture Toughness Measurement of Fiber

Preliminary experiments were conducted to measure the fracture toughness of fibers using an indentation-induced, controlled-flaw technique. The ultimate objectives of this study were to measure the fracture toughnesses of various small diameter ($<15 \mu\text{m}$) oxide fibers routinely produced by 3M, Inc. and also to measure the effect of dopants on the fracture toughness of Alumina-YAG Eutectic (AYE) fibers. Feasibility experiments were performed on large diameter ($\sim 100 \mu\text{m}$) AYE fibers, with and without 0.25% TiO_2 doping. Using a Knoop microhardness indentor (50 to 200 gm load), a semicircular crack ($a = \sim 10 \mu\text{m}$) was produced on the fibers. These fibers were then tested in tension to measure the fracture strength of the cracked fibers. The fracture surfaces of the fibers were examined using SEM to precisely measure the indentation crack sizes. Based upon the failure strengths and the indentation-induced crack sizes, the fracture toughnesses of the fibers were calculated. Based upon ~ 5 tests, the calculated average fracture toughnesses were 1.50 and $1.65 \text{ MPa}\cdot\sqrt{\text{m}}$ for undoped and 0.25% TiO_2 doped AYE, respectively. Since the measured difference in fracture toughness values was small, definitive conclusions cannot be presently made concerning the dopant effect on the AYE fiber. However, the technique seems useful, assuming that one can produce distinctive and measurable flaws on the surface of the fiber. In order to apply the current technique to small diameter Nextel™ fibers, a nano-indentation technique should be used. A drawback of this technique is that a large number of tests are required to make the measured value statistically sound. A short manuscript describing the technique is being written and will be submitted for publication.

4.2.3.4 Fugitive Liquid Phase Sintering of Alumina

An innovative processing scheme was explored to achieve dense matrices in CMCs using a fugitive liquid phase sintering route. The processing involves using LiF (m.p. = 845°C) as a fugitive liquid phase to promote densification at low temperature ($<1000^\circ\text{C}$) and low pressure

(<1000 psi). The CMC systems being considered were Nextel™ 610/Alumina and SiC_f/Mullite. Initial experiments were carried out using alumina with LiF to determine the minimum amount of LiF needed to achieve full densification and also to choose the appropriate processing conditions. The LiF amounts studied were 0.1, 0.3, 0.5, 1, and 3 wt%. With a 0.5 wt% LiF addition, full densification of alumina was reached within 30 minutes at 1000 °C/1000 psi. DTA/TGA analysis was performed on the alumina with 1 wt% LiF to examine the vaporization characteristics. Since the amount of LiF was small, it was difficult to resolve the vaporization XRD analysis of as-hot pressed and heat-treated (1100 °C/10hr/air and vacuum) specimens were carried out. It was found that, along with alpha alumina, a small amount of LiAl₅O₈ phase was formed. The amount of this minor phase varied with the LiF content and the heat-treatment condition.

The mullite matrix did not densify with 0.5 wt% LiF, due to the formation of LiAlSi₂O₆ (Spodumene) during hot-pressing. It appears that LiF is not a viable fugitive liquid phase sintering candidate for mullite densification.

A series of reaction couple (YAG/alumina-LiF, Monazite/alumina-LiF) experiments were carried out to examine potential reactions with CMC interface materials. Composites containing a few tows of Nextel™ 610 fibers with LiF-alumina matrix were also fabricated to study the compatibility. An interesting observation was the exaggerated alpha-alumina grain growth in the fiber. A manuscript describing the reaction couple experimental results and the microstructural observations is being written and will be submitted for publication.

4.2.3.5 CVD Processing of Alumina Matrix

Our work has shown the importance of obtaining a dense matrix to properly evaluate interface effectiveness. Collaborative work was conducted with ORNL and Northwestern University to determine if CVD methods could be used to deposit dense alumina matrices on fiber tows to fabricate minicomposites. ORNL used halides as precursors, and preliminary work showed that the interface chemistry was altered significantly by these precursors. The precursors had presumably reacted with the La hexaluminate coatings on sapphire. At Northwestern University, the procedure was different in that metallorganic precursors were used instead of halides. The monazite coating (as well as scheelite and Cerablak™ coatings) survived processing however, the as-deposited alumina was amorphous. The control composites showed very little bonding between the fiber and matrix.

When the matrix alumina was heat treated at 1100 °C for 2 hours, the amorphous alumina crystallized to gamma-alumina; the associated shrinkage resulted in matrix microcracks. The matrix became weak and dislodged during the tension test, leaving the monazite-coated fibers behind (Figure 27). In the control specimen, the alumina bonded strongly to the fiber and resulted in brittle fracture with low strength. Thus, although it was possible to get a dense alumina matrix, it was difficult to obtain dense, crack-free alumina as a matrix using CVD methods. Similar results were obtained using scheelite and Cerablak™ as interlayers.

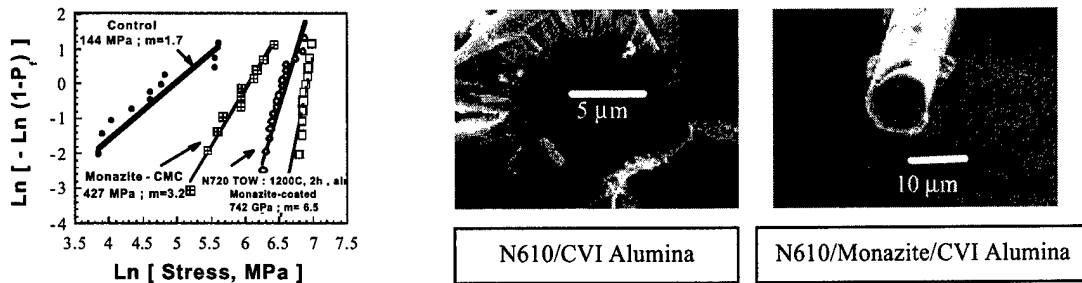


Figure 27. The Minicomposites Fabricated Using Monazite as Interlayers in NextelTM 610-Reinforced CVI Alumina Matrix Mini-CMCs Performed Significantly Better than Control Specimens Under Tension Tests

4.2.3.6 Microstructure of Pure and Doped YAG Fibers Produced by Containerless Method (Containerless Research, Inc., under AFOSR contract)

A TEM study of pure and doped YAG fibers produced by CRI was conducted. The goal of the CRI study was to improve nucleation of YAG and thus reduce the grain size of the polycrystalline fibers. A number of specimens were investigated. It was found that the doped specimens were actually multiphase materials containing alumina and, in some cases, lanthanum hexaluminate (lanthanum being a doping element). A special method of specimen preparation was developed during the course of this study, which allows for the reproducible preparation of high quality TEM specimens from very limited quantities of small diameter ceramic monofilaments.

4.2.3.7 Doped AYE Polycrystals

An experimental study was carried out to extend the AYE Polycrystal (Section 4.1.3.2, [45]) work. The major objective of this research effort was to study the effect of selected dopants on the AYE polycrystal. A previous segregation study showed that calcium and strontium preferentially segregate at alumina and YAG boundaries. A preferential segregation of selected dopants at the boundaries of both eutectic phases and grains in AYE polycrystal may improve the toughness of the polycrystal through interface boundary weakening.

Three kinds of dopants (CaO , SrO , and TiO_2), along with undoped AYE polycrystals, were studied. The dopant amount studied for CaO was 0.1 wt%, and for TiO_2 was 0.25 wt%. For SrO , three dopant levels (0.1, 0.25, and 0.3 wt%) were studied. The specimen preparation followed the same procedure as described in Reference 45. Extensive TEM (EDS) analysis on SrO -doped AYE after heat treatment was carried out in collaboration with Dr. E. Dickey of the University of Kentucky. Definitive segregation of Sr at the alumina/YAG phase boundaries was observed. The results were written and submitted to the Journal of the American Ceramic Society.

The average room temperature flexural strength of as-hot pressed ($1650\text{ }^{\circ}\text{C}/28\text{ MPa}/15\text{ min/Vac}$) 0.1 wt% CaO-doped AYE was 279 MPa and after heat treatment ($1400\text{ }^{\circ}\text{C}/200\text{ hr/Air}$) was 293 MPa. Figures 26 and 27 show the flexural strengths and fracture toughness plots of undoped AYE, along with SrO and TiO_2 -doped AYE. The plots were constructed based upon an average of over 10 data points. A salient point from these plots is that the strength values of the heat-treated doped and undoped AYE are lower than as-hot pressed ones, but the trend is reversed in toughness values. Another major point is that the dopant effect on strength appears very small, although some improvement of the fracture toughness was observed, especially after heat treatment. It was also found that no significant difference was observed after varying the levels (0.1, 0.25 and 0.3 wt.%) of SrO. Since the dopant effect is very small both in strength and toughness, no definitive conclusions can be drawn at present.

SEM fractographic analyses were carried out on selected specimens. It was found that the strength-controlling flaws in the bend bars were processing flaws (e.g., pores, agglomerates of grains, large single-phase grains). It appears that the strength of the AYE can be improved by using starting powders having uniform microstructure. An attempt to produce small AYE powders with uniform microstructures using the Inviscid Melt Spinning (IMS) process at Tulane University was unsuccessful. The resulting powders were large in size, contained large pores, and exhibited a nonuniform microstructure. The microstructural interactions with propagating cracks on the fracture toughness test bars were also examined with SEM. Clear indications of crack deflection at the alumina and YAG phase boundaries were observed in all of the examined fracture surfaces, including undoped AYE. The findings of the current research work are being analyzed further and a manuscript will be written for publication.

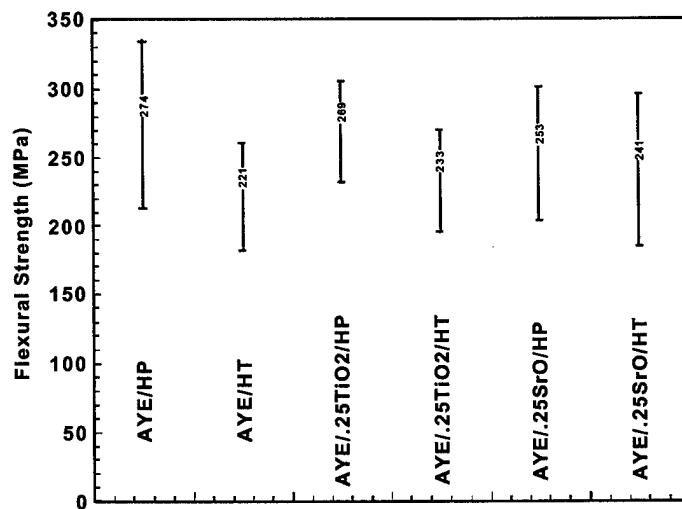
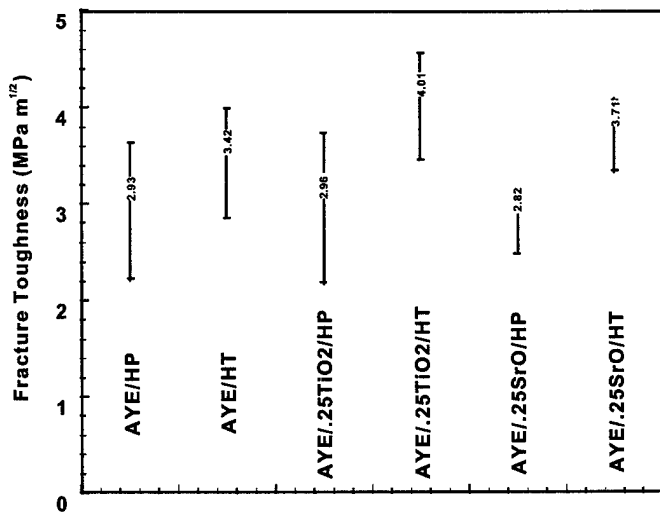


Figure 28. Flexural (4-pt) Strength of AYE Polycrystal with, and without Dopant ($\text{Hp}=1650\text{ }^{\circ}\text{C}/28\text{ MPa}/15\text{ min/Vac.}$, $\text{HT}=1400\text{ }^{\circ}\text{C}/200\text{ hr/Air}$)



**Figure 28. SENB Fracture Toughness of AYE Polycrystal with, and without Dopant
(Hp=1650 °C/28 MPa/15min/Vac., HT=1400 °C/200 hr/Air)**

4.2.3.8 Melt Growth of Piezoelectric Ceramic Fibers

A preliminary study was carried out to determine the feasibility of growing single-crystal piezoelectric ceramics. The experimental work involved composition formulation, DTA/TGA, XRD, and melting and solidification. The compositions studied were $\text{Na}_{0.5}\text{Bi}_{0.5}\text{TiO}_3$ (NBT) and $\text{K}_{0.5}\text{Bi}_{0.5}\text{TiO}_3$ (KBT) with barium oxide additions for selected compositions. Carbonates of Na and K were mixed with TiO_2 , Bi_2O_3 and barium acetate and used for all of the experimental work. The powder mixtures were cold pressed into pellets for sintering studies, as well as XRD analysis. Since significant weight loss occurred through the vaporization of Bi_2O_3 , the initial mixture compositions were adjusted to compensate for this loss. Based upon the DTA/TGA experiments, the reaction temperatures and the melting and solidification temperatures of the NBT and KBT were determined. The melting temperatures of both compositions were between 1280 °–1300 °C. Typically, significant weight loss was observed above 1200 °C; more weight loss occurred in argon than in air. The results correlated well with thermodynamic calculations on the vapor pressure of the constituents and P_{O_2} at the crystal growth temperature. XRD analysis of the samples from DTA/TGA and sintering showed $\text{Na}_{0.5}\text{Bi}_{0.5}\text{TiO}_3$ and $\text{K}_{0.5}\text{Bi}_{0.5}\text{TiO}_3$ as the major phases, with Na and K titanates as minor phases (due to the vaporization loss of bismuth). The composition and amount of minor phases varied depending upon the amount of weight loss in the sample.

Melting experiments were carried out for stoichiometric NBT and NBBT (5.5 mol% barium titanate addition) compositions. XRD analysis of NBBT, sintered at 1100 °C/2 hr/air revealed the presence of only $\text{Na}_{0.5}\text{Bi}_{0.5}\text{TiO}_3$. A detailed comparison of the diffraction peaks of NBT and NBBT showed a slight expansion of the cell dimensions for NBBT.

For melting experiments, the materials were charged into a platinum tube (1.57 mm OD by 1.32 mm ID), and both ends were sealed by crimping. The tubes were placed in the furnace vertically

and melted at 1350 °C/1 hr/air. The X-ray powder diffraction patterns of NBT and NBBT showed the presence of $\text{Na}_{0.5}\text{Bi}_{0.5}\text{TiO}_3$ only. Optical microscopic examination of the extracted melt rod (~1.32mm D x 2cm L) confirmed the single-crystal nature.

These preliminary experiments showed that large (~12.7 mm D by ~152.4 mm L) bulk single-crystal growth of Ba-doped NBT using a modified Bridgman technique is feasible. The production of single-crystal fibers using the EFG technique also seems reasonable and would require detailed die design, along with feasibility experiments.

4.2.3.9 Lanthanum Aluminate Single-Crystal Continuous Fiber Growth for Superconductor Substrate

An effort was initiated to grow single-crystal lanthanum aluminate (LaAlO_3) fibers with a diameter of 250 μm using the edge-defined film-fed growth technique. LaAlO_3 charge material was initially prepared with lanthanum oxide (La_2O_3) from calcined lanthanum acetate powder and alumina powder. Concern about obtaining stoichiometric LaAlO_3 due to the extremely hygroscopic nature of La_2O_3 led to the procurement of single crystal boules of LaAlO_3 . A molybdenum crucible was charged with these boules. The die tips and crucible die lid were also molybdenum.

Initial growth of the LaAlO_3 fiber was attempted with two types of seed fibers, sapphire (Al_2O_3) and SiC (SigmaTM coated with titanium diboride). The sapphire fiber melted upon touching the die tip. The melt was immediately drawn into the tip. A liquid meniscus could not be maintained between the sapphire fiber and the tip to initiate the growth. The SiC fiber also melted upon touching the die tip and melted the portion of the die tip with which it was in contact. A liquid meniscus could not be established between the SiC fiber and the die tip. A 2-mm length of fiber was grown in the course of cleaning the die tips with small diameter molybdenum wire. Efforts are underway to grow the LaAlO_3 using small diameter tungsten wire.

4.3 PUBLICATIONS

1. E.H. Moore, T. Mah, and P.W. Brown, "Carbon Coating of Nextel 550 and 720 by Pitch-Toluene Pyrolysis," *J. Am. Ceram. Soc.*, **80** [5] pp. 1285-1288 (1997).
2. R.S. Hay, J.R. Welch, and M.K. Cinibulk, "TEM Specimen Preparation and Characterization of Ceramic Coatings on Fiber Tows," *Thin Solid Films*, **308-309** pp. 389-392 (1997).
3. P. Chen and T. Mah, "Synthesis and Characterization of Lanthanum Phosphate Sol for Fiber Coating," *J. Mater. Sci.*, **32** [14] pp. 3863-67 (1997).
4. T. Mah, K. Keller, S. Sambasivan, and R.J. Kerans, "High-Temperature Environmental Stability of the Compounds in the Al_2O_3 - Y_2O_3 System," *J. Am. Ceram. Soc.*, **80** [4] pp. 874-878 (1997).

5. M.K. Cinibulk, J.R. Welch, and R.S. Hay, "Transmission Electron Microscopy Specimen Preparation of Ceramic Coatings on Ceramic Fibers," *MRS Symp. Proc.*, **480** pp. 3-17 (1997).
6. M.K. Cinibulk, "Deposition of Oxide Coatings on Fiber Cloths by Electrostatic Attraction," *J. Am. Ceram. Soc.*, **80** [2] pp. 453-460 (1997).
7. M.D. Petry, T. Mah, and R.J. Kerans, "Validity of Using Average Diameter for Determination of Tensile Strength and Weibull Modulus of Ceramic Filaments," *J. Am. Ceram. Soc.*, **80** [10] 2741-44 (1997).
8. R.J. Kerans and T.A. Parthasarathy, "Debond Crack Roughness, Interface Properties and Fiber Coating Design in Ceramic Composites," *Key Engineering Materials*, **127-131** pp. 51-62 (1997).
9. T. Mah and T.A. Parthasarathy, "Effects of Temperature, Environment and Orientation on the Fracture Toughness of Single Crystal YAG," *J. Am. Ceram. Soc.*, **80** [10] pp. 2730-2734 (1997).
10. T.A. Parthasarathy and R.J. Kerans, "Predicted Effects of Interfacial Roughness on the Behavior of Selected Ceramic Composites," *J. Am. Ceram. Soc.*, **80** [8] pp. 2043-2055 (1997).
11. M.K. Cinibulk, "Reactions between Hot-Pressed Calcium Hexaluminate and Silicon Carbide in the presence of Oxygen," *J. Am. Ceram. Soc.*, **81** [11] pp. 2789-98 (1998).
12. M.K. Cinibulk, "Synthesis of Calcium Hexaluminate and Lanthanum Hexaluminate Fiber Coatings," *Ceram. Eng. Sci. Proc.*, **19** [3] pp. 27-35 (1998).
13. M.K. Cinibulk, "Effect of Precursors and Dopants on the Synthesis and Grain Growth of Calcium Hexaluminate," *J. Am. Ceram. Soc.*, **81** [12] pp. 3157-3168 (1998).
14. M.K. Cinibulk, R.S. Hay, and R.E. Dutton, "Textured Calcium Hexaluminate Fiber-Matrix Interphase for Ceramic Matrix Composites"; pp. 853 in *Ceramic Microstructures '96*, edited by A. P. Tomsia and A. Glaeser, New York and London: Plenum Press, 1998.
15. J.I. Lee, N.L. Hecht, and T. Mah, "In situ Processing and Properties of SiC/MoS₂ Nanocomposites," *J. Am. Ceram. Soc.*, **81** [2] pp. 421-424 (1998).
16. B.K. Ahn, W.A. Curtin, T.A. Parthasarathy, and R.E. Dutton, "Criteria for Crack Deflection/Penetration criteria for Fiber-Reinforced Ceramic Matrix Composites," *Composite Sci. & Tech.*, **58** [11] pp. 1775-1784 (1998).
17. R.J. Kerans, T.A. Parthasarathy, F. Rebillat, and J. Lamon, "Interface Properties in High Strength Nicalon/C/SiC Composites as Determined by Rough Surface Analysis of Fiber Pushout Tests," *J. Am. Ceram. Soc.*, **81** [7] pp. 1881-1887 (1998).

18. T.A. Parthasarathy, C.A. Folsom, and L.P. Zawada, "Combined Effects of Exposure to Salt (NaCl) Water and Oxidation on The Strength of uncoated and BN-coated Nicalon Fibers," *J. Am. Ceram. Soc.*, **81** [7] pp. 1812-1818 (1998).
19. R.J. Kerans and T.A. Parthasarathy, "Fiber Coating Design Parameters for Ceramic Composites as Implied by Considerations of Debond Crack Roughness," presented at *Ceramic Microstructures: Control at the Atomic Level*, Berkeley, California 1998.
20. T.A. Parthasarathy and R.J. Kerans, "Thermal Gradient Resistant Oxide-Oxide Ceramic Composite," Patent App. No. # 09/483,924, AFRL Invention Disclosure AFD 00373 - April 26 1999, 1999.
21. E. Boakye, R.S. Hay, and M.D. Petry, "Continuous Coating of Oxide Fiber Tows Using Liquid Precursors: Monazite Coatings on NextelTM 720," *J. Am. Ceram. Soc.*, **82** [9] pp. 2321-2331 (1999).
22. M.K. Cinibulk and R.S. Hay, "Method of Forming Tubular Inclusions in Single-Crystal Alumina," U.S. Patent No. 5 894 035, USA, 1999.
23. R.S. Hay, E.E. Boakye, M.D. Petry, Y. Berta, K.V. Lehmden, and J. Welch, "Grain Growth and Tensile Strength of 3M Nextel 720 after Thermal Exposure," *Ceram. Eng. Sci. Proc.*, **20** [3] pp. 153-163 (1999).
24. R.J. Kerans, R.S. Hay, and T.A. Parthasarathy, "Structural Ceramic Composites," *Current Opinion in Solid State and Materials Science*, **4** pp. 445-451 (1999).
25. P. Mogilevsky and A. Zangvil, "Modeling of Oxidation Behavior of SiC-Reinforced Ceramic Matrix Composites," *Mater. Sci. Eng.*, **A262** pp. 16 (1999).
26. E.E. Boakye, R.S. Hay, M.D. Petry, and T.A. Parthasarathy, "Zircon-Carbon For Ceramic Composite Fiber Coatings and Fine-Grained Zircon Powder," U.S. Patent No. 6,221,942 B1, USA, 2001.
27. E.E. Boakye, M.D. Petry, and R.S. Hay, "Ceramic Composite," U.S. Patent No. 5,759,632, USA, 1999.
28. M.D. Petry and T. Mah, "Effect of Thermal Exposure on the Strengths of Nextel 550 and 720 Filaments," *J. Am. Ceram. Soc.*, **82** [10] pp. 2801-2807 (1999).
29. T.A. Parthasarathy, R.J. Kerans, and N.J. Pagano, "Effective Fiber Properties to incorporate Coating Thermoelastic Effects into Fiber/Matrix Composite Models," *J. Am. Ceram. Soc.*, **82** [3] pp. 579-584 (1999).
30. R.J. Kerans and T.A. Parthasarathy, "Crack Deflection in Ceramic Composites and Fiber Coating Design Criteria," *Composites Part A*, **30A** [4] pp. 521-524 (1999).

31. T.A. Parthasarathy, E.E. Boakye, M.K. Cinibulk, and D.M. Petry, "Fabrication and Testing of Oxide/Oxide Microcomposites with Lanthanum Phosphate and Calcium Hexaluminate as Interlayers," *J. Amer. Ceram. Soc.*, **82** [12] pp. 3575-3583 (1999).
32. E. Boakye, R.S. Hay, M.D. Petry, and T.A. Parthasarathy, "Sol-gel Synthesis of Zircon-Carbon Precursors and Coatings on Nextel 720 Fiber Tows," *J. Am. Ceram. Soc.*, **20** [3] pp. 165-172 (1999).
33. K. Keller, T.A. Parthasarathy, T. Mah, M.K. Cinibulk, and E.E. Boakye, "Evaluation of Monazite as Interlayer in Dense Matrix Composites," *Ceram. Sci. Eng.*, **20** [3] pp. 451-462 (1999).
34. E.E. Boakye, R.S. Hay, R.J. Kerans, and P. Mogilevsky, "Oxidation Inhibition of SiC by Monazite," Patent No. Pending, USA, 2000.
35. R.S. Hay, E.E. Boakye, and M.D. Petry, "Effect of Coating Deposition Temperature on Monazite Coated Fiber," *J. Eur. Ceram. Soc.*, **20** pp. 589-597 (2000).
36. M.N. Rahaman, T. Huang, T. Mah, and T.A. Parthasarathy, "In-situ Reinforced Mullite"; pp. 211-222 in Ceramic Transactions, Vol. 103, *Advances in Ceramic-Matrix Composites V*. Edited by N. P. Bansal, J. P. Singh and E. Ustandag. American Ceramic Society, Westerville, OH, 2000.
37. K.A. Keller, T. Mah, E.E. Boakye, and T.A. Parthasarathy, "Gel-casting and Reaction Bonding of Oxide-Oxide Minicomposites with Monazite Interphase," *Cer. Eng. Sci. Proc.*, **21** [3] pp. 525-534 (2000).
38. T. Huang, M.N. Rahaman, T.-I. Mah, and T.A. Parthasarathy, "Effect of SiO_2 and Y_2O_3 additives on the anisotropic grain growth of dense mullite," *J. Mater. Res.*, **15** [3] pp. 718-726 (2000).
39. M.K. Cinibulk, "Hexaluminates as a Cleavable Fiber-Matrix Interphase: Synthesis, Texture Development, and Phase Compatibility," *J. Eur. Ceram. Soc.*, **20** pp. 569-582 (2000).
40. M.K. Cinibulk, T.A. Parthasarathy, K.A. Keller, and T. Mah, "Porous Rare-Earth Aluminate Fiber Coatings for Oxide-Oxide Composites," *Ceram. Eng. Sci. Proc.*, **21** [4] pp. 219-228 (2000).
41. V.R. Kutta, R. Anthenien, R. Mantz, W.M. Roquemore, R.A. Brockman, R. John, L.P. Zawada, T.A. Parthasarathy, and R. Kerans, "Influence of Ceramic-Matrix-Composite Wall Plates on Combustor Performance," *36th AIAA/ASME/SAE/ASEE Joint Conference Proceedings*, AIAA 2000-3351 pp. 1-10 (2000).
42. S.M. Sim, K.A. Keller, and T. Mah, "Phase Formation in Yttrium Aluminum Garnet Powders Synthesized by Chemical Methods," *J. Mater. Sci.*, **35** pp. 713-717 (2000).

43. E.E. Boakye, M.D. Petry, and R.S. Hay, "Washed Lanthanum Phosphate (Monazite) Fiber Coatings: Strength Retention after Coatings," Patent No. Pending, USA, 2000.
44. E.E. Boakye, R.S. Hay, P. Mogilevsky, and L.M. Douglas, "Monazite Coatings on Fibers: II, Coating Without Strength Degradation," *J. Am. Ceram. Soc.*, in review.
45. T. Mah, T.A. Parthasarathy, and R.J. Kerans, "Processing, Microstructure and Strength Alumina-YAG Eutectic Polycrystals," *J. Am. Ceram. Soc.*, **83** [8] pp. 2088-2090 (2000).
46. E.E. Boakye, M.D. Petry, R.S. Hay, and L.M. Douglas, "Monazite Coatings on NextelTM 720, 610, and TyrannoTM-SA Fiber Tows; Effects of Precursors on Fiber Strength," *Ceram. Eng. Sci. Proc.*, **21** [4] pp. 229-235 (2000).
47. M.K. Cinibulk, "Synthesis of Yttrium-Aluminum Garnet from a Mixed Metal Citrate Precursor," *J. Am. Ceram. Soc.*, **83** [5] pp. 1276-1278 (2000).
48. R.S. Hay and E.E. Boakye, "Tensile Strength of Monazite and Monazite-Alumina Coated Fibers: Temperature Dependence and Degradation Mechanisms," *J. Am. Ceram. Soc.*, in review.
49. T. Huang, M.N. Rahaman, T. Mah, and T.A. Parthasarathy, "Anisotropic Grain Growth and Microstructural Evolution of Dense Mullite above 1550C," *J. Am. Ceram. Soc.*, **83** [1] pp. 204-210 (2000).
50. R.E. Dutton, N.J. Pagano, R.Y. Kim, and T.A. Parthasarathy, "Modeling the Ultimate Tensile Strength of Unidirectional Glass Matrix Composites," *J. Am. Ceram. Soc.*, **83** [1] pp. 166-174 (2000).
51. K.A. Keller, T. Mah, T.A. Parthasarathy, and C.M. Cooke, "Fugitive Interfacial Carbon Coatings for Oxide-Oxide Composites," *J. Am. Ceram. Soc.*, **83** [2] pp. 329-336 (2000).
52. T.A. Parthasarathy, "Extraction of Weibull Parameters of Fiber Strength from Means and Standard Deviations of Failure Loads and Fiber Diameters," *J. Am. Ceram. Soc.* **84** [3] pp. 588-92 (2001).
53. K.A. Keller, T. Mah, T.A. Parthasarathy, E. E. Boakye, and M. Cinibulk, "Evaluation of All-Oxide Composites Based on Coated NextelTM 610 and 650 Fibers," *Ceram. Eng. Sci. Proc.*, (2001).
54. M.K. Cinibulk and T.A. Parthasarathy, "Characterization of Oxidized Polymer-Derived SiBNC Fibers," *J. Am. Ceram. Soc.* (in press).
55. T.A. Parthasarathy, E. Boakye, K. Keller, and R.S. Hay, "Evaluation of Porous ZrO₂-SiO₂ and Monazite coatings using Nextel 720 Fiber-Reinforced Blackglas Matrix Minicomposites," *J. Am. Ceram. Soc.* (in press).

56. M.K. Cinibulk, "Effect of Divalent Cations on the Synthesis of Citrate-Gel Derived Lanthanum Hexaluminate Powders and Films", *J. Mater. Res.*, **14** [9] pp. 3581-3593 (1999).
57. R.J. Kerans, T.A. Parthasarathy, P.D. Jero, and R.S. Hay. "Interfaces in Ceramic Composites," in *Ceramic Engineering Handbook*, edited by M. N. Rahaman: Marcel Decker, Inc., in press.
58. T.A. Parthasarathy, "Composite Mechanics and Behavior," in *Ceramic Engineering Handbook*, edited by M. N. Rahaman: Marcell Decker, Inc., in press.
59. R.J. Kerans, R.S. Hay, T.A. Parthasarathy, and M.K. Cinibulk, "Interface Design for Oxidation Resistant Ceramic Composites," *J. Am. Ceram. Soc.*, (in review).
60. M.K. Cinibulk, K.A. Keller, T. Mah, and T.A. Parthasarathy, "Nextel 610 and 650 Fiber Reinforced Porous Alumina-YAG Matrix Composites," *Ceram. Eng. Sci. Proc.*, in press.

4.4 PATENTS

1. E.E. Boakye, M.D. Petry, and R.S. Hay, "Ceramic Composite," U.S. Patent No. 5,759,632, USA, 1999.
2. M.K. Cinibulk and R.S. Hay, "Method of Forming Tubular Inclusions in Single-Crystal Alumina," U.S. Patent No. 5,894,035, USA, 1999.
3. E.E. Boakye, R.S. Hay, M.D. Petry, and T.A. Parthasarathy, "Zircon-Carbon For Ceramic Composite Fiber Coatings and Fine-Grained Zircon Powder," U.S. Patent No. 6,221,942 B1, USA, 2001.
4. T.A. Parthasarathy and R.J. Kerans, "Thermal Gradient Resistant Oxide-Oxide Ceramic Composite," U.S. Patent Application No. 09/483,924, 1999.
5. E.E. Boakye, M.D. Petry, and R.S. Hay, "Washed Lanthanum Phosphate (Monazite) Fiber Coatings: Strength Retention after Coatings," Patent No. Pending, USA, 2000.
6. E.E. Boakye, R.S. Hay, R.J. Kerans, and P. Mogilevsky, "Oxidation Inhibition of SiC by Monazite," Patent No. Pending, USA, 2000.

4.5 BOOK CHAPTERS

1. R.J. Kerans, T.A. Parthasarathy, P.D. Jero, and R.S. Hay, "Interfaces in Ceramic Composites," in *Ceramic Engineering Handbook*, edited by M. N. Rahaman: Marcel Decker, Inc., in press.

2. T.A. Parthasarathy, "Composite Mechanics and Behavior," in *Ceramic Engineering Handbook*, edited by M. N. Rahaman: Marcell Decker Inc., in press.
3. M.L. Gambone, R.S. Hay, P.D. Jero, A.P. Katz, T. Mah, and L.E. Matson, "Ceramic Fibers" in *Ceramic Engineering Handbook*, edited by M.N. Rahaman: Marcell Decker, Inc., in press.

LIST OF ACRONYMS

<u>ACRONYM</u>	<u>DESCRIPTION</u>
AC	Air Cooling
AEM	Anger Electron Microscopy
AF	Alpha Forging
AFRL	Air Force Research Laboratory
APD	Anti-Phase Boundary
ARL	Alpha-Rolled Lamellar
ASC-MSRC Center	Air Force System Command-Materials Science Research
at.	Atomic
BCC	Body Centered Cubic
BDTT	Brittle Ductile Transition Temperature
BSEI	Back Scattered Electron Image
CCG	Creep Crack Growth
CMC	Ceramic Matrix Composites
CTE	Coefficient of Thermal Expansion
CVD	Chemical Vapor Deposition
CVI	Chemical Vapor Infiltration
DoD	Department of Defense
DOE	Department of Energy
DRA	Discontinuously Reinforced Aluminum
DRCu	Discontinuously Reinforced Copper
DS	Directionally Solidified
DSM	Dilute Solution Model
DTA	Differential Thermal Analysis
EAM	Embedded Atom Method
ECAP	Equal Channel Angular Pressing
EDS	Energy Dispersion Spectroscopy
EDX	Energy Dispersive Analysis
FCG	Fatigue Crack Growth
FEM	Finite Element Method
FL	Fully Lamellar
FL-GFBC	First Principles-Green's Function Boundary Condition
FS	Fatigue Strength
GC	Gel Casting
GFBC	Green's Function Boundary Condition
GE	General Electric
GE-CRD	General Electric-Corporate Research and Development
GF	Green's Function
GS	Grain Size
HDA	High-Density Area
HBD	High Bulk Density

LIST OF ACRONYMS (CONTINUED)

<u>ACRONYM</u>	<u>DESCRIPTION</u>
HIP	Hot Isostatic Process
HP	Half Petch
IHPTET	Integrated High Performance Turbine Engine Technology
IMS	Inviscid Melt Spinning
LANL	Los Alamos National Laboratory
LDA	Low-Density Areas
LGF	Lattice Green's Function
LS	Lamellar Spacing
LM	Lamellar Material
LTE	Low Temperature Expansion
MSAAF	Multiscalar Analysis of Area Functions
NRL	National Research Laboratory
NSF	National Science Foundation
OTMC	Orthorhombic Titanium Matrix Composites
PAM	Plasma Arc Melting
P&W	Pratt & Whitney
PA	Polyacrylic Acid
PST	Polysynthetically Twinned
PVD	Plasma Vapor Deposition
RB	Reaction Bonding
RBMO	Reaction Bonding of Metal Oxide
RBSN	Reaction Bonding of Silicon Nitride
RT	Room Temperature
SEM	Scanning Electron Microscopy
SENB	Single Edged Notched Beam
SOCHE	Southern Ohio Council of Higher Education
SVIB	Spatially Varied Interfacial Bonding
TEM	Transmission Electron Microscopy
TEOS	Tetraethoxysilane
TGA	Thermogravimetric Analysis
TMC	Titanium Matrix Composites
TMP	Thermomechanical Processing
TMPL	Thermomechanically Processed Lamellar
TMS	The Minerals and Metal Society
TMT	Thermomechanical Treatments
TYT	Titanium-Yttrium-Titanium
WUD	Work Unit Directive
XRD	X-ray Diffraction
YS	Yield Strength
ZEOS	Zierconium Ethoxide
ZN	Zirconyl Nitrate Hydrate